Order Number 9513424

Dynamics of a turbulent jet interacting with a free surface

Mangiavacchi, Norberto, Ph.D.

The University of Michigan, 1994

U·M·I

300 N. Zeeb Rd.
Ann Arbor, MI 48106

Dynamics of a Turbulent Jet Interacting with a Free Surface

by

Norberto Mangiavacchi

A dissertation submitted in partial fulfillment
of the requirements for the degree of
Doctor of Philosophy
(Mechanical Engineering and Scientific Computing)
in The University of Michigan
1994

Doctoral Committee:

Associate Professor Rayhaneh Akhavan, Chair
Associate Professor Luis Bernal
Associate Professor Gretar Tryggvason
Assistant Professor David Walker

To my wife

ACKNOWLEDGEMENTS

I would like to express special thanks and appreciation to my thesis supervisor, R. Akhavan, for her patient guidance, encouragement and support throughout the period of my study. My regards are also to Professor L. Bernal, G. Tryggvason, and D. T. Walker, for their advice and valuable comments on this study. And I also wish to thank all those who helped me in completing this thesis, especially Amid Ansari, many insightful conversations on various topics of this thesis, and Ravishankar Gundlapalli for his help on the data analysis. Finally, I would like to express my very special thanks to my parents, Valter Mangiavacchi, and Annamaria Silenzi, to my wife Ieda Polessa Mangiavacchi, and all other family members, who all helped make it possible and worthwhile to complete this work.

This work was supported by CNPq, Brazilian Government Council of Research and Development, and ONR contract #N00014-92-J-1750. The computations were performed at the San Diego Supercomputer Center which is sponsored by the National Science Foundation. The support is gratefully acknowledged.

PREFACE

The dynamics of free surface turbulence at low Froude numbers has been investigated by direct numerical simulations of a series of temporally growing round turbulent jets issued below and parallel to a clean free surface. The jets had a Reynolds number of 10000 based on initial jet diameter and centerline velocity ($Re_\lambda \approx 100$), a Froude number of 0.1 and were issued at depths of 1.0, 1.5, and 2.0 jet diameters below the surface, respectively. A passive scalar with a Schmidt number of 0.7 was also included in the simulation.

The statistics and structure of the jet was found to be in good agreement with experimental measurements in free-surface jets. As the jet approaches the free-surface, the vertical turbulent fluctuations are damped in a 'surface layer' of magnitude on the order of one lateral Taylor microscale, and the horizontal turbulent fluctuations are amplified.

Two classes of organized vortical structures could be identified within the surface layer of the jet; (i) vortex tubes with axis parallel to the free surface oriented along the direction of the mean flow strain field and, (ii) vortex tubes with axis normal to the free surface connected to the surface. The interaction of these structures with the free surface leads to the establishment of a secondary flow which pumps the flow upwards towards the free surface at the jet centerplane and outwards towards the edges of the jet on the surface. This phenomenon, known as the surface current, has also been observed in experimental studies. The parallel vortex tubes are subject

to three-dimensional dynamics and the usual cascade of energy to the small scales. The reconnected vortex tubes, on the other hand, are not subject to strong vortex stretching near the free surface and form long-lasting coherent structures which grow with time and occasionally merge, leading to a reverse cascade of energy towards the large scales and the establishment of a nearly two-dimensional turbulent state in the immediate vicinity of the free surface.

The implications of this two-dimensionality for the modeling of free-surface turbulence is discussed. The ability of various subgrid scale models in capturing these free-surface effects is assessed by *a priori* tests. The dynamic two-component model developed by Ansari *et al.* (1994) is shown to be a promising model for LES of free-surface turbulence.

TABLE OF CONTENTS

LIST OF FIGURES

LIST OF TABLES

LIST OF APPENDICES

Appendix

CHAPTER I

INTRODUCTION

Understanding the interactions of a turbulent flow with a free surface is of interest in many fields such as marine hydrodynamics, oceanic sciences, and industrial processes. One application that has gained particular interest is the identification of signatures of ship wakes on the sea surface. The signatures persist for very large distances behind the ship in the viscous wake region and can be identified by aerial and space photographs as well as by Syntethic Aperture Radar (SAR) images. These signatures have been attributed to surface disturbances created by the ship hull and propulsion system (Lyden et al 1988) and to short-wavelenght surface waves generated behind the ship (Munk, Scully-Power & Zachariesen 1987). Milgram et al. (1993) demonstrated the direct association between the reduced radar return (dark streaks in SAR images) and reduced scattering wave energy, and showed also that the principal reasons for the reduced short wave energy in ship wakes are ship-generated turbulence and surface film distributions. Since the surface film distribution itself is also affected by the turbulent wake, the interaction of the turbulent flow with the free surface is very important for the understanding and interpretation of SAR images.

1.1 Background

There have been a number of investigations dealing with different aspects of the interaction of turbulent flows with a free surface. Many aspects, however, are still not completely understood. Early studies of Evans (1955), Taylor (1955), and later Longuet-Higgins & Stewart (1961), and Taylor (1962), focussed on the effect of surface currents on the amplitude of surface waves. Longuet-Higgins & Stewart (1961) found that waves traveling on a non-uniform current that varies in the direction of the wave propagation undergo an amplification due to a nonlinear interaction between the waves and the components of the current. Taylor (1962) analyzed the changes in amplitude and wavelength of standing waves of uniform wavelength existing in an area of uniform surface divergence. The motivation for his study of this model flow was the common observation of the appearance of smooth areas in the disturbed water downstream of a lock when the sluice gates are opened which. As Taylor points out, these correspond to rising turbulent currents spreading out at the surface with horizontal divergence. Fabrikant and Raevsky (1994) have recently developed a theory for the scattering of gravity waves by vortical flows in the ocean. They found that for homogeneous turbulence the scattering characteristics are determined by the large scale spectrum components that are usually anisotropic and inhomogeneous.

Rajaratnam & Humphries (1984), Rajaratnam & Subramanyan (1985) and Swean et al. (1989) investigated surface jets with applications to civil and hydraulic engineering. They found that growth rates of the length and velocity scales resemble those of a two-dimensional wall jet at the same Reynolds number. On the related problem of the interaction of a jet with a solid surface, Launder & Rodi (1981, 1983) provide a comprehensive review of investigations of the solid wall jet for different jet

exit geometries. Swean et al. (1989) made turbulence measurements in a developing planar surface jet and noted a decrease in vertical velocity fluctuations near the free surface.

Experimental investigations of the interaction of a round jet with a free surface were reported by Bernal & Madnia (1988), Anthony & Willmarth (1992), Madnia & Bernal (1994) and Walker et al (1994). Madnia & Bernal (1994) chose this flow because it is one of the simplest flows configurations which incorporates many of the vortical interactions encountered in the ship wake problem. They reported measurements of the mean velocity and turbulence intensities, using hot-film velocity measurements, flow visualization and surface curvature measurements. Madnia & Bernal (1994) observed characteristic dark circular features in shadowgraph images of the surface associated with concentrated vorticity normal to the surface, which is believed to be the result of vortex line reconnection processes in the turbulent flow. Anthony & Willmarth (1992), using three-component laser Doppler velocimeter and visualizations of the flow using fluorescent dye and free-surface shadowgraphs, observed the formation of a shallow surface current that consists largely of fluid structures ejected from the jet. These structures remain coherent within the current, supposedly as a consequence of reduced turbulent mixing just beneath the surface. They also observed that when an insoluble surfactant is added to the surface, the surface current is suppressed.

Measurements of the structure of turbulence beneath a free surface have been reported. Komori et al. (1982) used a laser velocimeter to measure the turbulent fluctuations and Reynolds stress beneath a free surface in two-dimensional flows in open channels. They found that as the free surface is approached, the velocity fluctuations become anisotropic, the normal component are damped while the parallel

components are enhanced. Similar findings have been reported by Swean (1989) for the two-dimensional surface jet, and by Anthony & Willmarth (1992), and Walker et al (1994) for a round jet interacting with a free surface.

Rashidi et al. (1992) studied the effect of surface waves on turbulent quantities such as the mean velocities, turbulence intensities, and Reynolds stresses near the free surface, in wall turbulent flows, concentrating their analysis on the effect of the wavy motion on the wall shear stress, and the frequency of ejection-insweep cycles.

A number of recent works deal with the observation and interpretation of vortex interactions with a free surface. Several experimental papers on the interaction of tilted vortex rings with a free surface have been published, such as Bernal and Kwong (1989), Bernal et al (1989), Sarpkaya and Suthon (1991). Tryggvason et al. (1991) and Song et al (1990) have performed numerical simulations with an inviscid model, and Dommermuth and Yue (1991) performed numerical simulations using a viscous model. Hirsa & Willmarth (1994) analyzed the effect of contamination on the interaction of a vortex pair with a free surface, and observed that when vortex pairs rise and interact with a free surface they cause characteristic surface deformations known as scars and striations. These are caused by stretching and interaction of cross-stream vortices near the surface. When a small amount of surface contamination is present, they observe the formation of contamination fronts on the surface and secondary vorticity of opposite rotation, that cause the primary vortex pair to rebound from the surface. Rood (1994) proposes an explanation for the vortex attachment process, which does not rely on vortex image methods, but on the flux of vorticity to the boundary. As an example Rood explains the experimental observation of Bernal and Kwong (1989) that in a vortex ring approaching the free surface along an inclined path the upper arc of the ring "breaks" to form a loop with its

ends terminating at the surface. According to Rood, during this process as the vortex loop approaches the free surface, the core is deformed against the surface leading to large vorticity diffusion. In the limit of low Froude number the surface-parallel vorticity disappears, leaving the remainder of the loop with ends terminating at the free surface. One important conclusion is that vortex reconnection to the surface is a viscous process, and therefore it may be Reynolds number dependent. This Reynolds number dependence has been observed in Willert and Gharib (1994) experiment on the interaction of modulated vortex pairs with a clean and contaminated free surface. In this experiment, for low Reynolds numbers and a clean surface, the vortex pair locally "reconnects" by removing the vorticity from the vortex tube closest to the surface to form two parallel lines of U-vortices, whereas for higher Reynolds numbers the reconnection process is not as clearly seen, the vortical structure being "shattered" as it reaches the surface, presumably because there is insufficient time for the lobe of the spatially modulated vortex closest to the surface to loose its vorticity to the surface by accelerating the surface locally, forming a reconnection site (i.e. surface normal vorticity). These vortex free-surface interaction studies provide with some basic tools for the understanding of free-surface turbulence.

A theory for the structure of turbulence in the vicinity of plane boundaries developed by Hunt and Graham (1978) was extended to a free surface in the limit of negligible surface deformation by Hunt (1984). Hunt and Graham's (1978) development is based on a linear theory and is restricted to short times of interaction between the turbulent flow and the shear-free boundary. Over longer times nonlinear effects develop, such as large eddies straining smaller eddies near the boundary, and Hunt (1984) suggests some estimates of this effect.

Hunt's (1984) theory was found to be in general qualitative agreement with ex-

perimental measurements of spectra and profiles of turbulence intensities in a free-surface grid-stirred tank by Brumley and Jirka (1987). Nevertheless, these measurements reveal important dynamical effects which are not properly accounted for by the purely kinematical theory of Hunt. In particular, the experimental data show a higher concentration of turbulence energy at the low wavenumbers in the tangential velocity components near the free surface than that predicted by Hunt's theory. Measurements also show the surface induced anisotropy in the velocity fluctuations to extend to high wavenumbers, well into the inertial subrange, as the free surface is approached. However, closer examination of the one-dimensional energy spectra in the experiments of Brumley and Jirka (1987) shows the presence of two distinct subranges in the spectra of horizontal velocity components within the surface influenced layer; a $k^{-5/3}$ subrange at intermediate wavenumbers and a k^{-3} subrange at high wavenumbers. At large distances away from the free surface, the k^{-3} range disappears. Similar trends can also be observed in the experimental measurements of turbulent planar free-surface jets by Swean et al. (1991). Close examination of the one-dimensional energy spectra of horizontal velocity components within the surface layer in these experiments also show the presence of two distinct subranges; a $k^{-5/3}$ range at intermediate wavenumbers and a k^{-3} range at high wavenumbers. Furthermore, the data indicate a trend for pile-up of energy in the horizontal velocity components near the surface as the jet moves downstream. The authors attribute this to the presence of slowly dissipating vertically oriented coherent vortex tubes which connect normal to the free surface.

These connected vertical vortex tubes, which have also been observed in a number of other experimental studies of free-surface flows (Madnia and Bernal 1989, Sarpkaya and Suthon 1991, Gharib et al. 1992, Dommermouth 1993), are indeed

a major distinguishing feature of free surface turbulence from wall-bounded or free turbulent shear flows. At low Froude numbers, these vortices are not subject to significant vortex stretching in the immediate vicinity of the free surface. Therefore, the cascade of energy to the small scales within such vortices is inhibited, leading to their longevity and the establishment of a nearly two-dimensional turbulent state in the immediate vicinity of the free surface. These vortex tubes, however, are not the only admissible class of vortical structures in the vicinity of a free surface. Another class might consist of vortex tubes which are oriented parallel to the free surface. In contrast to the former structures, these vortices are subject to strong vortex stretching and the usual cascade of energy to the small scales. Thus the overall dynamics of turbulence near a free surface may be determined by a delicate balance between the two classes of structures.

1.2 Objectives

The objective of this study is to provide a better understanding of the dynamics of turbulence near a free surface, in particular with regards to the importance of two-dimensionality within the surface influenced layer and implications for the development of accurate subgrid-scale models for LES of free-surface turbulence. The studies are based on results from direct numerical simulations of a temporally growing submerged turbulent round jet which is issued parallel to a clean free surface. This flow exhibits many of the features of ship wakes and because of its inherent simplicity has served as a prototype flow in a number of recent experimental studies of free-surface turbulence (Madnia & Bernal 1989, Anthony 1990, Liepmann 1990, Walker et al (1994).

Specifically, our studies will provide information on the topology and dynam-

ics of large- and small-scale coherent structures and the detailed interscale energy transfers near the free surface, assess the importance of two-dimensionality and the reverse cascade of energy near the free surface and relate the observed phenomena to the underlying dynamics of vortical structures to provide a physical basis for the evaluation of subgrid-scales model for LES of free-surface turbulent flows.

The organization of this work is as follows. In §2 the physical parameters of the problem are introduced and the numerical methods are discussed. The evolution of the jet from laminar to turbulent stages is presented in §3. In §4 the statistics of the free-surface turbulent jet are compared to known experimental results. The small-scale structures of the jet are examined in §5, followed in §6 by a discussion of the dynamical role of these structures in the interscale energy transfers and the dynamics of the cascade. The implications for the development of more accurate subgrid-scale models of free-surface turbulence are discussed on §7. Conclusions are presented in §8.

CHAPTER II

NUMERICAL METHODS

In this chapter we discuss the numerical schemes which were employed in our direct numerical simulation study of an incompressible, temporally growing, round turbulent jet issued parallel to a free surface. The governing equations are presented first, followed by a general description of the boundary conditions, the numerical methods, the initial conditions and other flow parameters used in the simulations.

2.1 Governing Equations

We investigate the evolution and dynamics of a temporally growing round jet which is issued parallel to a clean free surface at a depth varying from one to two jet diameter below the surface ($\frac{H}{D}$ = 1, 1.5, and 2). A schematic of the jet and of the coordinate system used in this study is shown in Figure 2.1. The initial laminar jet had a Reynolds number, $Re_o = \frac{DU_o}{\nu}$, of 10000 based on initial jet diameter and centerline velocity and a Froude number, $Fr = \frac{U_o}{\sqrt{gD}}$, of 0.1. This Froude number is small enough to allow the use of linearized free-surface boundary conditions in the simulations, thus resulting in significant savings in the required computational resources.

The evolution of the jet is tracked in a Cartesian coordinate system by solving

the Navier-Stokes equations

$$\frac{\partial \vec{u}}{\partial t} = \vec{u} \times \vec{\omega} - \nabla \pi + \frac{1}{Re} \nabla^2 \vec{u} \tag{2.1}$$

subject to the incompressibility constraint

$$\nabla \cdot \vec{u} = 0 \tag{2.2}$$

where $\vec{\omega} = \nabla \times \vec{u}$ is the vorticity and $\pi = p + \frac{z}{Fr^2} + \frac{1}{2} \mid \vec{u} \mid^2$ is the dynamic pressure head. These equations were combined to give a second order equation for the normal component of vorticity and a fourth order equation for the normal component of velocity

$$\frac{\partial \omega_z}{\partial t} = \vec{k} \cdot \nabla \times (\vec{u} \times \vec{\omega}) + \nu \nabla^2 \omega_z \tag{2.3}$$

$$\frac{\partial \nabla^2 w}{\partial t} = -\vec{k} \cdot \nabla \times \nabla \times (\vec{u} \times \vec{\omega}) + \nu \nabla^4 w \tag{2.4}$$

In addition, in order to provide direct comparisons with experimental flow visualization studies, a passive scalar with a Schmidt number of 0.7 was imposed on the initial jet profile and its evolution was tracked by solving the scalar transport equation

$$\frac{\partial c}{\partial t} + \vec{u}.\nabla c = \frac{1}{Re.Sc} \nabla^2 c \tag{2.5}$$

2.2 Boundary Conditions

Periodic boundary conditions were imposed in the homogeneous (x) direction. The assumed periodicity length was chosen to be $L_x/R_o = 16\pi/\alpha$, where $\alpha = 2.85$ corresponds to the wavenumber of the least stable (axisymmetric) eigenmode of the initial laminar profile. Figure 2.2 shows the least stable eigenmodes of the initial laminar profile (equation 2.18) as computed by a solution of the linearized stability equations (Kambe, 1969; Lessen and Singh, 1973). The details are described in Appendix C. As shown in Figure 2.2, both axisymmetric and helical modes are

nearly equally amplified at this wavenumber. The periodicity length of $16\pi/\alpha$ was chosen to accommodate the development of not only the fundamental mode, but also two successive subharmonics. Based on available experimental data on the two-point longitudinal correlation lengths in turbulent round jets (Wygnanski and Fiedler, 1969) this domain is also large enough to ensure that the two-point statistics of the fully-developed turbulent jet are uncorrelated at a separation of one half the domain length in the streamwise direction. The flow was assumed to be quiescent ($\vec{u} = 0$) at large distances away from the jet ($y = \pm\infty$ and $z = \infty$), while at the free surface ($z = 0$) the linearized free-surface boundary conditions were imposed

$$\frac{\partial h}{\partial t} + u\frac{\partial h}{\partial x} + v\frac{\partial h}{\partial y} = w \tag{2.6}$$

$$\frac{\partial u}{\partial z} + \frac{\partial w}{\partial x} = 0 \tag{2.7}$$

$$\frac{\partial v}{\partial z} + \frac{\partial w}{\partial y} = 0 \tag{2.8}$$

$$p + \frac{h}{Fr^2} = \frac{2}{Re}\frac{\partial w}{\partial z} \tag{2.9}$$

where h is the surface elevation.

Boundary conditions 2.7 and 2.8, can be combined to obtain boundary conditions for ω_z and w by using the continuity equation, leading to

$$\frac{\partial \omega_z}{\partial z} = 0 \tag{2.10}$$

$$\frac{\partial^2 w}{\partial z^2} = \frac{\partial^2 w}{\partial x^2} + \frac{\partial^2 w}{\partial y^2} \tag{2.11}$$

2.3 Discretization and Numerical Solution

The computations were performed using standard pseudospectral methods (Canuto et al. 1987) employing Fourier series in the streamwise (x) direction and mapped Chebyshev polynomials in the spanwise (y) and normal (z) directions.

$$\mathbf{v}(\mathbf{x},t) = \sum_{p=0}^{P}\sum_{n=0}^{N}\sum_{m=-M/2}^{M/2} \hat{\mathbf{v}}(m,n,p,t)e^{iamx}T_n(y)T_p(z) \tag{2.12}$$

Two algebraic mappings

$$\frac{y}{R_o} = \frac{A\zeta}{(1-\zeta^4)^{1/4}} \tag{2.13}$$

and

$$\frac{z}{R_o} = \frac{B(1-\zeta)^{1/2}}{(1+\zeta)^{1/2}} \tag{2.14}$$

were used to map the $-\infty \leq y/R_o \leq \infty$ and $0 \leq z/R_o \leq \infty$ physical domain to the $-1 \leq \zeta \leq 1$ domain of Chebyshev polynomials. The scale factors $A = 5.0$ and $B = 9.6$ were chosen to produce a nearly uniform distribution of grid points in the central portion of the jet and a more concentrated distribution of grid points near the free surface. In the computations the so-called 3/2 rule was used to de-alias all the variables.

Time advancement was carried out by a semi-implicit full-step time-stepping scheme (Orszag and Patera 1983), involving explicit evaluation of the convective terms using a second-order Adams-Bashforth scheme and an implicit evaluation of the viscous terms using a Crank-Nicholson scheme.

$$\frac{\omega_z^{n+1}-\omega_z^n}{\Delta t} = \vec{k}\cdot\frac{3}{2}(\nabla\times(\vec{u}\times\vec{\omega}))^n - \frac{1}{2}(\nabla\times(\vec{u}\times\vec{\omega}))^{n-1} + \frac{\nu}{2}\nabla^2(\omega_z^{n+1}+\omega_z^n) \tag{2.15}$$

$$\frac{\nabla^2(w^{n+1}-w^n)}{\Delta t} = -\vec{k}\cdot\nabla\times\nabla\times(\frac{3}{2}(\vec{u}\times\vec{\omega})^n - \frac{1}{2}(\vec{u}\times\vec{\omega})^{n-1}) + \frac{\nu}{2}\nabla^4(w^{n+1}+w^n) \tag{2.16}$$

At each step, h was computed according to

$$\frac{h^{n+1}-h^n}{\Delta t} = \frac{3}{2}(-u\frac{\partial h}{\partial x} - v\frac{\partial h}{\partial y})^n - \frac{1}{2}(-u\frac{\partial h}{\partial x} - v\frac{\partial h}{\partial y})^{n-1} + \frac{1}{2}(w^{n+1}+w^n) \qquad (2.17)$$

These equations were solved subject to boundary conditions given by equations 2.10 and 2.11, and quiescent conditions far from the jet. One additional free-surface boundary condition for w, required in the solution of the viscous term in equation 2.16 was obtained from equation 2.9 by using the normal component of the Navier-Stokes equations as

$$\frac{\partial^2 w}{\partial t \partial z} = -\frac{\partial}{\partial x}\vec{i}\cdot(\vec{u}\times\vec{\omega}) - \frac{\partial}{\partial y}\vec{j}\cdot(\vec{u}\times\vec{\omega}) + \frac{\partial^2 \pi}{\partial x^2} + \frac{\partial^2 \pi}{\partial y^2} + \nabla^2\frac{\partial w}{\partial z} \qquad (2.18)$$

The fourth order equation for w (2.16) was solved by decoupling it into two second order Poisson operators and imposing the boundary conditions (2.11) and (2.17) using an analytical Green's function technique (Domaradzki, 1990) (see Appendix A).

The resulting second-order Poisson operators were inverted using a collocation/ diagonalization technique (Haidvogel and Zang, 1979; Haldenwang et al., 1984). Each Poisson solver requires $O(NX \cdot NY \cdot NZ^2 + NX \cdot NY^2 \cdot NZ)$ operations, roughly twice as many operations as in a Fourier/Fourier/Chebyshev code. The application of the diagonalization procedure using the Green's function approach is detailed in Appendix A.

These methods lend themselves to high efficiency parallel implementation on medium-grained distributed memory parallel processors (Mangiavacchi and Akhavan, 1993). The only operation that requires communication is the evaluation of the multi-dimensional FFT's, which can be computed using a transpose algorithm. A description of the parallel implementation of the Fourier-Double Chebyshev code on a message-passing architecture is given on Appendix B.

Resolution	Ny=Nz=128		
α	σ_{N-S}	σ_{O-S}	% error
1.0	0.2664884	0.266490	6×10^{-4}
2.0	0.4692816	0.469300	4×10^{-3}
3.0	0.5135206	0.513540	3.5×10^{-3}
4.0	0.4332315	0.433232	1.1×10^{-4}
5.0	0.2509230	0.250924	3×10^{-4}

Table 2.1: Quantitative comparison between the growth rates of the least stable eigenmodes of the linearized equation for a free round jet from the solution of the Navier-Stokes equations to the growth rates predicted from solution of the linearized equation (Appendix C).

2.4 Tests of the Code

A number of test problems have been conducted to ensure the accuracy of the numerical schemes. Individual routines were tested for accuracy by comparing with analytical results. The complete code was tested by comparing the evolution of the most unstable axisymmetric mode to the solution of the linearized viscous stability (the Orr-Sommerfeld) equations. The details are described in Appendix C. To perform the tests, the Navier-Stokes solver was initialized with a laminar jet profile (equation 2.18), on which a pure mode of the Orr-Sommerfeld equation was superimposed. Figure 2.3 shows a comparison between the growth rates of the least stable eigenmodes of the linearized stability equation for a free round jet computed from the solution of the Navier-Stokes equations to the growth rates predicted from direct solution of the linearized equation. Excellent agreement is seen between the two results. Table 2.1 shows a quantitative comparison between the results.

The linearized free-surface boundary conditions were verified by comparing the period P of small amplitude sinusoidal standing waves of wavelength k with the predictions from linear theory,

$$P = \frac{2\pi}{\sqrt{gk}}$$

where g is the gravity acceleration. The error in the period was found to be smaller than 1.0% when using a time step compatible with the simulations.

2.5 Initial Conditions

Initial conditions for the runs were specified as a laminar jet with a blunt velocity profile

$$U/U_o = 0.5\{1 + \tanh[6.25(1 - r/R)]\} \tag{2.19}$$

on which a divergence-free, random noise disturbance field given by

$$\mathbf{u}'(\mathbf{x}) = \nabla \times (\mathbf{\Phi}(\mathbf{x}) \cdot I(r)) \tag{2.20}$$

was superimposed. Here $\mathbf{\Phi}$ is a three-dimensional isotropic random disturbance field (Rogallo, 1981) whose spectral components were chosen to give $\mathbf{u}'$ an energy spectrum

$$E(k) = (\frac{\Lambda}{1 + k^2\Lambda^2}) \tag{2.21}$$

The experimental data of Wygnanski and Fiedler (1969) were used to choose the value of $\Lambda = 0.45R_o$ and the profile of $I(r) = \exp(-1.9r^2/R_o^2)$. The initial disturbance field had an energy of 10^{-4} relative to that of the mean flow. The passive scalar field was initialized with a profile identical to that of the mean flow (equation 2.18). No disturbances were imposed on the passive scalar.

The temporally-growing round jet was issued at depths ranging from one to two jet diameters below the free surface (H/D = 1.0, 1.5, and 2.0). A relatively low

Froude number jet was studied ($Fr = \frac{U}{\sqrt{gD}} = 0.10$, based on initial jet centerline velocity and jet diameter). This prevents the production of large amplitude waves and allowed us to use the linearized free-surface boundary conditions in our simulations, thus resulting in significant savings in the required computational resources. For the scope of this study, the free surface is assumed to be clean of surfactants and surface tension effects are assumed to be negligible.

Simulations were carried out with a resolution of $128 \times 129 \times 129$ de-aliased modes in the streamwise, spanwise and normal directions on a partition of the SDSC 400-node Intel Paragon. The turbulent jet had a turbulent Reynolds number of $\approx 10,000$ based on initial jet diameter and centerline velocity, and a final $Re_\lambda \approx 100$ based on longitudinal Taylor microscale ($Re_{\lambda_g} \approx 75$). At this time, the grid spacing was on the order of 3 Kolmogorov scales in the central portion of the jet.

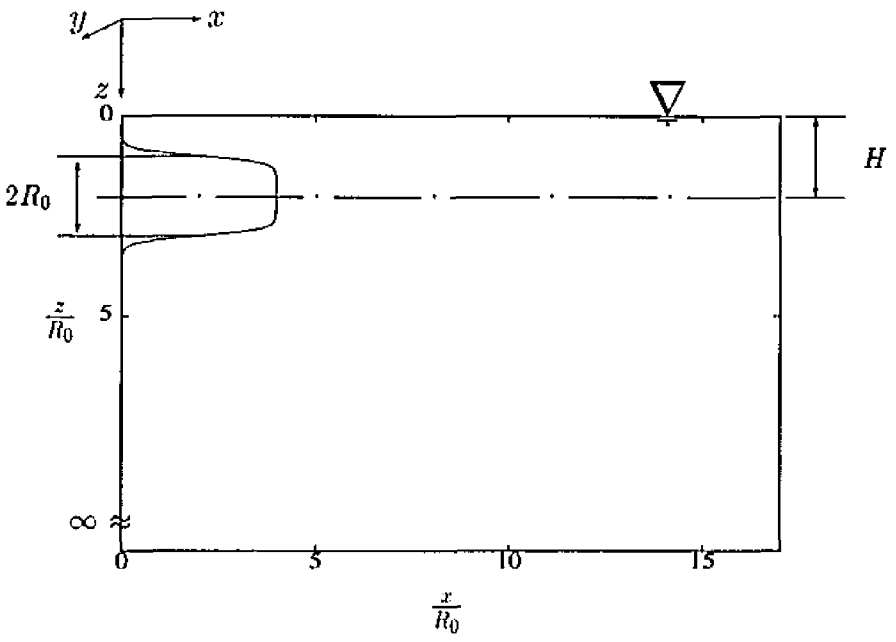

Figure 2.1: Schematic of the jet and of the coordinate system

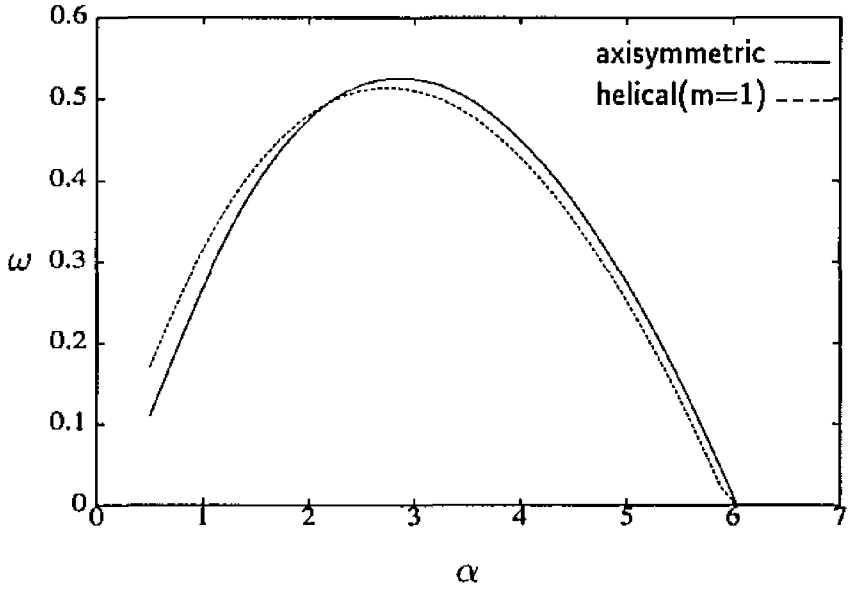

Figure 2.2: Growth rates of axisymmetric and helical modes in the initial laminar profile as a function of the disturbance wavenumber

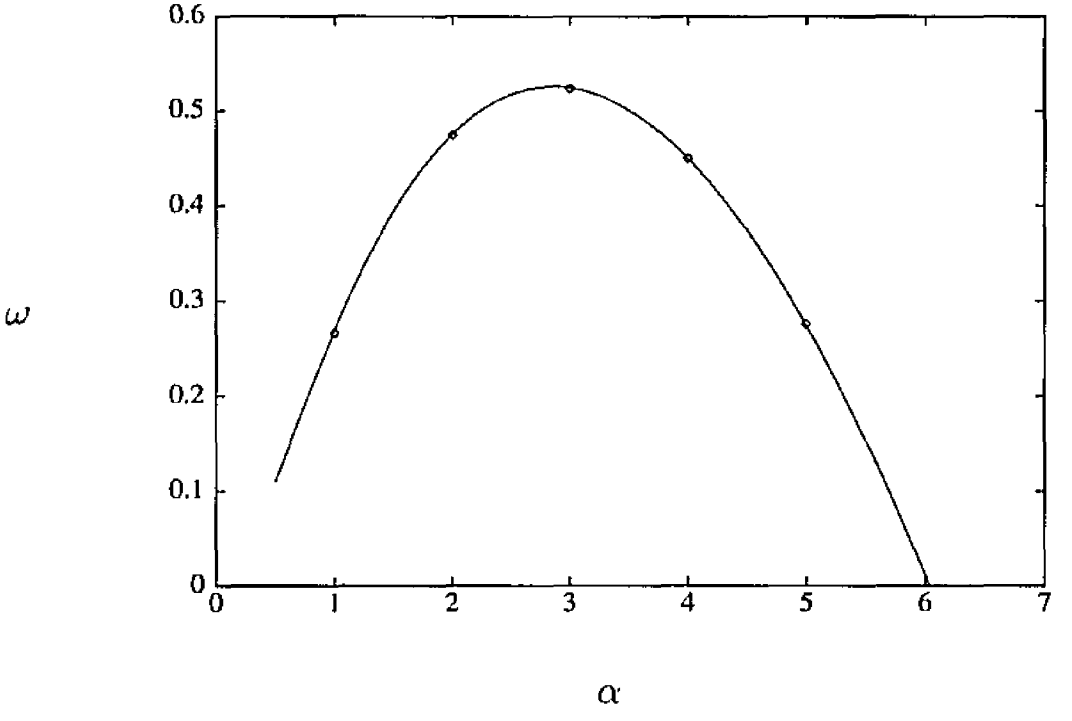

Figure 2.3: Comparison of the growth rates (ω) of the least stable eigenmode of the blunt velocity profile (equation 2.18) from the solution of Navier-Stokes equations ($\diamond$), to the predicted value from the solution of the linearized stability equation C.10-C.12,(solid line) for various wavenumbers α

CHAPTER III

INITIAL EVOLUTION

The evolution of the free-surface jet flow from a laminar to a fully developed turbulent state is discussed in this chapter. For the jets studied here, which were all issued at a depth of $H/D \geq 1.0$, the early stages of the evolution of the jet are not significantly affected by the presence of the free-surface. Similar to a free jet, the random disturbances that are superimposed on the base flow initially grow as a result of linear interactions with the base profile. The growth and saturation of these disturbances results in the formation of axisymmetric vortex rings, which undergo a rapid secondary instability and result in the transition of the jet to a turbulent state. As the jet grows and approaches the free-surface, the growth, evolution and vortical structure of the flow is influenced by the presence of the free-surface. In this chapter, we review the evolution and growth of the jet and compare the results with analytical predictions as well as experimental measurements, in submerged and free jets.

3.1 Vorticity and Passive Scalar Fields

The initial evolution of the free-surface jet can be visualized with the help of three-dimensional iso-surfaces of constant value vorticity and passive scalar fields.

The resulting images are useful in observing the general features of the flow, such as the large scale structure of the flow.

Figures 3.1-3.12 show the evolution of the vorticity and passive-scalar fields for the free-surface jet issued at one diameter below the free surface (i.e. with $H/D = 1.0$). It is also shown in these figures the surface elevation, which was amplified for the scope of the visualization. The actual amplitude of the surface elevation is very small for the present simulations (on the order of 10^{-3}). Since the level of the random noise present in the initial velocity profile is very small ($E \sim 10^{-4}$) the initial vorticity and passive scalar fields at tU_o/R_o=0 (Figures 3.1 and 3.2) are composed of isosurfaces that are almost perfectly cylindrical. As the most linearly unstable modes begin to grow, the cylindrical surfaces begin to undulate (see Figures 3.3 and 3.4). The initial structures formed from the saturation of the most linearly unstable modes are in the form of axisymmetric vortex rings (Figure 3.5). These correspond to mushroom shaped structures in the passive scalar field (Figure 3.6). Subsequent evolution of these structures involves the instability of these vortex rings to azimuthal perturbations, already visible in Figure 3.5, the development of helical modes and pairings between various vortical structures. In particular, the structure of the vorticity field at this time shows the presence of an azimuthal mode with $m = \pm 5$, the development of asymmetry due to the presence of a helical mode with $m = 1$ and symmetric as well as asymmetric pairings between the various vortical structures. The azimuthal instabilities rapidly lead to the formation of braids, that are streamwise vortex tubes, strengthened during the vortex pairings, thus resulting in rapid transition to small-scale turbulence.

In contrast to the planar jet and the mixing layer, more than one pairing of the axisymmetric vortex rings is rarely seen in round jets. After the first pairing, azimuthal

modes become very strong considerably increasing the level of three-dimensionality in the jet and thus triggering the transition to turbulence before the next pairing has a chance to occur. These azimuthal modes have also been observed in a number of experimental and numerical studies (Liepmann and Gharib, 1992; Abid and Brachet, 1993; and and Brancher et al 1994) are belived to be precursors to ejections of fluid from the sides of the jet, known as side jets. Traces of all these effects can be observed in the structure of the vorticity and passive scalar fields at $tU_o/R_o = 20$ (figures 3.7-3.8). By $tU_o/R_o = 40$ (Figures 3.9-3.10), the jet has reached a fully turbulent state. The development of the shallow jet beyond this time is strongly influenced by the presence of the free surface (Figures 3.11-3.12). Among other effects, this interaction leads to significantly higher spreading rates of the jet in the lateral direction in a shallow layer near the free surface (Figures 3.11-3.12). This phenomenon, known as the surface current, has also been observed in a number of experimental studies of free-surface jet (Madnia and Bernal 1989, Anthony et al. 1991, Anthony and Willmarth 1992).

That this spreading is caused by the presence of the free surface can be verified by comparing the passive scalar and vorticity fields at tU_o/R_o =80 for H/D =1 (Figures 3.11-3.12) with that of H/D =1.5 (Figures 3.13-3.14) and H/D =2 (Figures 3.15-3.16). For these two cases, the free-surface effect is much smaller and the lateral spreading of the jet near the free-surface is considerably smaller.

3.2 Evolution of the Jet

The overall evolution of the free-surface jet with time is shown in Figures 3.17-3.19. The growth of the free-surface jet (H/D =1.0, 1.5, and 2.0) is tracked by following the time histories of the jet half-widths in the vertical and transverse directions

$z_{1/2}(t)$, in Figure 3.17, and $y_{1/2}(t)$ in Figure 3.18), defined as the distance between the location of the maximum mean velocity and the locations along vertical and transverse planes where the mean velocity has dropped to half the maximum value. Also shown in Figure 3.17 are the time histories of the maximum mean jet velocity, $U_c(t)$, and the jet Reynolds number, $Re_{z_{\frac{1}{2}}} = \frac{z_{\frac{1}{2}} U_c}{\nu}$, normalized with respect to the initial Reynolds number of the jet, $Re_o = \frac{R_o U_o}{\nu}$.

The interval between $0 < tU_o/R_o < 15$ represents the growth and saturation of the most unstable modes of the initial disturbance field. During this period, the sharp shear layers at the edges of the jet grow by viscous diffusion and the jet becomes less blunt. Nevertheless, since an inviscid core continues to exist at the center of the jet, the jet half-width and the centerline velocities are not affected. The time $tU_o/R_o \sim 15$ signifies the start of the first vortex pairing in the jet, after which the jet experiences rapid transition to small-scale turbulence. By a time of $tU_o/R_o \sim 40$, the jet has become fully turbulent. This time also represents the start of the interaction between the jet and the free surface, for the shallow jet case (H/D =1.0). In general, the effect of the free surface is felt when the jet is about on-half radius from the surface. As seen in Figure 3.17 and 3.18, the evolution of the shallow jet (H/D =1.0) is dramatically different from that of the deeper jet (H/D =2.0) beyond this point. While the deep jet (H/D =2.0) still behaves as a free jet and gradually approaches a self-similar fully-developed turbulent state, the shallow jet experiences a rapid rise in its vertical jet half-width upon first interaction with the free surface at $tU_o/R_o \sim 30$. This is accompanied by a simultaneous decrease in the transverse jet width (Figure 3.17). These trends are reversed later on (beyond $tU_o/R_o \sim 60$ when the free-surface jet begins to approach a self-similar state. In the final fully-developed turbulent free-surface jet ($tU_o/R_o > 85$), the transverse jet half-width is nearly 50% larger than

the half-width in the vertical direction. The same trends are also observed for the (H/D =1.5) jet, but at later times. These results are consistent with experimental measurements in free-surface jets (Madnia and Bernal 1989, Anthony and Willmarth 1992).

Figure 3.19 shows a comparison of $z_{1/2}(t)$, $y_{1/2@z=z_m}(t)$, and $y_{1/2@z=0}(t)$, for the case of the shallow jet H/D =1.0. The plane $z = z_m$ is the horizontal plane that cuts through the point of maximum mean streamwise velocity, while $z = 0$ is at the surface. This figure shows clearly how the jet first grows in the vertical direction, then in the horizontal direction, and finally, the spreading of the jet is maximum at the surface.

The initial vertical spread observed in the shallow jets may be attributed to the effect of the the free surface on the initial perturbations of the laminar jet. The presence of the free surface introduces the observed helical and azimuthal perturbations with m=1, that can cause the jet to grow preferentially in the vertical direction by means of ejections or side jets. This initial growth in the vertical direction has also been observed by Liepmann and Gharib (1992) using DPIV on a free-surface jet issued parallel to the surface at H/D=1, showing that during the initial evolution, the jet becomes elongated vertically.

In the deeper jet, the spread of the jet for $70 < tU_o/R_o < 200$ is consistent with the existence of self-preserving profiles for the mean velocity and the Reynolds shear stress of the form,

$$\frac{U(r,t)}{U_c(t)} = f(\frac{r}{r_{1/2}(t)}) \tag{3.1}$$

$$\frac{-\overline{u_x' u_r'}(r,t)}{U_c^2(t)} = g(\frac{r}{r_{1/2}(t)}) \tag{3.2}$$

Substitution of these expressions into the equation of motion

$$\frac{\partial U}{\partial t} = -\frac{\partial \overline{(u'_x u'_r)}}{\partial r} \tag{3.3}$$

and the momentum integral constraint

$$\frac{d}{dt}\int_0^\infty \rho\, U(r,t)\, r\, dr = 0 \tag{3.4}$$

leads to the conclusion that under conditions of self-preservation, $r_{1/2}(t) \sim (t-t_o)^{1/3}$ and $U_c(t) \sim (t-t_o)^{-2/3}$, consistent with the evolution of the deep jet beyond $tU_o/R_o \sim 70$. The evolution of the *temporally* growing round turbulent jet is, therefore, different from that of *spatially* growing round turbulent jets, for which self-preservation requires that the jet radius-width grow as $r_{1/2} \sim (x-x_o)$ while its centerline velocity drops as $(x-x_o)^{-1}$ resulting in a Reynolds number which is constant (Tennekes & Lumley 1972).

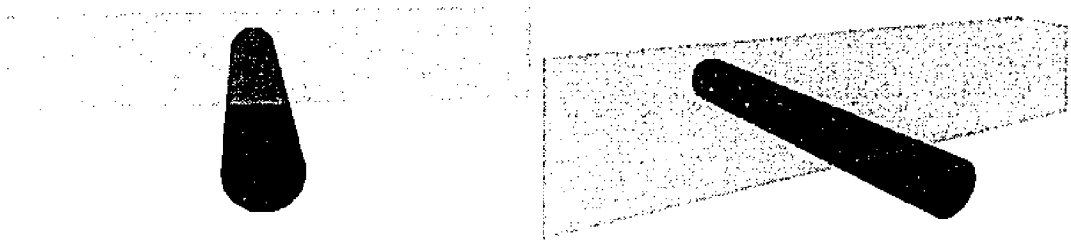

Figure 3.1: Isosurfaces of vorticity magnitude, $|\omega|/|\omega_{max}|$ =0.5 ($|\omega|D/U_o = 1.5$), H/D =1.0, at $tU_o/R_o = 0$. The initial surface elevation is $h(x, y, t = 0) = 0$

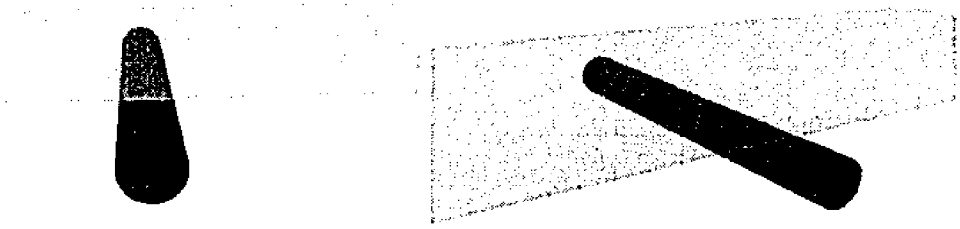

Figure 3.2: Isosurfaces of passive scalar, c/c_{max} =0.5 ($c/c_o = 0.5$), H/D =1.0, at $tU_o/R_o = 0$.

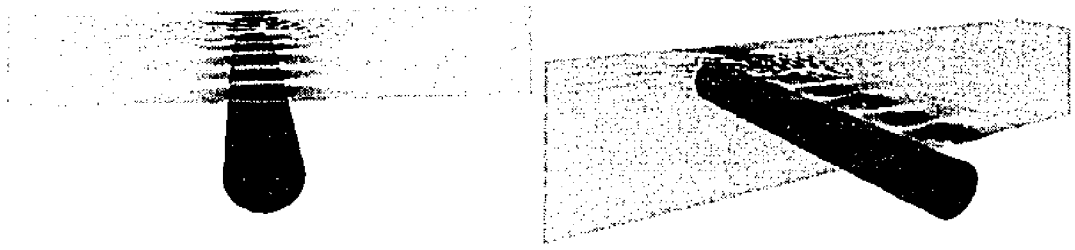

Figure 3.3: Isosurfaces of vorticity magnitude, $|\omega|/|\omega_{max}|$ =0.5 ($|\omega|D/U_o = 2.0$), H/D =1.0, at $tU_o/R_o = 10$. The maximum surface elevation is $h/R_o = 4.5 \times 10^{-5}$, and was magnified to 0.3 for visualization purposes.

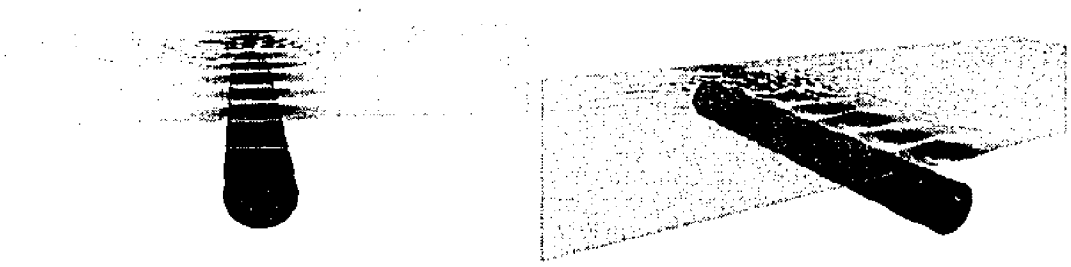

Figure 3.4: Isosurfaces of passive scalar, c/c_{max} =0.5 ($c/c_o = 0.5$), H/D =1.0, at $tU_o/R_o = 10$. The maximum surface elevation is $h/R_o = 4.5 \times 10^{-5}$, and was magnified to 0.3 for visualization purposes.

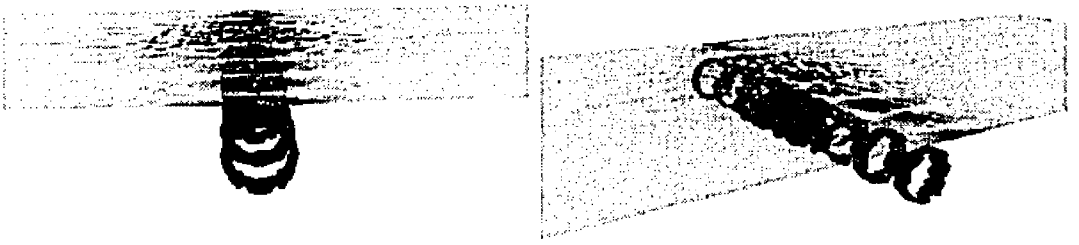

Figure 3.5: Isosurfaces of vorticity magnitude, $|\omega|/|\omega_{max}|$ =0.5 ($|\omega|D/U_o = 2.4$), H/D =1.0, at $tU_o/R_o = 15$. The maximum surface elevation is $h/R_o = 4.5 \times 10^{-4}$, and was magnified to 0.3 for visualization purposes.

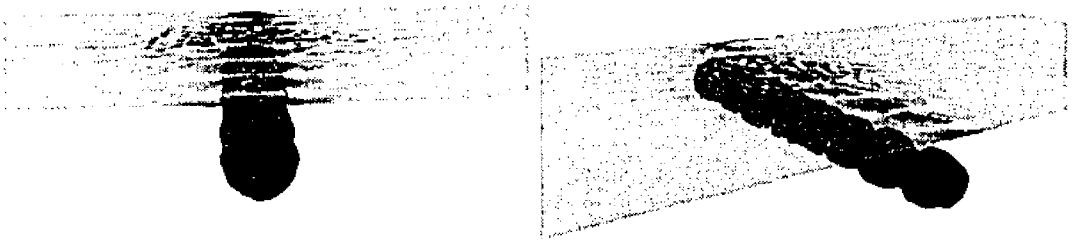

Figure 3.6: Isosurfaces of passive scalar, c/c_{max} =0.5 ($c/c_o = 0.5$), H/D =1.0, at $tU_o/R_o = 15$. The maximum surface elevation is $h/R_o = 4.5 \times 10^{-4}$, and was magnified to 0.3 for visualization purposes.

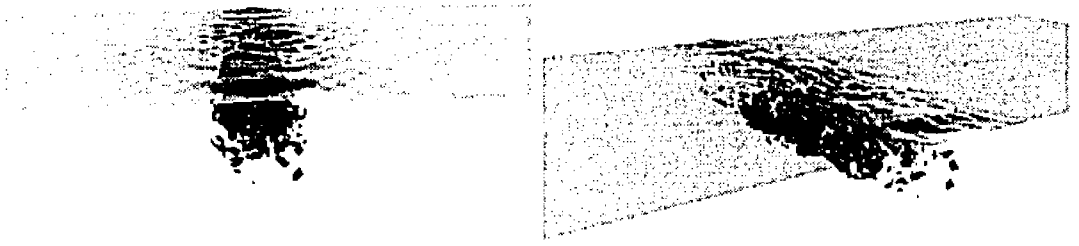

Figure 3.7: Isosurfaces of vorticity magnitude, $|\omega|/|\omega_{max}|$ =0.5 ($|\omega|D/U_o$ = 4.0), H/D =1.0, at $tU_o/R_o = 20$. The maximum surface elevation is $h/R_o = 1.25 \times 10^{-3}$, and was magnified to 0.3 for visualization purposes.

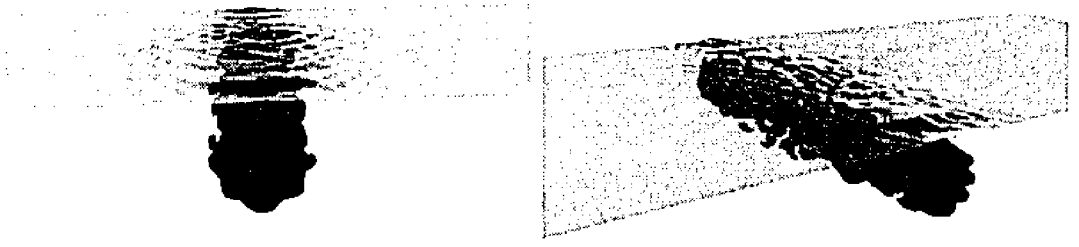

Figure 3.8: Isosurfaces of passive scalar, c/c_{max} =0.5 (c/c_o = 0.5), H/D =1.0, at $tU_o/R_o = 20$. The maximum surface elevation is $h/R_o = 1.25 \times 10^{-3}$, and was magnified to 0.3 for visualization purposes.

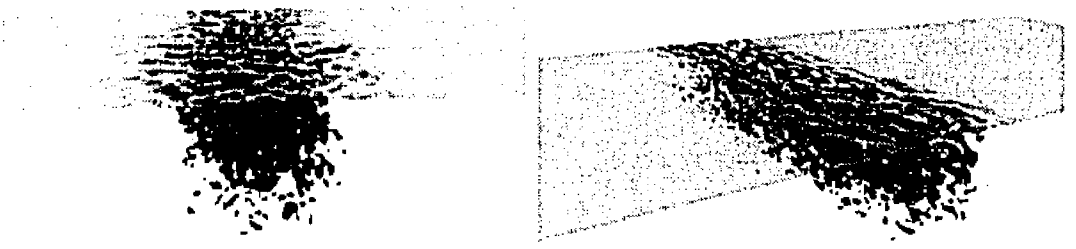

Figure 3.9: Isosurfaces of vorticity magnitude, $|\omega|/|\omega_{max}|$ =0.5 ($|\omega|D/U_o = 3.0$), H/D =1.0, at $tU_o/R_o = 40$. The maximum surface elevation is $h/R_o = 1.90 \times 10^{-3}$, and was magnified to 0.3 for visualization purposes.

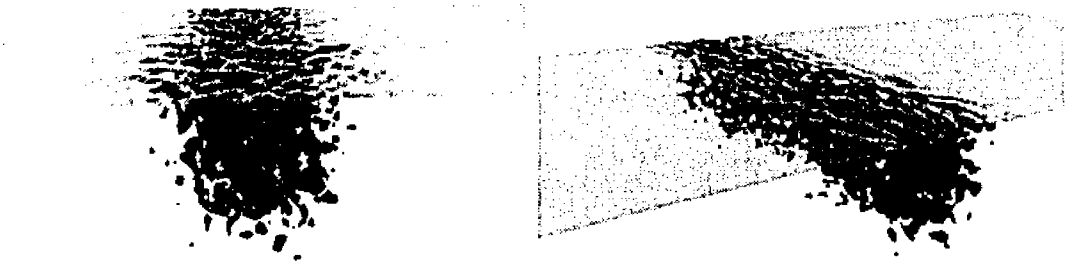

Figure 3.10: Isosurfaces of passive scalar, c/c_{max} =0.5 ($c/c_o = 0.36$), H/D =1.0, at $tU_o/R_o = 40$. The maximum surface elevation is $h/R_o = 1.90 \times 10^{-3}$, and was magnified to 0.3 for visualization purposes.

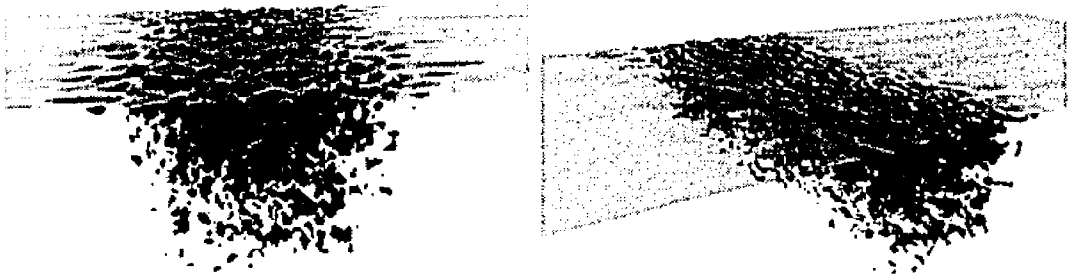

Figure 3.11: Isosurfaces of vorticity magnitude, $|\omega|/|\omega_{max}|$ =0.5 ($|\omega|D/U_o = 1.5$), H/D =1.0, at $tU_o/R_o = 80$. The maximum surface elevation is $h/R_o = 5.31 \times 10^{-4}$, and was magnified to 0.3 for visualization purposes.

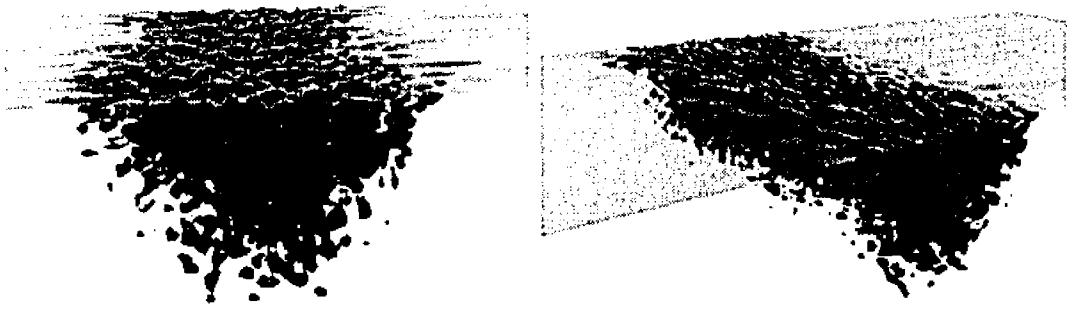

Figure 3.12: Isosurfaces of passive scalar, c/c_{max} =0.5 ($c/c_o = 0.25$), H/D =1.0, at $tU_o/R_o = 80$. The maximum surface elevation is $h/R_o = 5.31 \times 10^{-4}$, and was magnified to 0.3 for visualization purposes.

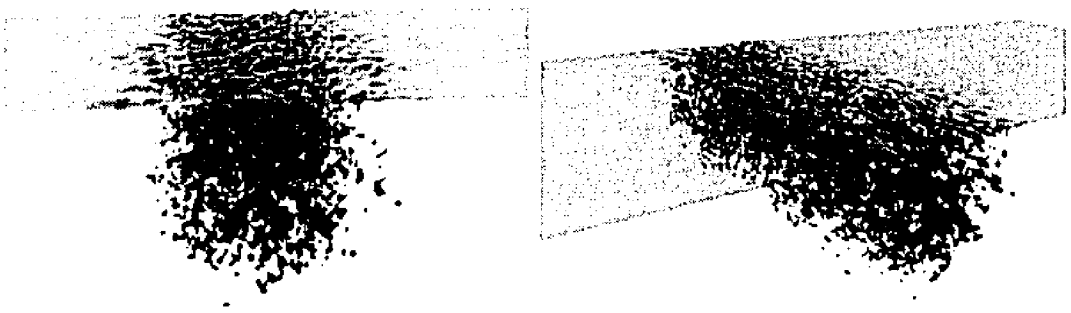

Figure 3.13: Isosurfaces of vorticity magnitude, $|\omega|/|\omega_{max}|$ =0.5 ($|\omega|D/U_o = 1.5$), H/D =1.5, at $tU_o/R_o = 80$. The maximum surface elevation is $h/R_o = 4.46 \times 10^{-4}$, and was magnified to 0.3 for visualization purposes.

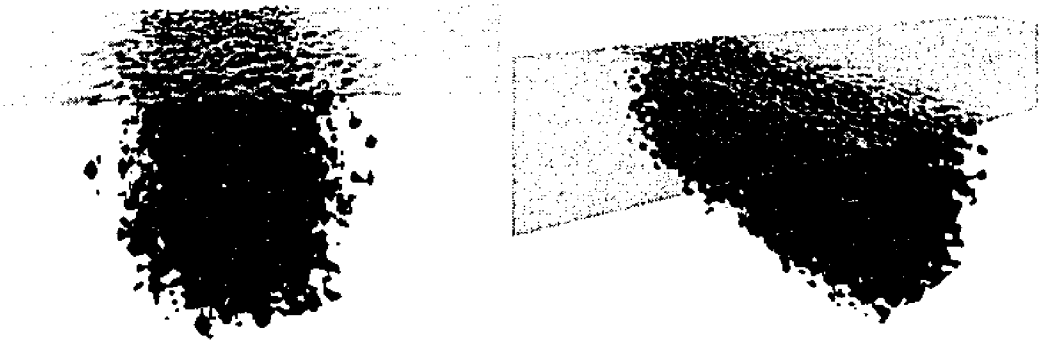

Figure 3.14: Isosurfaces of passive scalar, c/c_{max} =0.25 ($c/c_o = 0.5$), H/D =1.5, at $tU_o/R_o = 80$. The maximum surface elevation is $h/R_o = 4.46 \times 10^{-4}$, and was magnified to 0.3 for visualization purposes.

Figure 3.15: Isosurfaces of vorticity magnitude, $|\omega|/|\omega_{max}|$ =0.5 ($|\omega|D/U_o = 1.5$), H/D =2.0, at $tU_o/R_o = 80$. The maximum surface elevation is $h/R_o = 3.65 \times 10^{-4}$, and was magnified to 0.3 for visualization purposes.

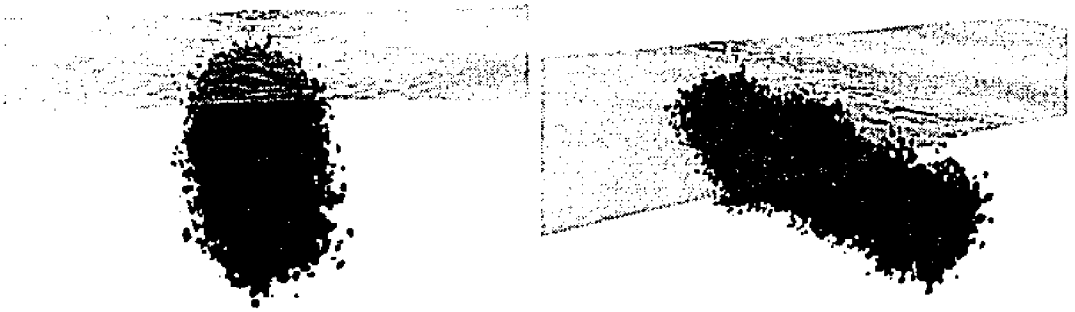

Figure 3.16: Isosurfaces of passive scalar, c/c_{max} =0.25 ($c/c_o = 0.5$), H/D =2.0, at $tU_o/R_o = 80$. The maximum surface elevation is $h/R_o = 3.65 \times 10^{-4}$, and was magnified to 0.3 for visualization purposes.

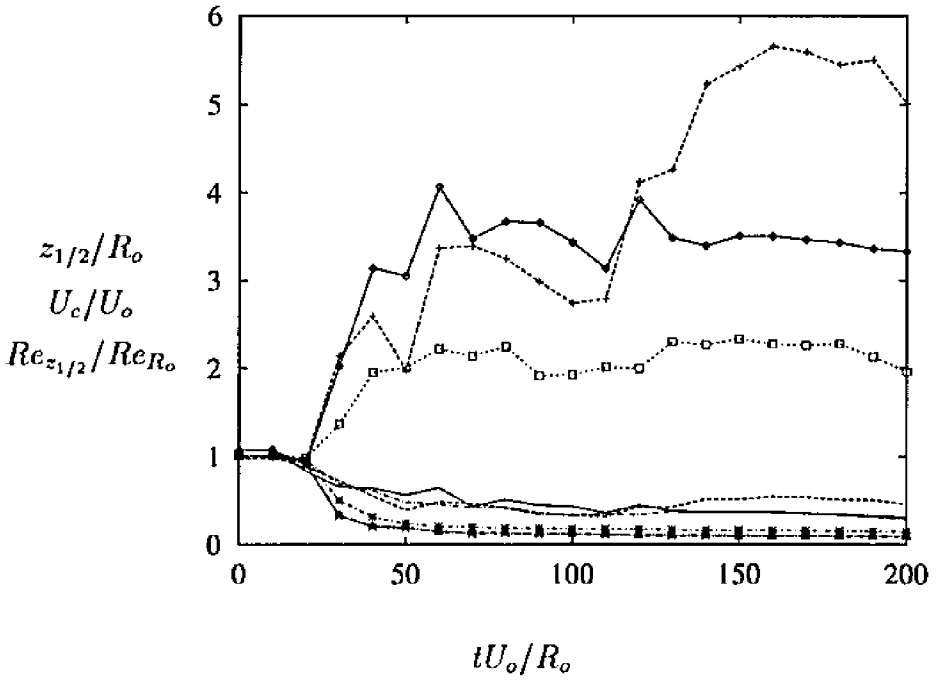

Figure 3.17: Evolution of the free-surface jet centerline velocity and half-width in the normal direction. $\diamond$, $z_{1/2}/R_o$, $H/D = 1.0$; $+$, $z_{1/2}/R_o$, $H/D = 1.5$; $\square$, $z_{1/2}/R_o$, $H/D = 2.0$; $\times$, U_c/U_o, $H/D = 1.0$; $\triangle$, U_c/U_o, $H/D = 1.5$; $*$, U_c/U_o, $H/D = 2.0$, —, $Re_{z_{1/2}}/Re_{R_o}$, $H/D = 1.0$; – – – –, $Re_{z_{1/2}}/Re_{R_o}$, $H/D = 1.5$; – · – · –·, $Re_{z_{1/2}}/Re_{R_o}$, $H/D = 2.0$.

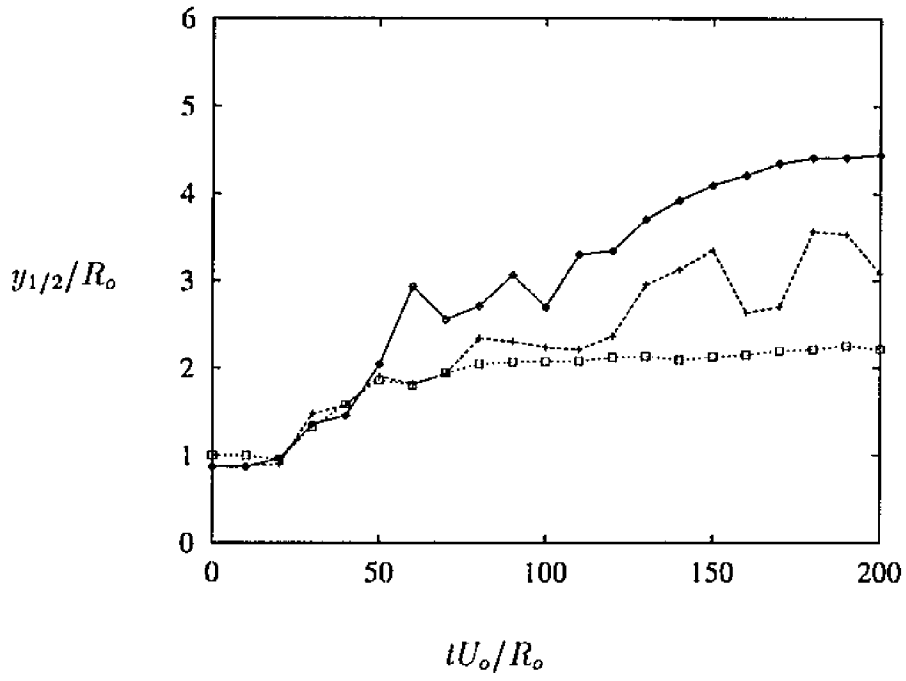

Figure 3.18: Evolution of the free-surface jet half-width in the transverse direction. $\diamond$, $y_{1/2}/R_o$, $H/D = 1.0$; $+$, $y_{1/2}/R_o$, $H/D = 1.5$; $\square$, $y_{1/2}/R_o$, $H/D = 2.0$.

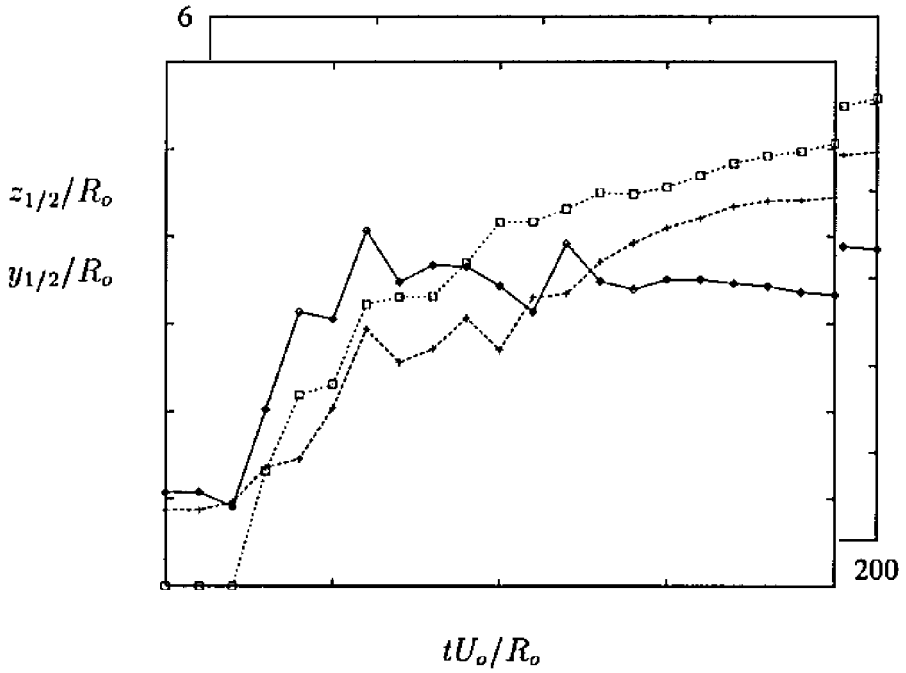

Figure 3.19: Evolution of the free-surface jet half-width, $H/D = 1.0$. $\diamond$, $z_{1/2}/R_o$; $+$, $y_{1/2}/R_o$, at $z = z_m$; $\square$, $y_{1/2}/R_o$, at $z = 0$.

CHAPTER IV

STATISTICS OF THE FREE SURFACE TURBULENT JET

In this chapter, the statistics and large scale structure of the simulated turbulent free-surface jet is presented and the results are compared to existing experimental data. This will help characterize the present database which will be used in the following chapters to study the structure and dynamics of free-surface turbulence. Three cases will be discussed; a deep jet issued at (H/D =2.0), and two shallow jets (H/D =1.5, H/D =1.0).

4.1 The Deep Jet

4.1.1 Mean Velocity Profiles

The profiles of mean velocity in the deep turbulent jet (H/D =2.0), plotted as a function of $(z - H)/L_z$, are shown in Figures 4.1 and 4.2 for $tU_o/z_o = 100$ and 150. Here H is the depth of the jet below the free surface and L_z is the vertical distance between the original centerline and the point where the velocity drops to half the centerline value. These profiles, as well as all other statistics discussed in this chapter, were calculated by temporal and spatial averaging of the Flow (in the x homogeneous direction) over a short time interval of $\Delta tU_o/R_o$=1. Since the computational domain contains only a few large-scale structures and due to the time-dependent nature of

the flow, the averaging can be done only over a short period of time, the statistics are not expected to fully converged and are somewhat noisy. Cleaner statistics can only be obtained by repeating the simulations a number of times with different random noise initial conditions and averaging the statistics over the different runs. This is a very expensive procedure and was attempted in the present study.

The early stages of the evolution of the jet is not significantly affected by the presence of the free surface. Figure 4.1 shows that even at $tU_o/R_o = 100$ the deep jet has barely begun to interact with the free surface and still shows an almost perfect axisymmetry. The mean velocity profile at this stage is in good agreement with the experimental data of (Wygnanski and Fiedler 1969) in self-preserving free turbulent jet as well as the Gaussian curve

$$\frac{U(z,t)}{U_c(t)} = e^{-0.693(r/r_{1/2})^2} \tag{4.1}$$

which represents the self-preserving mean velocity profile in a temporally-growing turbulent jet assuming a constant eddy viscosity ν_t. An exact agreement between the two sets of data, however, can not be expected, since spatially growing jets have a non-zero normal component of the mean velocity which is not present in the temporally growing jet.

After tU_o/R_o =100 the presence of the free surface begins to break the symmetry of the jet. At $tU_o/R_o = 150$ (Figure 4.2), the velocity profile in the upper-half of the jet is affected by the presence of the surface. The computed velocity profileat this time is seen to be in good agreement with the experimental of Anthony and Willmarth (1992) and Walker *etal* (1994). the free surface. The observed velocity profile is typical of the early stages of interaction of the jet with the free surface, when the mean velocity at the surface is less than $U_m/2$ (where U_m is the maximum

velocity); or equivalently, when the distance from the point of maximum velocity to the surface is larger than the half-radius.

Figure 4.3 shows the mean velocity profiles in the horizontal direction at tU_o/R_o =100 and tU_o/R_o =150, plotted as a function of $y/y_{1/2}$ (where $y_{1/2}$ represents the distance between the the point of maximum velocity and the point where the velocity drops to half the maximum value). The data is seen to be in excellent agreement with the free jet data of Wygnanski and Fiedler(1969) and the Gaussian curve which represents the similarity profile obtained analytically.

4.1.2 Turbulence Intensities and Reynolds Stresses

Figure 4.4 shows the distributions of the turbulence intensities and the Reynolds shear stress in the deep jet (H/D =2.0) at tU_o/R_o = 100 and 150 compared to the experimental measurements of Anthony and Willmarth (1992), and Walker *et al.* (1994) in spatially growing free-surface turbulent jets. Despite some oscillations in the numerical results, which are caused by the relatively small number of samples used in the computation of the statistics, the agreement with experimental data is seem to be quite good. The effect of the free surface is most prominantly felt in the vertical turbulence intensities. Here the presence of the free surface at low Froude numbers requires that the vertical turbulence intensities at the free surface nearly vanish. The distribution of the other components of the turbulence intensity as well as Reynolds shear stress are still quite symmetric and similar to those in a free jet.

As mentioned before, the deep jet results up to tU_o/R_o =150 are representative of the initial interaction of the jet with the free surface. Since the Reynolds number of the temporally growing jet decreases with time, the maximum time of the simulation is restricted to $tU_o/R_o \approx 200$, after which the Reynolds number becomes too small

to be representative of fully turbulent flows. On the other hand, this time is still not representative of the final stages of the interaction of the jet with the free surface. This interaction can be better observed by analyzing more shallow jets.

Figure 4.5 shows the distribution of the turbulence intensities and the Reynolds shear stress in the deep jet (H/D =2.0) at tU_o/R_o =100 and 150, in the plane $z = z_m$. The general features in the plane $z = z_m$ are qualitatively similar to those for the plane $y = 0$.

4.2 The Shallow Jets

The effect of the free surface is felt much earlier on the shallow (H/D =1.0 and 1.5) jets. Therefore, results of the simulation for these two cases at earlier times can be expected to have features that correspond to much later times of the deep (H/D =2.0) jet. It is convenient to compare the results of various depth jets at the same time when all jets have the same Reynolds number. for different depths to infer the effect of the free surface, and isolate it from effects of the decay of the jet Reynolds number. This will isolate the effect of the free surface on the evolution of the jet, independent of Reynolds number.

4.2.1 The Mean Velocity Profiles

The development of the mean velocity profile in the (H/D =1) free-surface jet is shown in Figure 4.6. Profiles of the mean velocity are presented along the vertical ($y_m = 0$) plane passing through the location of the maximum mean streamwise velocity in the jet. While the lateral location of the maximum mean streamwise velocity always remains in the center-plane of the original jet (i.e., the plane ($y_m = 0$)), the vertical $z = z_m$ location of this maximum begins to shift towards the free surface as the jet begins to interact with the free-surface. For the case of the H/D =1

jet this begins to happen at $tU_o/R_o \sim 40$, shortly after the jet experiences transition to turbulence. The maximum velocity reaches the free surface at $tU_o/R_o \sim 75$ (Figure 4.6) and remains there for the remainder of the evolution of the jet. figure 4.7 shows a comparison between the computed mean velocity profiles and the experimental data of Anthony and Willmarth. (1992) and Walker et al.(1994) at x/D=32. The agreement is quite good.

The lateral mean velocity profile in the jet is shown in Figure 4.8. The profile is in good agreement with the experimental data of Anthony and Willmarth (1992) and Walker et al.(1994) at x/D=32. The free jet data of Wygnanski and Fiedler(1969) along with the Gaussian curve are also shown. The good agreement between all curves shows that the jet grows like a free jet in the lateral direction.

The presence of the free surface results in the development of a secondary flow in the jet. Figure 4.9 shows the profiles of $V(y)$ in the plane $z = 0$ and $W(z)$ in the plane $y = 0$, respectively. The mean normal velocity W is seen to be negative on the centerplane of the jet (plane $y = 0$) causing an upwelling of the jet fluid towards the free surface. At the same time, the transverse velocity V in the plane $z = 0$ is seen to change sign on passing the centerplane of the jet. This behavior is caused by the development of a secondary flow, which is better visualized by means of contour plots of mean streamwise velocity and streamlines of secondary mean velocity shown in Figure 4.10. The predominant features of this secondary flow are two pairs of counter-rotating vortices, which pump the fluid towards the surface at the center plane of the jet and eject the fluid towards the edges of the jet at the surface. This secondary flow is of Prandtl's second kind; i.e., it arises from the anisotropy and non-uniformity in the normal and tangential Reynolds stresses. This can be shown by considering the equation of the streamwise mean vorticity which, for the temporally

growing free-surface jet analyzed here, reduces to

$$\frac{D\overline{\omega_x}}{Dt} = \frac{\partial^2}{\partial y \partial z}(\overline{w'^2} - \overline{v'^2}) + \frac{\partial^2 \overline{v'w'}}{\partial y^2} - \frac{\partial^2 \overline{v'w'}}{\partial z^2} + \nu(\frac{\partial^2 \overline{\omega_x}}{\partial y^2} + \frac{\partial^2 \overline{\omega_x}}{\partial z^2}) \qquad (4.2)$$

The last term on the right hand side of eq. 4.2 is a diffusive term and cannot generate mean streamwise vorticity. The anisotropy and spatial variation of the turbulent intensities and Reynolds shear stresses are, therefore, the main source of creation of a mean streamwise vorticity and development of a secondary flow. A similar secondary flow also develops in turbulent wall jets (Launder and Rodi 1983). The effect of the secondary flow on the profiles of mean streamwise velocity can be better visualized by means of contour plots of mean streamwise velocity, as shown in Figure 4.11. The effect of the secondary flow is to increase the spreading of the jet at the surface, creating thin a layer at the edges of the jet, also know as surface current.

Figures 4.12 and 4.13 show the mean velocity profiles in the vertical and horizontal directions respectively, for the case of the shallow jet (H/D =1.5). The features observed in this jet are similar to the case (H/D =1.0). Good agreement is seen also between these results and the experimental data of Anthony and Willmarth (1992) and Walker *et al.* (1994).

4.2.2 Turbulence Intensities and Reynolds Stresses

The evolution of the mean turbulence intensities and Reynolds stresses in the (H/D =1.0) free-surface jet is shown in Figures 4.14 through 4.16. At early times the turbulence statistics in the free-surface jet are indistinguishable from those which would be obtained in a free jet. As the jet begins to interact with the free surface, shortly after experiencing transition to turbulence, the presence of the free surface

inhibits the vertical velocity fluctuations ($\sqrt{\overline{w'^2}}$) within a thin 'surface layer' in the immediate vicinity of the free surface (see Figures 4.14c, 4.15c). Within this layer, the vertical turbulence kinetic energy is re-distributed to the kinetic energy of horizontal ($\sqrt{\overline{u'^2}}, \sqrt{\overline{w'^2}}$) motion and the turbulent fluctuations attain a strongly anisotropic character. The thickness of this 'surface layer' is estimated to be on the order of one lateral Taylor microscale (or 1/4 of the local vertical jet half-width in the present jet).

The evolution of the vertical Reynolds shear stress, $\overline{u'w'}$ in the plane $y = 0$ is shown in Figures 4.14d, and 4.15d. The $-\overline{u'w'}$ Reynolds shear stress develops an asymmetry about the centrerline of the jet as the free surfce is approached (Figures 4.14d). For large times ($tU_o/R_o \geq 100$), when the velocity profile becomes monotonically decreased with its maximum at the free surface, the $\overline{u'w'}$ Reynolds stress becomes entirely negative such that turbulence production is always positive. Similat trends can also be observed in the experimental measurements (Figure 4.15d). The profile of the $\overline{u'v'}$ Reynolds stress in the horizontal plane $z = 0$ is shown in Figure 4.16d at tU_o/R_o =100 and compared to experimental data. These profiles are not too different from those in a free jet. The sign of $\overline{u'v'}$ is always such that its contribution to the turbulence production ($\overline{u'v'}\partial U/\partial y$) is always positive. Figures 4.17 and 4.18 show the distributions of the turbulence intensities and the Reynolds shear stress in the intermediate jet (H/D =1.5) at tU_o/R_o = 100, compared with experimental measurements of Anthony and Willmarth (1992), and Walker *et al.* (1994) in spatially growing free-surface turbulent jets. The results are qualitatively similar to those for the shallow jet (H/D =1.0). Good agreement with experimental measurement is also observed here.

4.2.3 Turbulent Kinetic Energy Dissipation and Production

The distribution of the average turbulent kinetic energy dissipation, the average turbulence production and the average turbulent kinetic energy in the (H/D =1.0) jet at tU_o/R_o = 150 are shown in Figures 4.19-4.21. The two-dimensional contour plot of average dissipation at tU_o/R_o = 150 in figure 4.19 shows that the maximum dissipation occurs close to the edges of the jet in a region at a depth of $\approx 0.5Z_{1/2}$. Not surprisingly, the maximum production also occurs approximately in the same regions as shown in figure 4.20. These regions correspond to the location of maximum strain.

Figure 4.21 shows the contour plot of turbulent kinetic energy at tU_o/R_o = 150 for the shallow jet(H/D=1.0). The location of the peak is not at the free surface but slightly below it. The peaks agree well with the location of peak production and dissipation.

4.3 Kinetic Energy and Dissipation Spectra

The conversion of the vertical kinetic energy of turbulence into the kinetic energy of horizontal motion within the 'surface layer' of the jet leads to the establishment of a strongly anisotropic, nearly two-dimensional turbulent state within this layer. To gain a better understanding of the dynamics of turbulence within this layer, we next examine the spectra of kinetic energy and kinetic energy dissipation in the jet.

4.3.1 Deep jet

Figures 4.22 and 4.23 show the three-dimensional kinetic energy and dissipation spectra in the deep jet (H/D =2.0) at tU_o/R_o = 150. These spectra were computed by interpolating the data onto a uniform Fourier grid using spectral interpolation

and calculating the spectra using the definition

$$E(k) = \frac{4\pi k^2}{N} \sum_{k-\frac{1}{2}<|\mathbf{k}|\leq k+\frac{1}{2}} \frac{1}{2}|\hat{\mathbf{u}}'(\mathbf{k})|^2 \tag{4.3}$$

where $\hat{\mathbf{u}}'(\mathbf{k})$ are the Fourier coefficients of the disturbance velocity fluctuation field in the three-dimensional Fourier box, and N is the number of wave vectors k which fall into a spherical shell of radius k. The three-dimensional kinetic energy spectrum shown in figure 4.22 displays a short inertial subrange with a Kolmogorov constant $C_K = 1.4$ which is in good agreement with the value of $C_K \approx 1.5$ suggested by Monin and Yaglom (1981, pp. 485) based on analysis of numerous experimental data. The normalized kinetic energy dissipation spectrum in the jet is shown in figure 4.23. The dissipation spectrum displays a peak at $k_d < \eta > \approx 0.2$, where η is the Kolmogorov scale, suggesting the presence of a dominant length scale for the dissipative structures on the order of $l_d \approx 5 < \eta >$ (or $\approx 0.2\lambda_g$). The value of $k_d < \eta > \approx 0.2$ at which the peak of the dissipation spectrum is observed in the present database is in good agreement with results observed in other numerical simulations of turbulence (Domaradzki 1992) and the wavenumber of peak dissipation predicted by Pao's (1965) spectrum with a Kolmogorov constant of 1.4.

4.3.2 Shallow Jet

Figure 4.24 shows the one-dimensional spectra of the turbulent velocity fluctuations in the jet at $tU_o/R_o = 100$ at various depths below the free surface. At large depths ($z/R_o \geq 2.0$) the turbulence is seen to have an isotropic character, manifested in Figure 4.24 by a collapse of the curves of one-dimensional spectra for the three components of velocity. As the free surface is approached, the low wavenumber components of the vertical velocity fluctuation is suppressed and the kinetic energy of these fluctuations is transferred into the horizontal (particularly streamwise)

components of velocity. This anisotropy in the velocity fluctuations extends into progressively smaller scales, well into the inertial and dissipative ranges of turbulence, as the free surface is approached.

The behavior observed in Figure 4.24 is qualitatively consistent with that predicted by Hunt's (1984) theory, in which the free surface is assumed to affect a turbulent eddy of size ℓ only when the eddy is within a distance ℓ of the free surface. The primary effect of the free surface being the creation of an image eddy which suppresses the vertical velocity fluctuations at the surface and inhibits further movement of the original eddy towards the free surface. Thus the effect of the free surface is expected to be first felt at the lowest wavenumber components of the velocity and to then gradually extend to the high wavenumbers, consistent with the form of the spectra in the jet. Nevertheless, the results shown in Figure 4.24 also reveal important dynamical effects which are not properly accounted for in Hunt's theory. Figure 4.24 shows the anisotropy in the velocity fluctuations to extend to the smallest wavenumbers at the free surface. Furthermore, these results indicate the presence of two distinct subranges in the energy spectra; a $k^{-5/3}$ subrange at intermediate wavenumbers and a k^{-3} subrange at high wavenumbers. These two subranges are typical of 'two-dimensional' turbulence and suggest that the dynamics of turbulence in the 'surface layer' may indeed follow the governing laws of two-dimensional turbulence. Examination of the 3d spectrum (Figure 4.25) shows the presence of the same two sub-ranges. Similar trends can also be observed in the experimental measurements of the energy spectra in planar free surface turbulent jets by Swean *et al.* (1991) and in the free surface grid-stirred tank of Brumley and Jirka (1987).

4.4 Surface Elevation Spectra

The effect of the underlying turbulence on the surface elevation can be studied by examining the surface elevation one-dimensional spectrum shown in Figure 4.26. E_s was computed according to

$$E_s(k) = \sum_{k-\frac{1}{2}<k_x\leq k+\frac{1}{2}} \frac{1}{2}|\hat{h}(\mathrm{k})|^2 \tag{4.4}$$

where $\hat{h}$ is the Fourier transform of the surface elevation. A k^{-3} range can also be observed in the surface elevation spectrum, indicating that at low Froude numbers the surface elevation is mostly determined by the energy of the sub-surface turbulence.

The relationship among vortical sub-surface structures and surface signatures has been investigated by various authors (Bernal and Kwong, 1989; Bernal *et al.*,1989; Sarpkaya and Suthon, 1991, Tryggvason *et al.*, 1991, Madnia and Bernal, 1994). Their interrelation will be discussed further in the analysis of the structure of the small scales (§5), and in the dynamics of the free-suraface turbulence (§6).

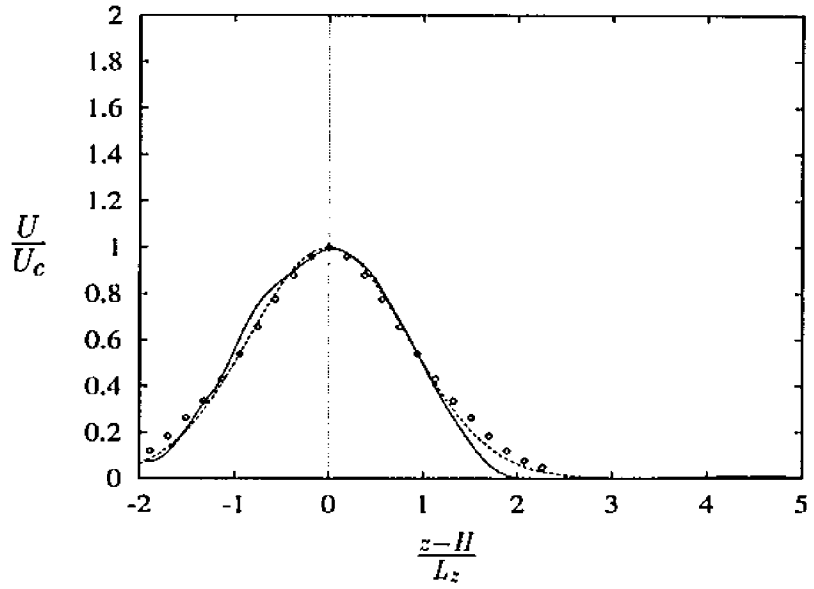

Figure 4.1: Profile of the mean velocity in the plane y=0. —— numerical results at time $tU_o/R_o = 100$, for the deep jet (H/D =2);– – – Gaussian curve (eq. 4.1); ◇ experimental data of Wygnanski and Fiedler (1969) for a free jet.

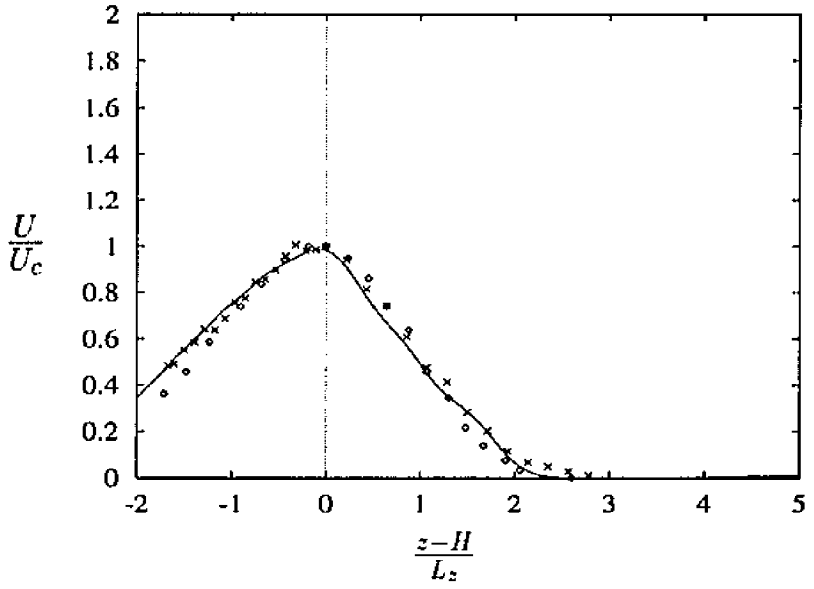

Figure 4.2: Profile of the mean velocity in the plane y=0. ——, numerical results at time $tU_o/R_o = 150$, for the deep jet (H/D =2); ◇, experimental data of Anthony and Willmarth (1992), at x/D=16; ×, experimental data of Walker *et al.* (1994), at x/D=16;

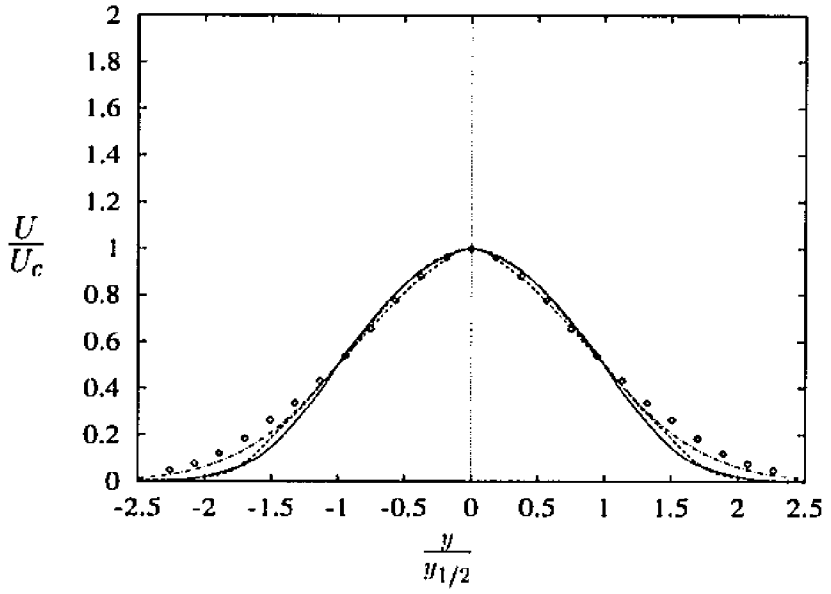

Figure 4.3: Profile of the mean velocity in the plane $z = z_m$ for the deep jet(H/D =2.0); ——, numerical results at time $tU_o/R_o = 100$, – – –, $tU_o/R_o = 150$, – · –·, Gaussian curve (eq. 4.1), ◇ experimental data of Wygnansky and Fiedler (1969), for a free jet.

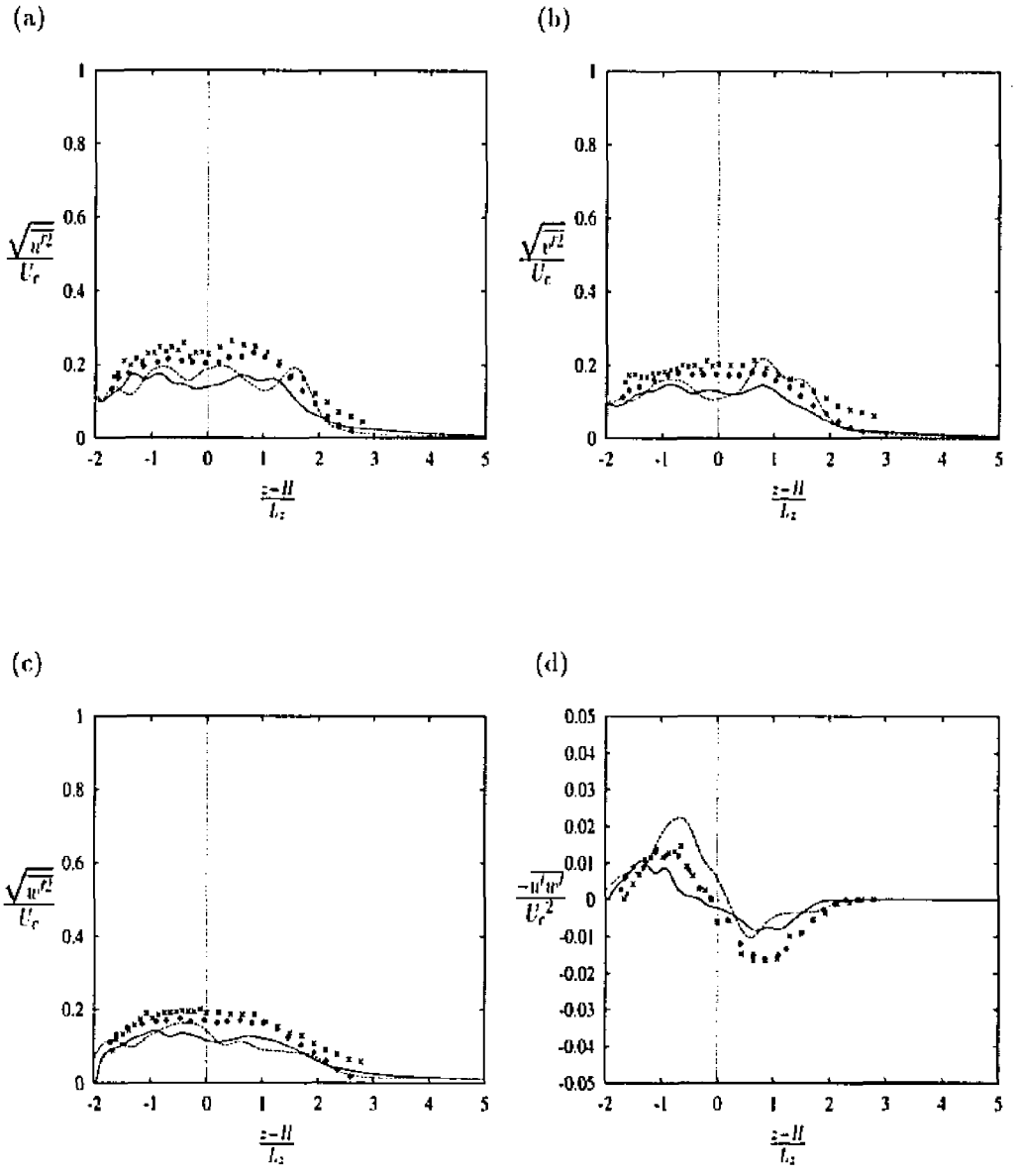

Figure 4.4: Profile of the turbulent intensities and Reynolds stress in the plane y=0. —, numerical results at time $tU_o/R_o = 100$; – – –, $tU_o/R_o = 150$, for the deep jet (H/D =2.0); ◇, experimental data of Anthony and Willmarth (1992), at x/D=16; ×, experimental data of Walker *et al.* (1994), at x/D=16;

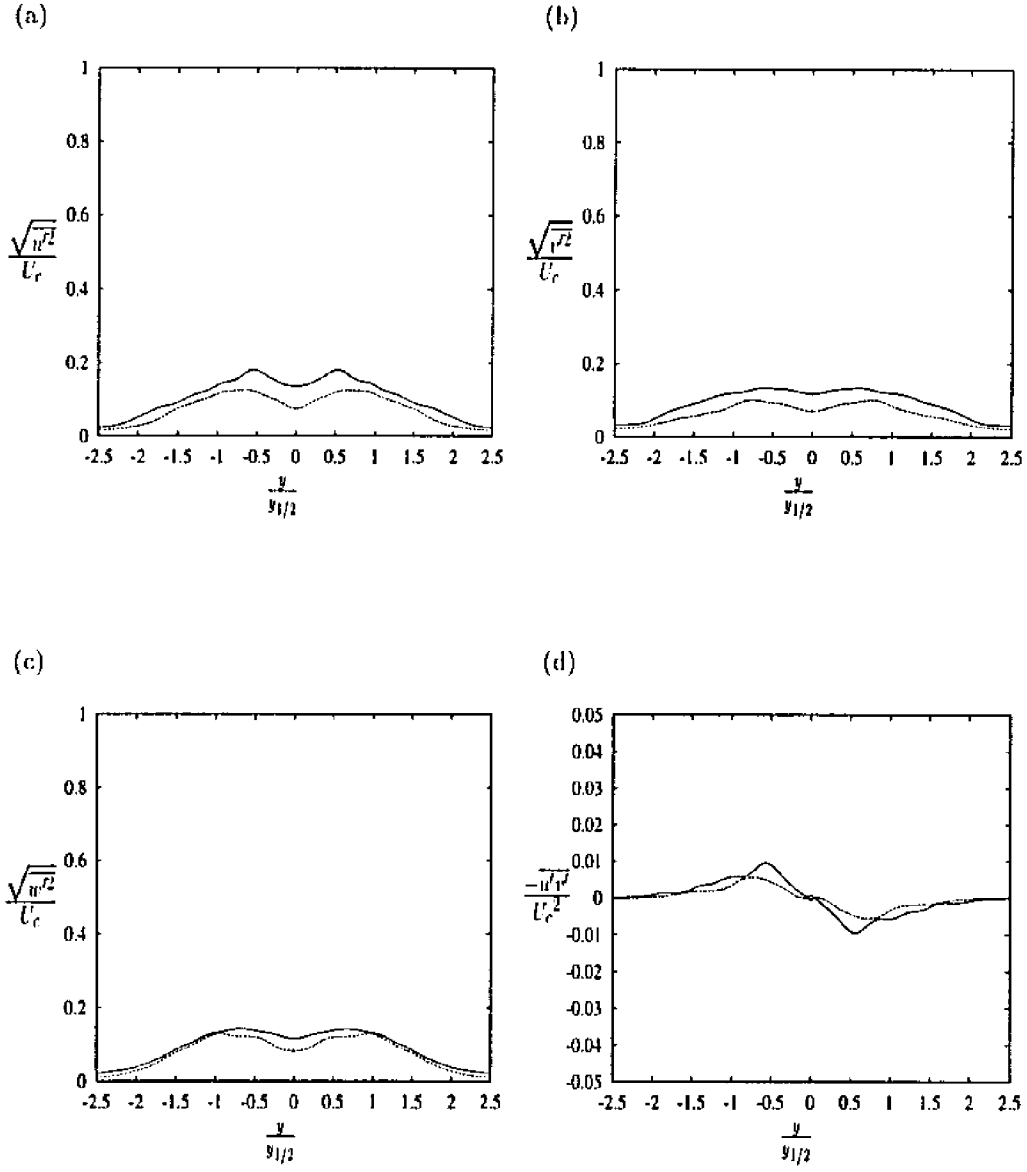

Figure 4.5: Profile of the turbulent intensities and Reynolds stress in the plane $z = z_m$. ——, numerical results at time $tU_o/R_o = 100$, – – –, $tU_o/R_o = 150$; for the deep jet (H/D =2.0).

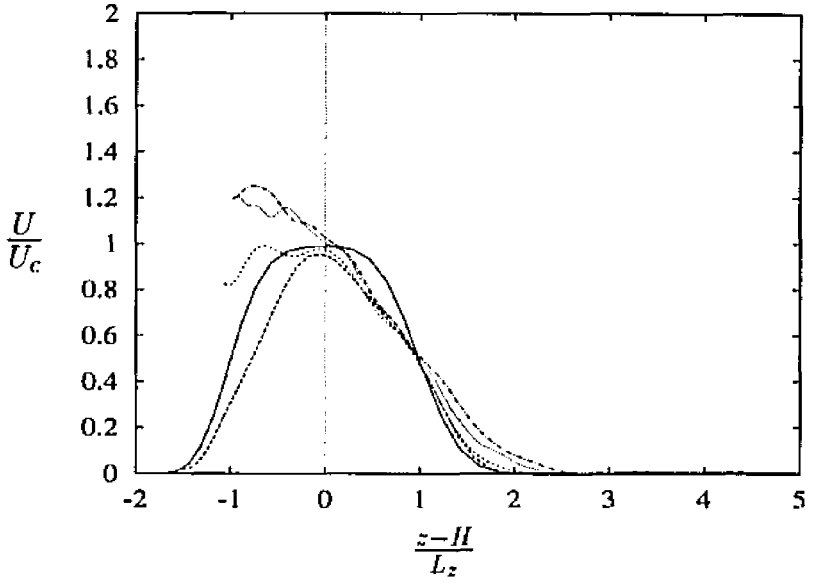

Figure 4.6: Time evolution of the profile of the mean velocity in the plane y=0, for the shallow jet (H/D =1.0). —, numerical result at time $tU_o/R_o = 0$, – – –, $tU_o/R_o = 25$; - - - - -, $tU_o/R_o = 50$; · · · · ·, $tU_o/R_o = 75$; – · – · –, $tU_o/R_o = 100$.

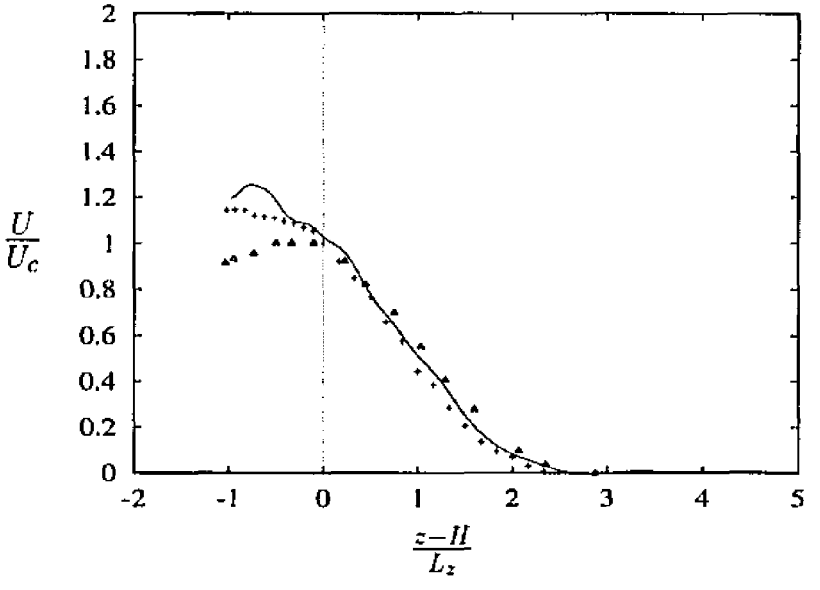

Figure 4.7: Profile of the mean velocity in the plane y=0. —, numerical results at time $tU_o/R_o = 100$ for the shallow jet (H/D =1.0); △, experimental data of Anthony and Willmarth (1992) at x/D=32; +, experimental data of Walker *et al.* (1994) at x/D=32;

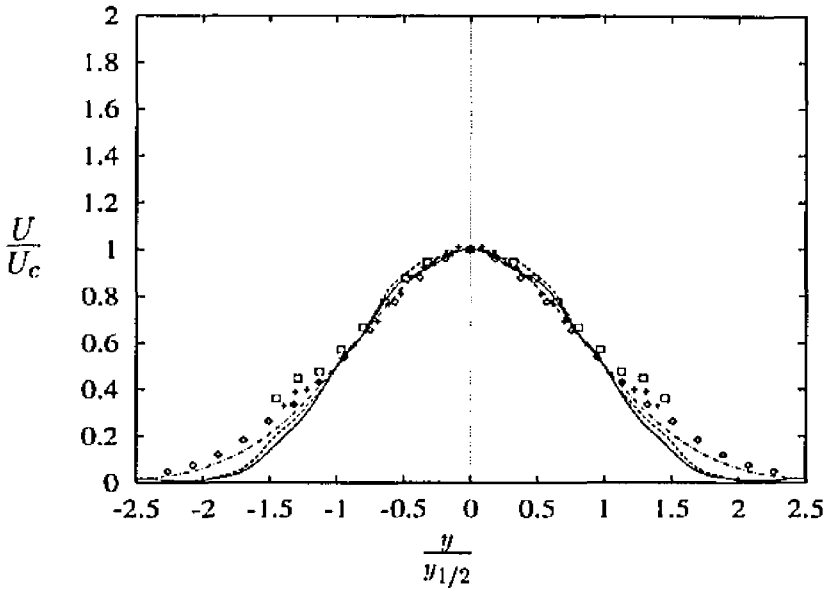

Figure 4.8: Profile of the mean velocity at time $tU_o/R_o = 100$. for the shallow jet (H/D =1.0); — at the plane $z = z_m$, − − − at the free surface, −·−·− Gaussian curve(eq 4.1), + experimental data of Walker *et al.* (1994), at x/D=32, □ experimental data of Anthony and Willmarth (1992), at x/D=32, ◇, experimental data of Wygnanski and Fiedler(1969).

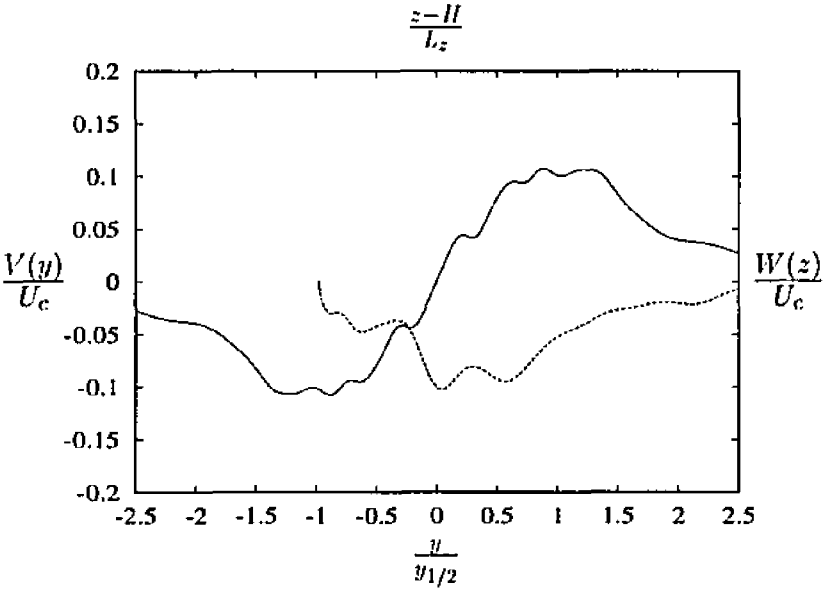

Figure 4.9: Profiles of the mean velocities in the horizontal and vertical directions at time $tU_o/R_o = 100$ for the shallow jet (H/D =1.0); — horizontal profile V(y) along plane $z = 0$, − − − vertical profile W(z), along plane $y = 0$.

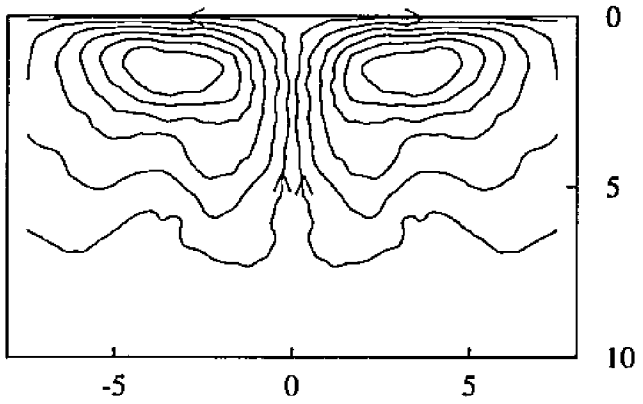

Figure 4.10: Streamlines of the mean secondary flow at time $tU_o/R_o = 100$, for the shallow jet (H/D =1). The streamlines are from $\psi/(U_oR_o)$ =-0.0152 to 0.0152, with an increment of 2.78×10^{-3}.

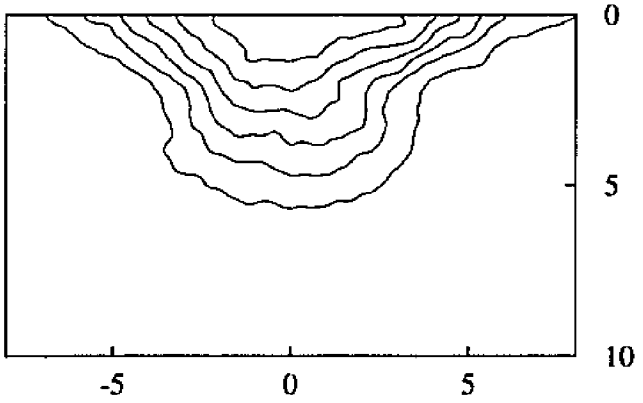

Figure 4.11: Contours of constant mean streamwise velocity ($\overline{U}$) at time tU_o/R_o = 100 for the shallow jet (H/D =1). The contours are from U/U_o) =0.0145 to 0.132, with an increment of 2.3×10^{-2}.

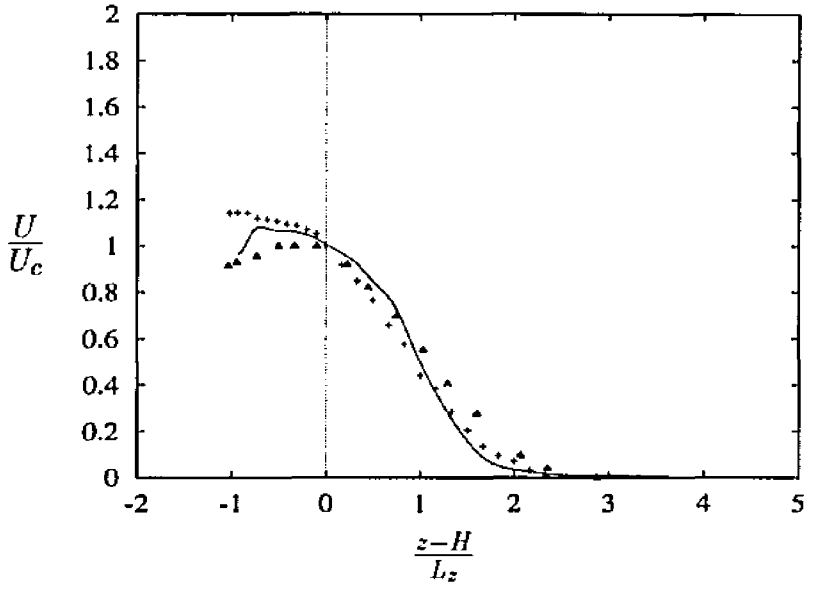

Figure 4.12: Profile of the mean velocity in the plane y=0. —, numerical results at time $tU_o/R_o = 100$, for the intermediate jet (H/D =1.5); △, experimental data of Anthony and Willmarth (1992), at x/D=32; +, experimental data of Walker *et al.* (1994), at x/D=32;

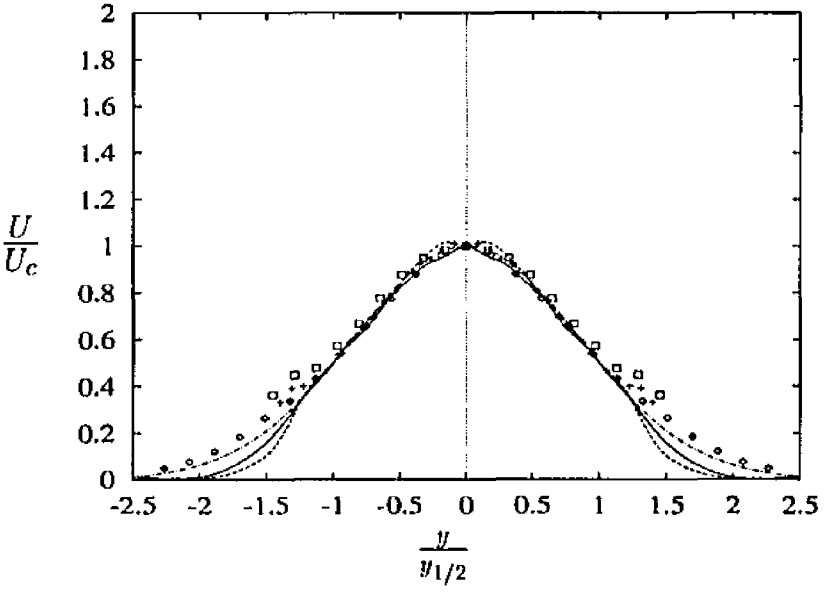

Figure 4.13: Profile of the mean velocity at time $tU_o/R_o = 100$. for the shallow jet (H/D =1.5); — at the plane $z = z_m$, − − − at the free surface, −·−·− Gaussian curve(eq 4.1), + experimental data of Walker *et al.* (1994), at x/D=32, □ experimental data of Anthony and Willmarth (1992), at x/D=32, ◇, experimental data of Wygnanski and Fiedler(1969).

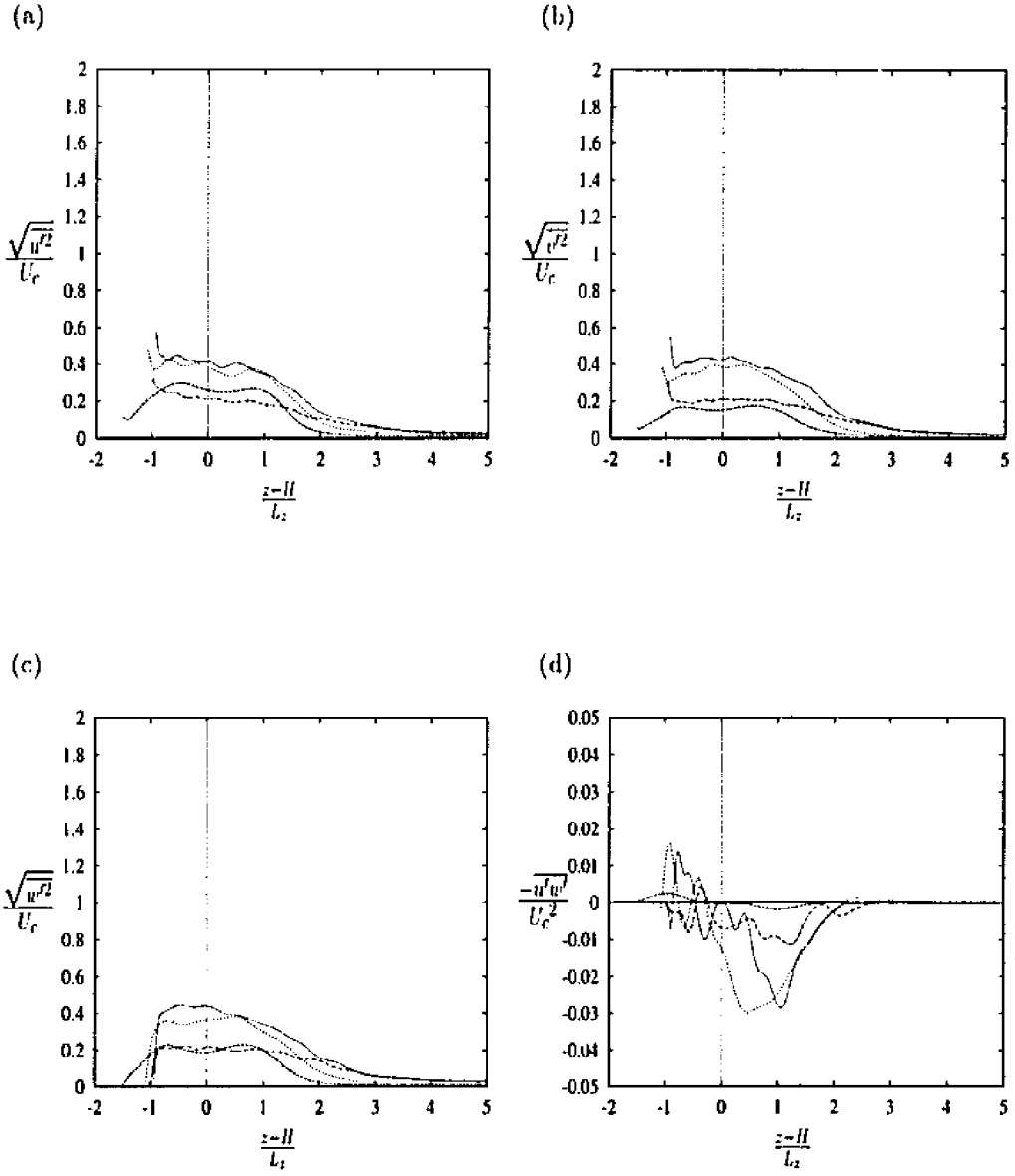

Figure 4.14: Evolution of the profiles of turbulent intensities and Reynolds stress in the plane y=0, for the shallow jet (H/D =1.0); ——, numerical results at time $tU_o/R_o = 0$, − − −, $tU_o/R_o = 25$; - - - - -, $tU_o/R_o = 50$; · · ·, $tU_o/R_o = 75$; − · − · −, $tU_o/R_o = 100$.

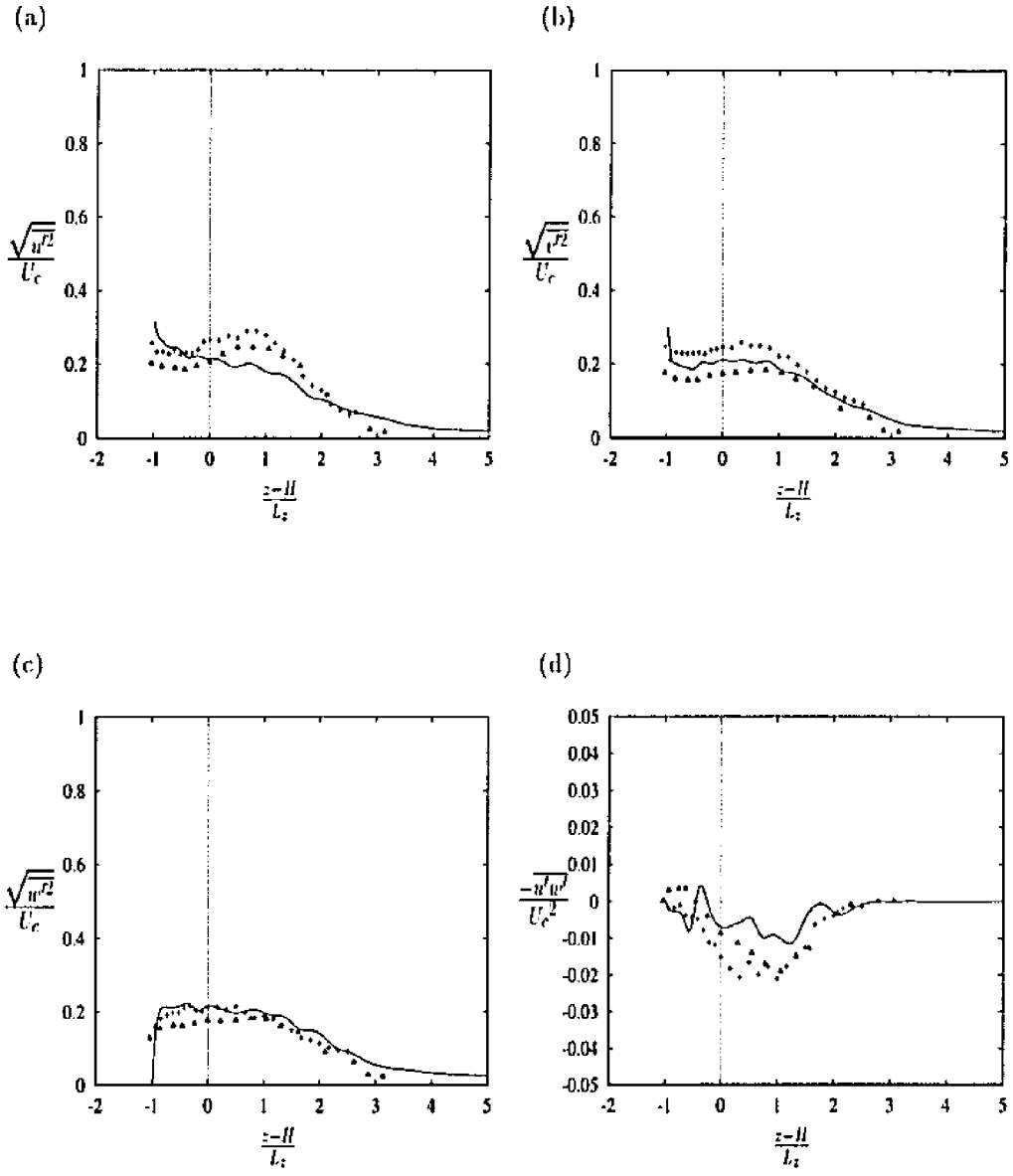

Figure 4.15: Profile of the turbulent intensities and Reynolds stress in the plane y=0. ——, numerical results at time $tU_o/R_o = 100$, for the shallow jet (H/D =1.0); △, experimental data of Anthony and Willmarth (1992), at x/D=32; +, experimental data of Walker *et al.* (1994), at x/D=32;

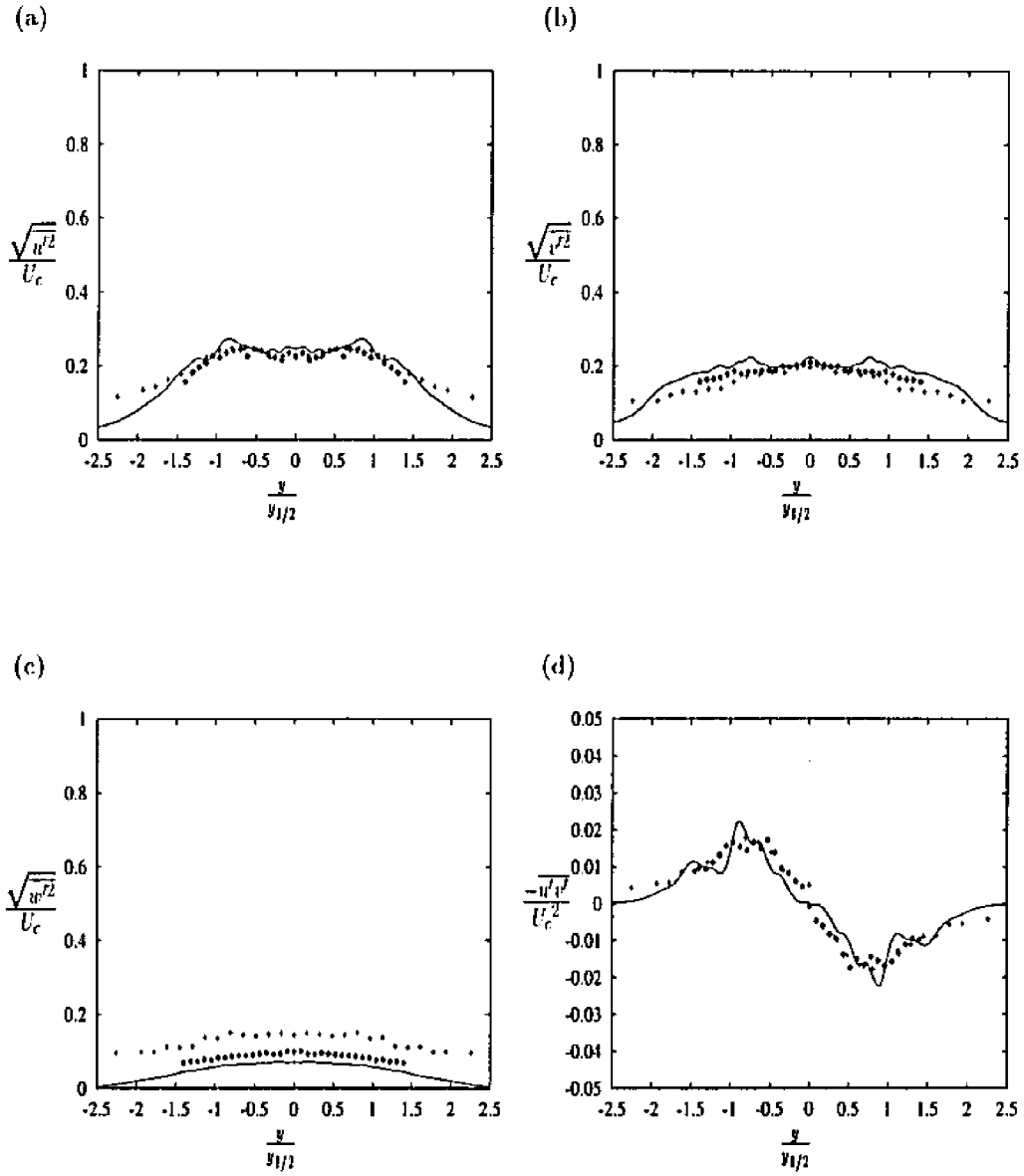

Figure 4.16: Profile of the turbulent intensities and Reynolds stress in the plane $z = 0$. ——, numerical results at time $tU_o/R_o = 100$, shallow jet (H/D =1.0); ◇, experimental data of Walker *et al.* (1994), at x/D=32. +, experimental data of Anthony and Willmarth (1992), at x/D=32.

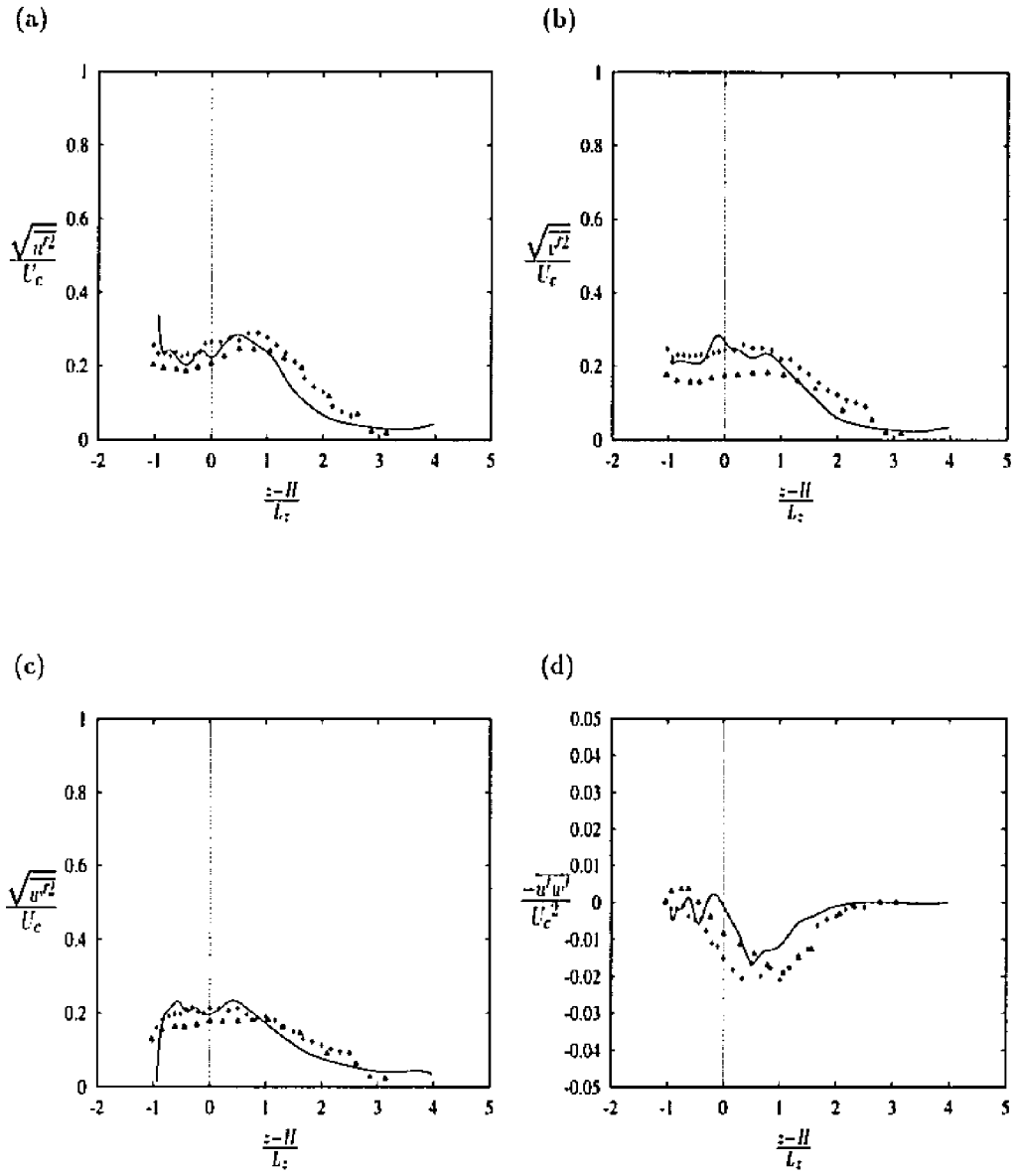

Figure 4.17: Profile of the turbulent intensities and Reynolds stress in the plane y=0. —, numerical results at time $tU_o/R_o = 100$, for the intermediate jet (H/D =1.5); △, experimental data of Anthony and Willmarth (1992), at x/D=32; +, experimental data of Walker *et al.* (1994), at x/D=32;

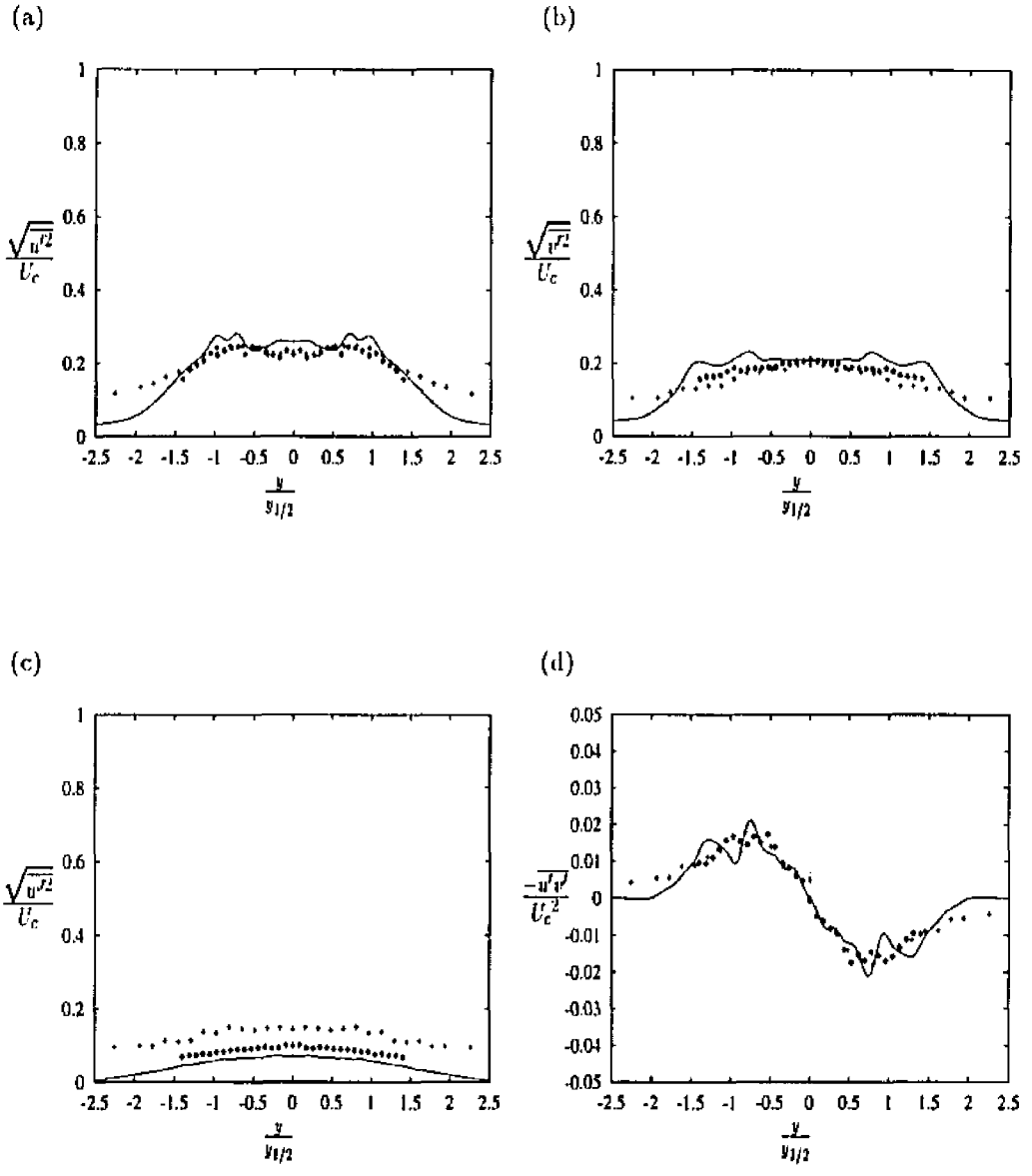

Figure 4.18: Profile of the turbulent intensities and Reynolds stress in the plane $z = 0$. ——, numerical results at time $tU_o/R_o = 100$, shallow jet (H/D =1.5); ◇, experimental data of Walker *et al.* (1994), at x/D=32, + experimental data of Anthony and Willmarth (1992), at x/D=32;

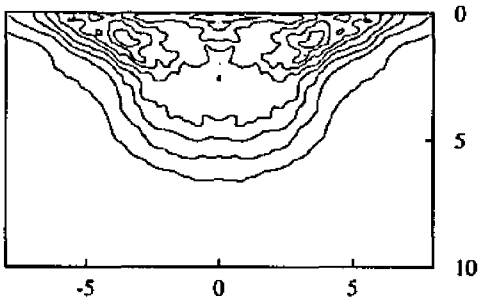

Figure 4.19: Contour plots of average kinetic energy dissipation ϵ at time $tU_o/R_o = 150$ for the shallow jet (H/D =1). The contours are from $\epsilon R_o/U_o^3 = 1.0 \times 10^{-6}$ to 81.0×10^{-6}, with an increment of 1.0×10^{-6}.

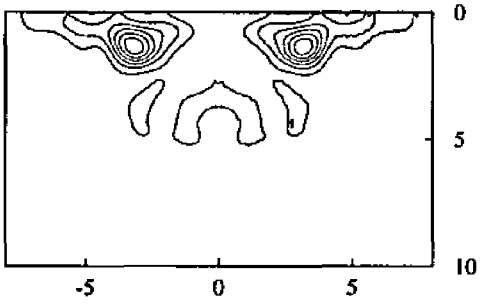

Figure 4.20: Contour plots of average turbulence production p at time $tU_o/R_o = 150$ for the shallow jet (H/D =1). The contours are from $pR_o/U_o^3 = 1.05 \times 10^{-6}$ to 9.55×10^{-7}, with an increment of 1.92×10^{-6}.

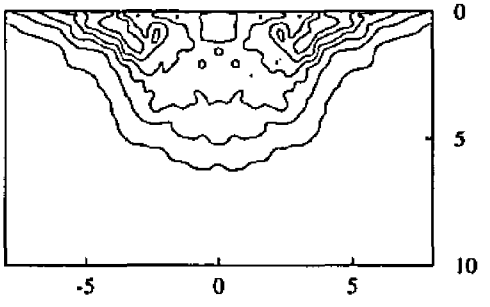

Figure 4.21: Contour plots of average turbulent kinetic energy q^2 at time $tU_o/R_o = 150$ for the shallow jet (H/D =1). The contours are from $q^2/U_o^2 = 9.39 \times 10^{-5}$ to 5.63×10^{-4}, with an increment of 9.4×10^{-5}.

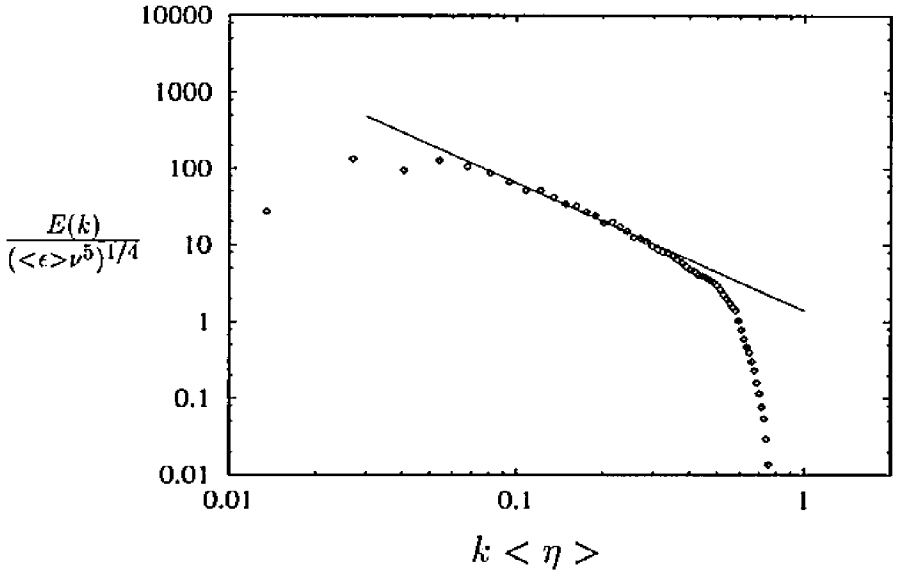

Figure 4.22: Three-dimensional spectrum of kinetic energy in the deep jet H/D =2.0 at $tU_o/R_o = 150$. $\diamond$ numerical results, — 1.4 $k^{-5/3}$ slope line.

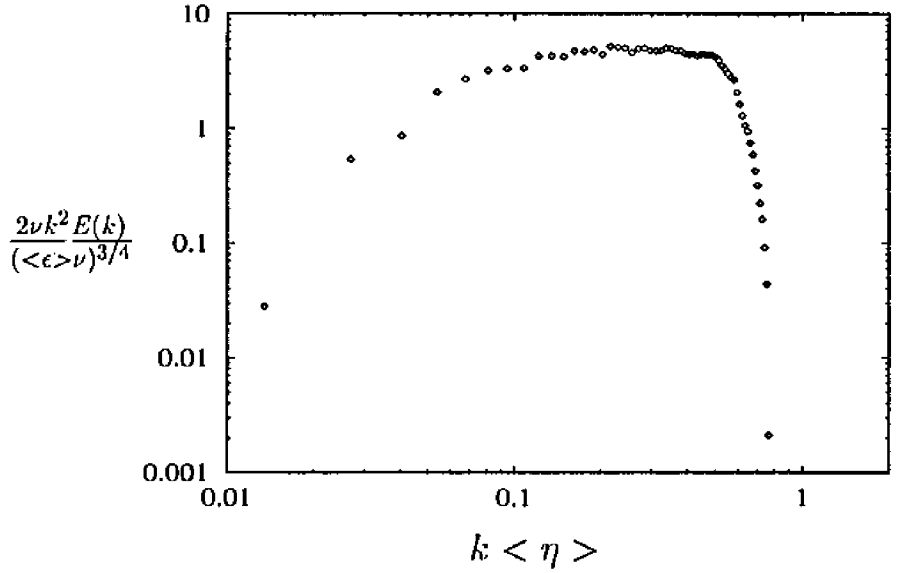

Figure 4.23: Three-dimensional spectrum of kinetic energy dissipation in the deep jet H/D =2.0 at $tU_o/R_o = 150$.

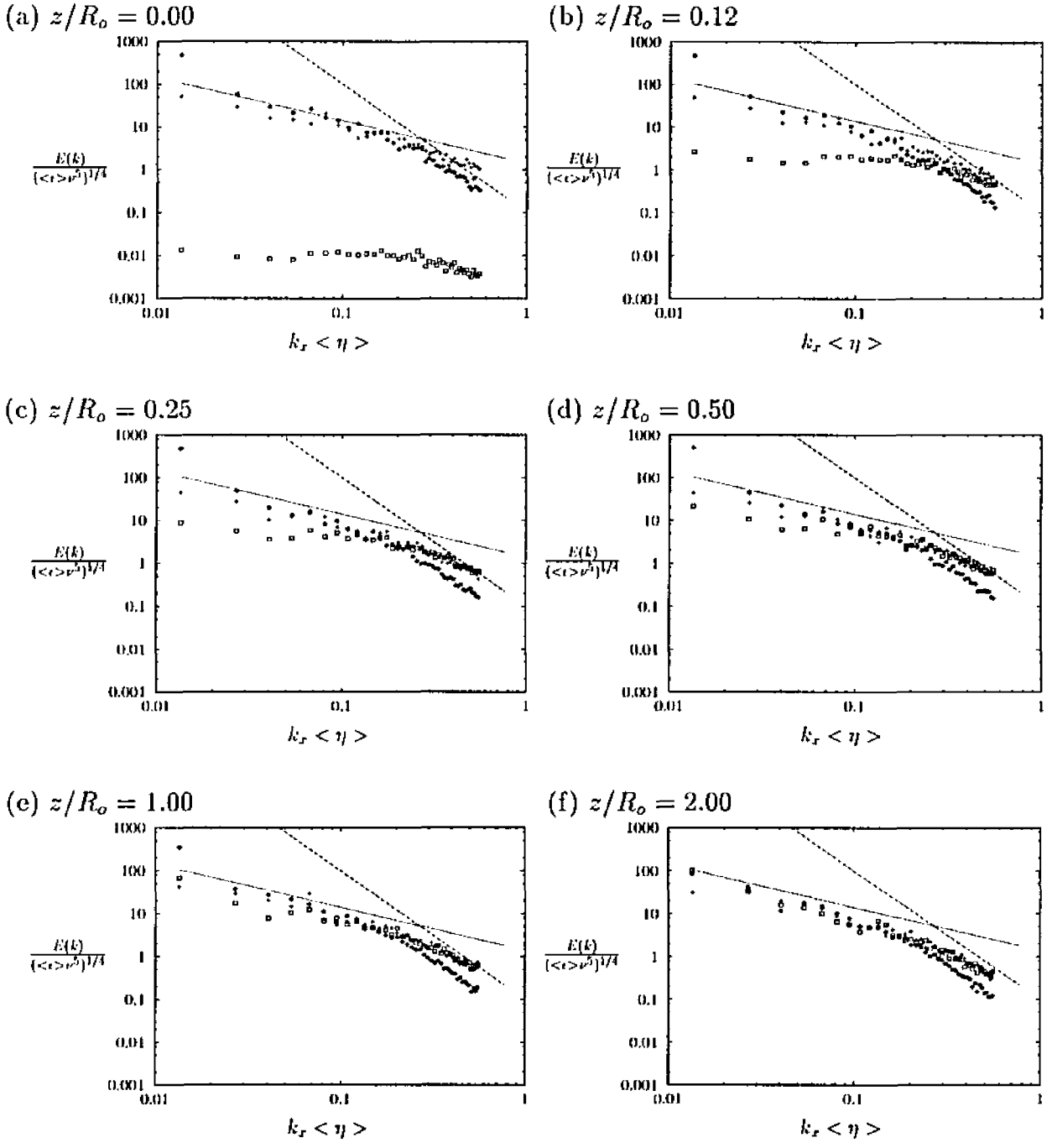

Figure 4.24: One-dimensional spectrum of kinetic energy in the shallow jet, $H/D = 1.0$ at time $tU_o/R_o = 150$, at various depths. $\diamond$, u; $+$, v; $\square$, w; ——$k^{-5/3}$ slope line, – – –k^{-3} slope line.

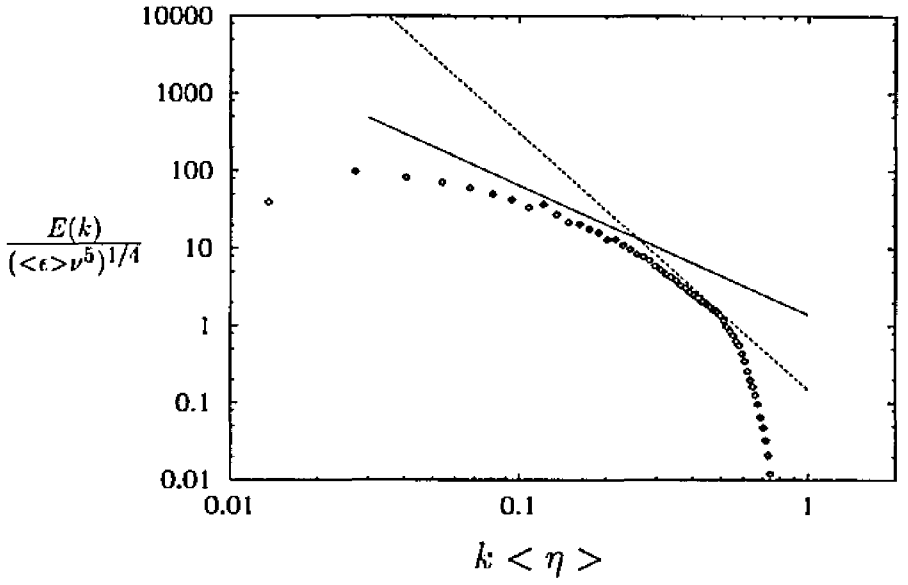

Figure 4.25: Three-dimensional spectrum of kinetic energy in the shallow jet H/D =1.0 at $tU_o/R_o = 150$. $\diamond$ numerical results; ——, 1.4 $k^{-5/3}$ slope line, – – –, .15k^{-3} slope line.

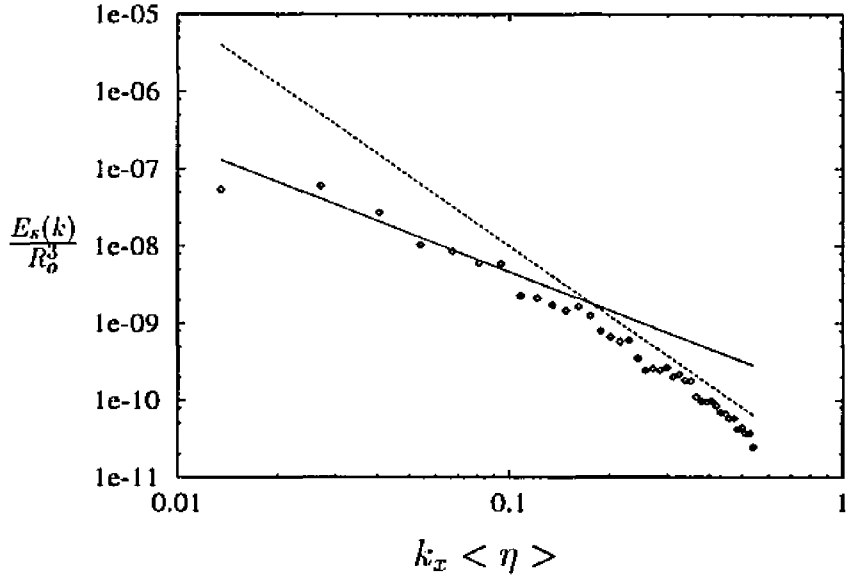

Figure 4.26: One-dimesional spectrum of surface elevation in the jet surface. $\diamond$ numerical results at time $tU_o/R_o = 150$; —— $k^{-5/3}$ slope line; – – – k^{-3} slope line.

CHAPTER V

TURBULENCE STRUCTURE

In this chapter, the structure of turbulence in the free-surface jet is examined and free-surface effects are discussed. An understanding of the dynamics of these structures will help identify the physical-space mechanisms responsible for the transfer of energy between scales of turbulent motion, and the role played by the free surface in the overall dynamics of turbulence.

The structure of turbulence will be first examined in the deep jet (H/D =2.0), where the jet is just beginning to interact with the free suraface, and free surface effects are still small. The discussion will then turn to the shallow jets, for which free surface effects are strong.

5.1 Large Scale Structure of the Jet

The existence of organized large-scale structures in jets has been verified experimentally in a number of works. Yule (1978) investigated the vortices in the transition region and the large eddies in the turbulent region of a jet, by using flow-visualization and hot-wire techniques. Using a conditional sampling technique, eddies moving near the center-line were measured. The sampled eddies were found to contribute greatly to local velocity fluctuations and statistical correlations. Yoda *et al.* (1992) investi-

gated the structure and evolution of natural and forced turbulent round jets in the far field and found both helical and axisymmetric instability modes to be present in the natural jet. Schefer *et al.* (1994) studied the existence of organized large-scale structure in jets using planar imaging of the CH_4 concentration in a turbulent jet. They observed a non-symmetric behavior, with vortical structures appearing on one side or the other, but not necessarily both sides. They also observed instantaneous concentration fields which were consistent with the axisymmetric instability mode. Overall this jet showed clear evidence of the axisymmetric instability mode on 40% of the images analyzed, while 30% showed evidence of the helical instability, and 30% showed no clear evidence for either instability mode. Another important feature was the observation of ramp-like structures, associated with vortical structure formation during the axisymmetric instability mode. The sudden increase in concentration in the ramp corresponds to the leading edge of the vortical structures, while the subsequent gradual decrease is associated with the remainder of the structure.

In these experiments the large scale vortical structure is derived either by some conditional sampling or by observation of the spreading of a passive scalar. In this work, since the complete velocity field is available, the vorticity distribution can be computed directly. However, the vorticity field emphasizes the small scale features of the flow. In order to analyze the large-scale vortical structures, it is necessary to apply a filtering operation that emphasizes the large scale contributions. The simplest such approach is to apply a sharp low-pass Fourier cut-off filter at various wavenumbers. The resulting vorticity (or vorticity magnitude) field is representative of the fluid motion at the scales close to the cut-off.

5.1.1 The Deep Jet

Figure 5.1 shows the large scale vortical structure of the deep jet at t =200, for two sharp cut-off filter at $k_c < \eta >$=0.070, and 0.025. The energy above these cut-offs corresponds to about 40% and 25% of the total turbulent kinetic energy, respectively. The shape of the isosurface of vorticity magnitude suggests the predominance of the antisymmetric instability mode, but there are indications of the presence of the symmetric mode as well. This is consistent with the experimental observation that the jet switches between the axisymmetrical and helical modes and is in each mode about 50% of the time.

At the largest scales (scales representative of the size of energy-containing eddies) the vorticity field consists of hybrid structures, that combine features of both axisymmetric and helical modes. These eddies give rise to a predominantly 'flapping' type of motion, although at certain locations they appear symmetrically aligned about the jet center-line and locally give rise to a 'puffing' type of motion. Increasing the magnitude of the cutoff wavenumber to a size representative of the smaller energy-containing eddies (figure 5.1b) reveals the presence of coherent vortical structures which are formed by the cut and reconnect of the primary eddies shown in figure 5.1a. The predominant structures at this cutoff continue to be helix-like, or deformed ring eddies whose axis lies in the $x - y$ plane. These eddies are consistent with one class of organized structures which have been described in experimental studies of spatially growing turbulent jets (Mumford 1982, Thomas & Goldschmidt 1986). A second class of structures suggested in experimental studies (Mumford 1982) consists of roller-like eddies whose axes are aligned along the direction of the mean flow strain field. While such 'strainwise' eddies were found to be rare at the scale of energy-containing eddies, at the smaller scales (on the order of inertial range and

dissipative scales) the organized vortical structures in the flow consisted primarily of such elongated vortex tubes with axes oriented along the direction of the mean flow strain field.

5.1.2 The Shallow Jet

Figure 5.2 shows the large scale vortical structure of the shallow jet at t =200, for the same sharp cut-off filters at $k_c < \eta >$=0.070 and 0.025. As the jet reaches the free surface, the presence of the surface precludes the existence of the initial axisymmetric mode. The helix and ring shaped eddies become further deformed, giving origin to elongated eddies almost parallel to the surface, and there are indications of the reconnection of the large scale eddies with the surface, leading to large scale vortical structures normal to the surface. The overall appearance of the free-surface large scale eddies is of a helix cut in half by the surface. There are also indications of the formation of half-ring shaped eddies, which are attached to the surface, but are not necessarily aligned with the center of the jet, being therefore a combination of axisymmetric and helical instability modes.

5.2 Two-Point Correlations

The two-point correlations of the three components of the disturbance velocity with separations along the streamwise (x), and lateral (y) directions are shown in figures 5.3 and 5.4 for the deep (H/D =2.0) jet at $tU_o/R_o = 200$. In the streamwise direction, the two-point correlations were computed on the center-line of the jet according to the definition

$$R_{ii}(\mathbf{r}) = \frac{\overline{u_i'(\mathbf{x})u_i'(\mathbf{x}+\mathbf{r})}}{\overline{[u_i'^2(\mathbf{x})]^{1/2}}\ \overline{[u_i'^2(\mathbf{x})]^{1/2}}} \tag{5.1}$$

where $\mathbf{x}$ is the position on the center-line and $\mathbf{r}$ is the separation vector. In the lateral direction, (figure 5.4) the two point correlations were measured between points which were symmetrically located on opposite sides of the jet center-line,

$$R_{ii}(\pm\frac{\mathbf{r}}{2}) = \frac{\overline{u_i'(\mathbf{x}-\mathbf{r}/2)u_i'(\mathbf{x}+\mathbf{r}/2)}}{[u_i'^2(\mathbf{x}-\mathbf{r}/2)]^{1/2}\,\overline{[u_i'^2(\mathbf{x}+\mathbf{r}/2)]^{1/2}}} \tag{5.2}$$

This form of the correlation coefficient in the lateral direction has been commonly used in experimental studies of turbulent jets to deduce the large-scale coherent structure of the flow. An example of these measurements for the u component from the data of Wygnanski and Fiedler (1969) is also shown in figure 5.3 and 5.4.

The two-point correlations for the deep jet show good qualitative agreement with experimental data for the velocity components of free jets, for which experimental data is available. In the streamwise direction, these correlations drop off to small values at a separation of one-half the domain length, indicating that the computational domain is adequately large to ensure that the assumption of periodicity does not significantly affect the dynamics of the large scale structures.

5.3 The Fine Scale Structure

5.3.1 The Deep Jet

We begin by examining the spatial distributions of the fluctuating vorticity, the passive scalar, and the kinetic energy dissipation fields for the deep jet (H/D =2). Figure 5.5 shows the distribution of these fields in two perpendicular planar cuts through the jet at $tU_o/R_o = 200$; one (plane $y = 0$) oriented along the streamwise direction, and the other (plane $x = 1.38R_o$) along the transverse direction. All quantities have been normalized with respect to their respective averages (denoted by $< >$) in a box extending from $-4 < y/R_o < 4$ and $0 < z/R_o < 8$, and are plotted using a linear gray-scale color scheme. Figure 5.5 shows the regions of high

intensity vorticity in the jet to be in the form of vortex tubes with a preferential orientation along the direction of the mean flow strain field; i.e., at 45 degrees to the direction of the mean flow lying on conocal surfaces around the centerline of the jet. In the streamwise cut through the jet, the projection of these structures appears elongated and at 45 degrees to the streamwise direction, while in the transverse cut their projection is seen to form a ring around the centerline of the jet.

A similar picture is also observed for the structure of the kinetic energy dissipation fields (Figure 5.5b). The regions of high intensity kinetic energy dissipation are seen to be well correlated with the regions of intense vorticity, occurring at the periphery of the intense vortical structures.

Figure 5.6 shows a three-dimensional view of these structures in the jet. High intensity vortex tubes, oriented at 45 degrees to the direction of the mean flow, can clearly be seen in this picture. These vortex tubes have a diameter on the order of 10 Kolmogorov scales ($0.3\lambda_g$) and a length on the order of an integral scale. The presence of similar tube-like vortical structures with characteristic diameter on the order of the Kolmogorov scale and a length on the order of an integral scale has been observed in a number of databases of homogeneous, isotropic turbulence (Yamamoto & Hosokawa 1988, She et al. 1990, Ruetsch & Maxey 1991, Vincent & Meneguzzi 1991, Jimenez et al 1992), as well as turbulent shear flows (Ansari 1993). These structures give rise to high intensity kinetic energy dissipation at their periphery in rod-like regions of diameter on the order of 10 Kolmogorov scales, similar to a Burger vortex tube. The size of these intense regions of kinetic energy dissipation corresponds to the scale at which the dissipation spectrum reaches its peak, providing a physical explanation for the presence of this peak (Ansari, 1993).

5.3.2 The Shallow Jets

To begin to investigate the effects of the free-surface on the dynamics of turbulence, we next examine the structure of turbulence in the shallow jets.

Figure 5.7 shows the structure of the vorticity, kinetic energy dissipation and passive scalar field in two perpendicular streamwise and transverse cuts through the shallow ($H/D = 1.0$) jet at time $tU_o/R_o = 200$. The transverse cuts of the various fields show dramatic spread in the jet width in the transverse direction as the jet approaches the free suraface. This phenomenon, known as the surface current, has also been observed in a number of experimental studies of free-surface jet (Madnia and Bernal, 1989; Anthony and Willmarth, 1992; Walker *et al.*, 1994).

High intensity regions of vorticity and kinetic energy dissipation are again seen to be well-correlated and to have rod-like structures, with intense kinetic energy dissipation occurring at the periphery of the intense vortical structures.

Figure 5.8 shows a three-dimensional view of the vortical structures in the shallow jet jet at $tU_o/R_o = 200$. Two classes of organized vortical structures can be identified near the free-surface; (i) vortex tubes with axis parallel to the free surface oriented along the direction of the mean flow strain field and, (ii) vortex tubes with axis normal to the free surface connected to the surface. Close-up view of these two classes of structures, together with their respective free-surface signature, is shown in Figure 5.9 and 5.10. Due to the downward motion induced by the images on the free surface the parallel vortex tubes can only get to within a distance on the order of their own diameter of the free surface. The self-induced lateral motion of these structures under the influence of their images leads to a large-scale mean secondary flow (chapter 4) known as the surface current. In effect, the free-surface provides a mechanism that 'sorts' vortical structures parallel to it, causing the clockwise vortices

to move right, and the counter-clockwise vortices to move to the left. This motion is the origin of the significantly higher lateral spreading rates of the jet compared to its spreading rates in the vertical direction. These vortices are subject to 3D dynamics an the usual cascade of energy to the small scale.

The normal vortex tubes, on the other hand, connect to the free surface and form long-lasting structures at the edges of the jet. The origin of these structures is underlying vortex tubes which approach the free surface at an angle and connect to it. These vortices are pumped to the edges of the jet by the mean secondary flow, where they form long lasting whirls. This effect can be seen by looking at the distribution of the average normal vorticity magnitude accross the surface of the jet, shown in Figure 5.11. The normal vorticity magnitude has a plateau at the center of the jet, and peaks at the edges of the jet, where the long lasting whirls dwell. The longevity of these structures is due to the lack of strong vortex stretching in them. The connection of these structures to the free surface constrains their motion, and prevents them from freely changing their orientation to align with the direction of mean flow strain. The only strain that can act on these vortices is due to variation in the normal component of the velocity near tha surface, which is small compared to the mean flow strain. Consequently, the cascade of energy in these vortices is inhibited, leading to the establishment of a nearly two-dimensional turbulent state in the immediate vicinity of the free surface.

The surface signature of the two classes of structures is shown in Figures 5.12. The top view of the surface shows elongated elevations and depressions aligned with the direction of the main flow strain field, i.e., at 45 degrees to the direction of the mean flow, and circular depressions at the edges of the jet. Figure 5.13 shows the same surface rendered semi-transparent showing the underlying vortical structures.

The overall dynamics of turbulence within the 'surface layer' is determined by a balance between the 'two-dimensional' dynamics of the connected vortical structures and the 'three-dimensional' dynamics of the parallel vortex tubes.

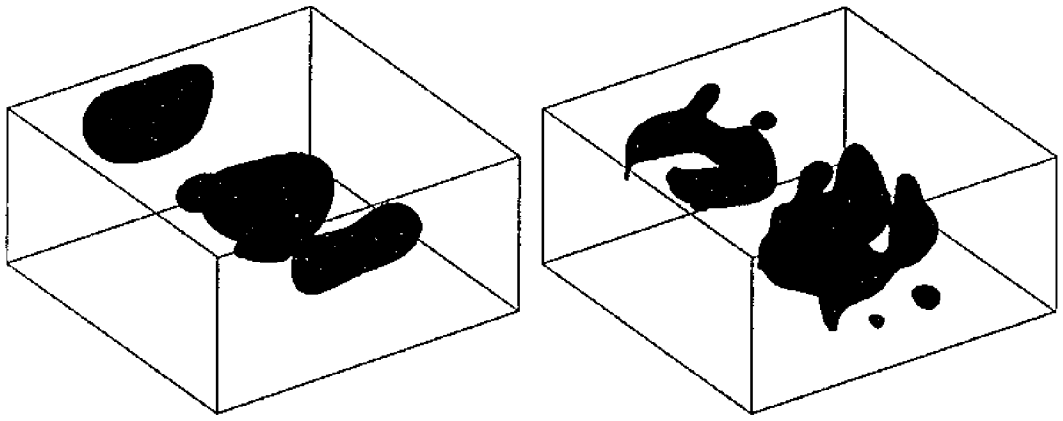

Figure 5.1: Isosurfaces of vorticity magnitude, $|\omega|/|\omega_{max}|$ =0.5, H/D =2.0, at $tU_o/R_o = 200$, for $k_c < \eta >= 0.025$ (left) and 0.070 (right)

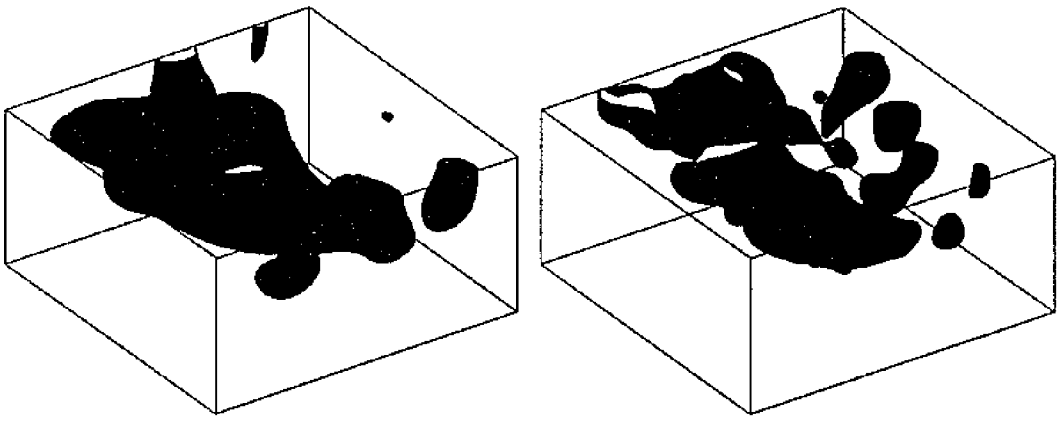

Figure 5.2: Isosurfaces vorticity magnitude, $|\omega|/|\omega_{max}|$ =0.5, H/D =1.0, at $tU_o/R_o = 200$, for $k_c < \eta >= 0.025$ (left) and 0.070 (right)

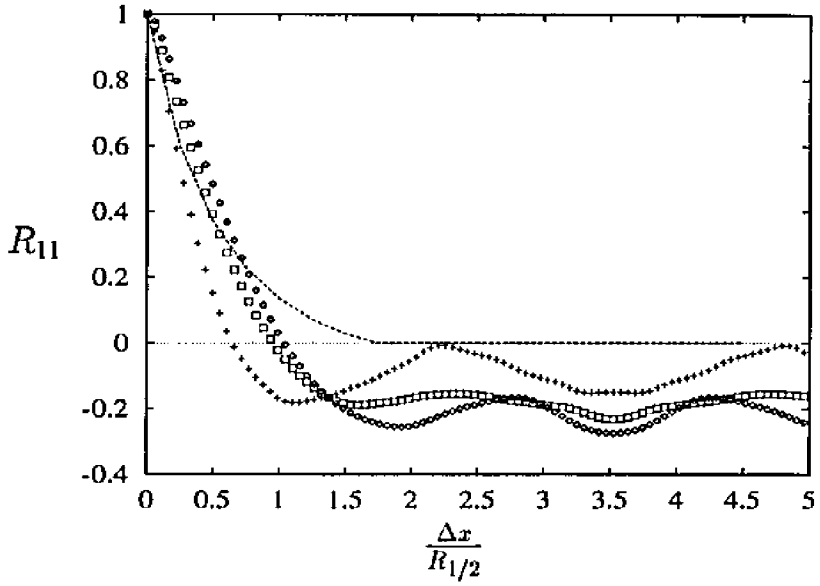

Figure 5.3: Longitudinal correlation on the deep jet(H/D =2.0) at time tU_o/R_o = 200. □, u component; ◇, v component; +, w component; − − −, u component from experimental data of Wygnansky and Fiedler (1969).

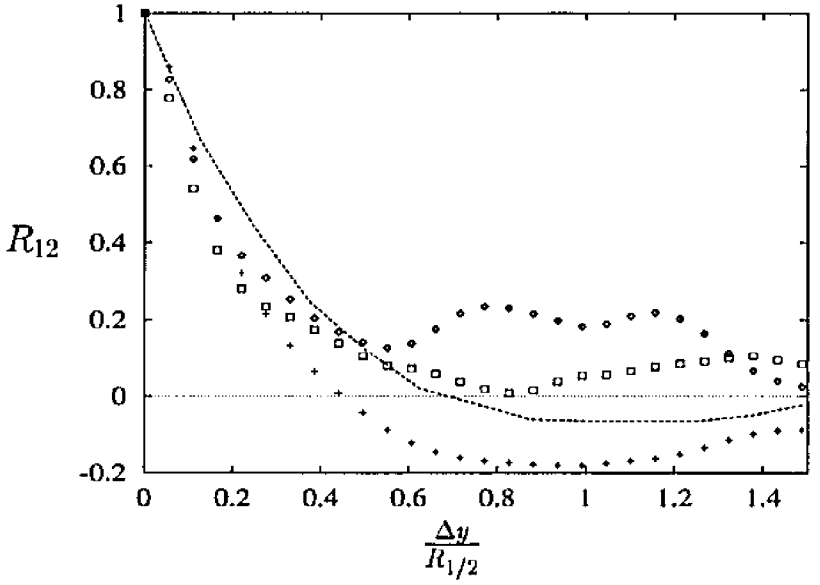

Figure 5.4: Lateral correlation on the deep jet(H/D =2.0) at time $tU_o/R_o = 200$. □, u component; ◇, v component; +, w component; − − −, u component from experimental data of Wygnansky and Fiedler (1969).

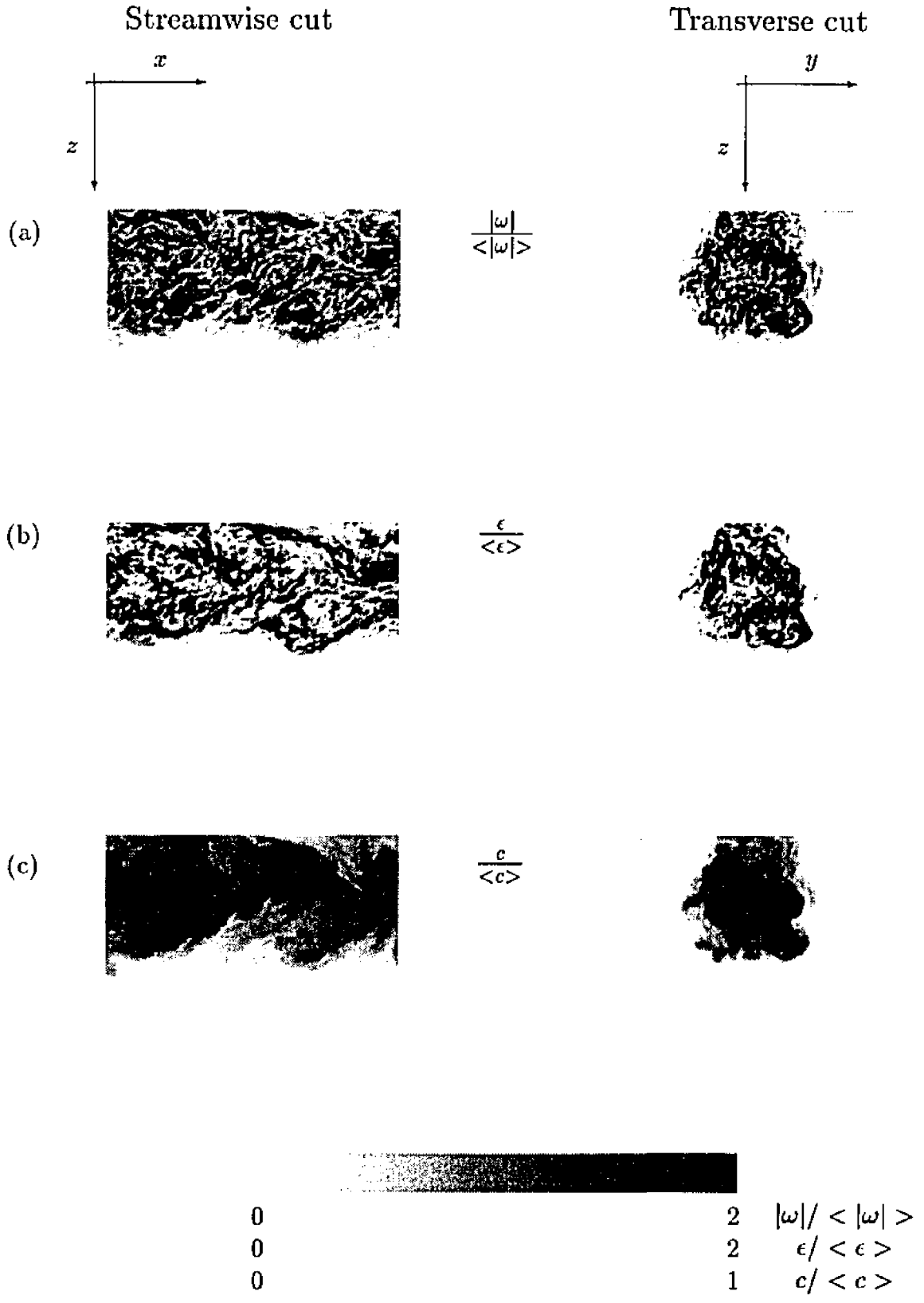

Figure 5.5: Spatial distributions of the (a) fluctuating vorticity magnitude, (b) kinetic energy dissipation and (c) passive scalar fields in two perpendicular planar cuts through the jet for the deep jet (H/D =2.0) at $tU_o/R_o = 200$. Left column, plane $y = 0$, right column, plane $x = 1.38R_o$.

Figure 5.6: Three-dimensional view of the high intensity vortical structures and their associated kinetic energy dissipation fields in the deep jet (H/D =2.0) at $tU_o/R_o = 200$. The structures are visualized by isosurfaces of $|\omega|/ < |\omega| >= 2.5$ (dark gray) and $\epsilon/ < \epsilon >= 4.0$ (light gray).

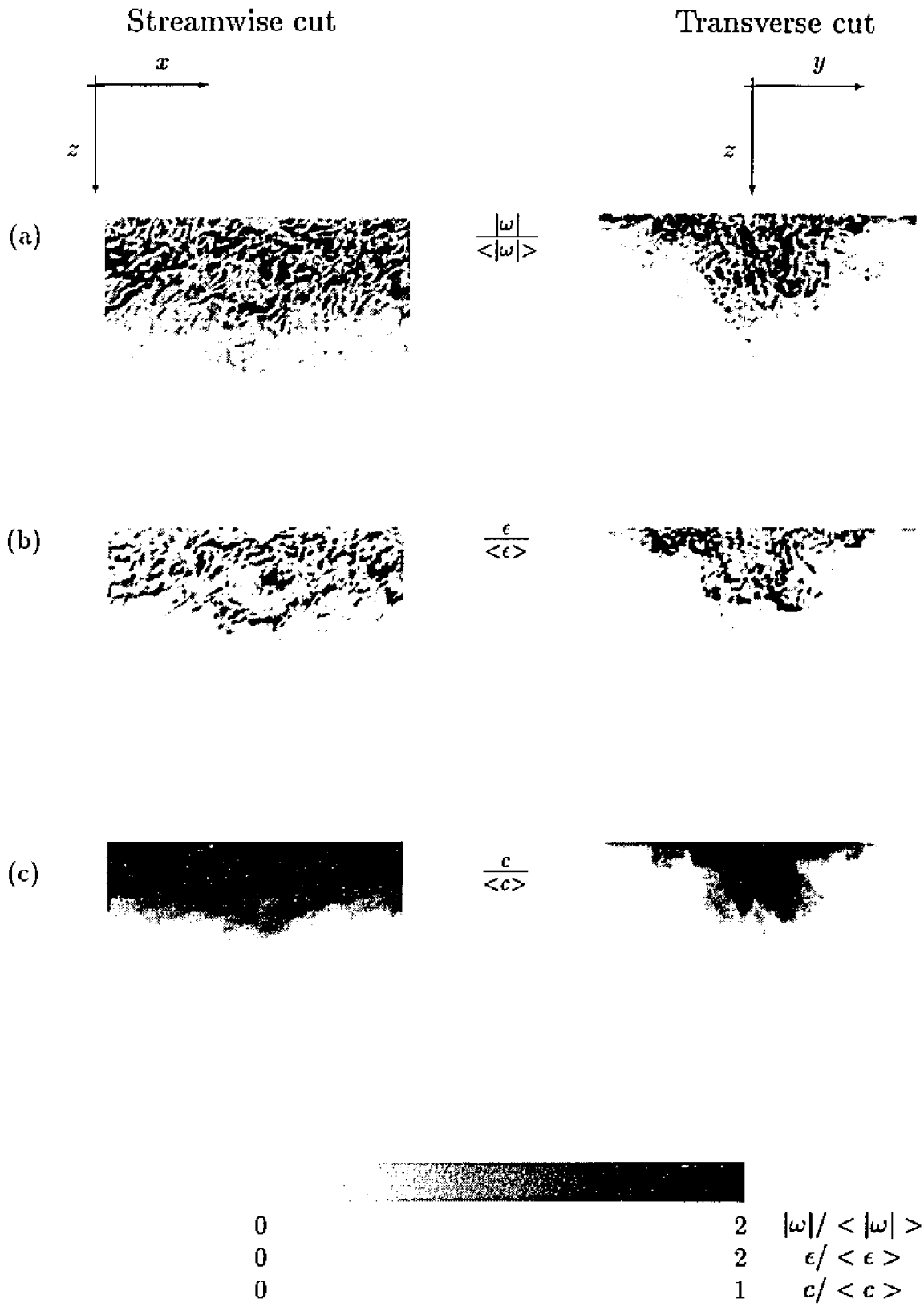

Figure 5.7: Spatial distributions of the (a) fluctuating vorticity magnitude, (b) kinetic energy dissipation and (c) passive scalar fields in two perpendicular planar cuts through the jet for the shallow jet (H/D =1.5) at $tU_o/R_o = 200$. Left column, plane $y = 0$, right column, plane $x = 1.38R_o$.

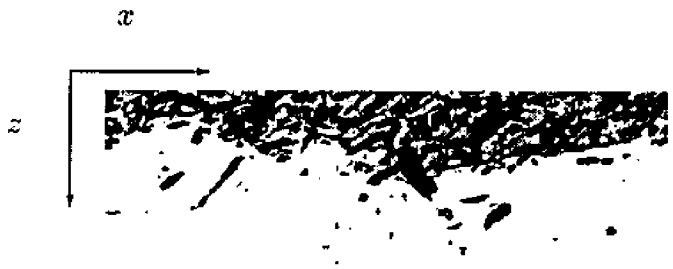

Figure 5.8: Three-dimensional view of the high intensity vortical structures and their associated kinetic energy dissipation fields in the shallow jet (H/D =1.0) at $tU_o/R_o = 200$. The structures are visualized by isosurfaces of $|\omega|/ < |\omega| >= 2.5$ (dark gray) and $\epsilon/ < \epsilon >= 4.0$ (light gray).

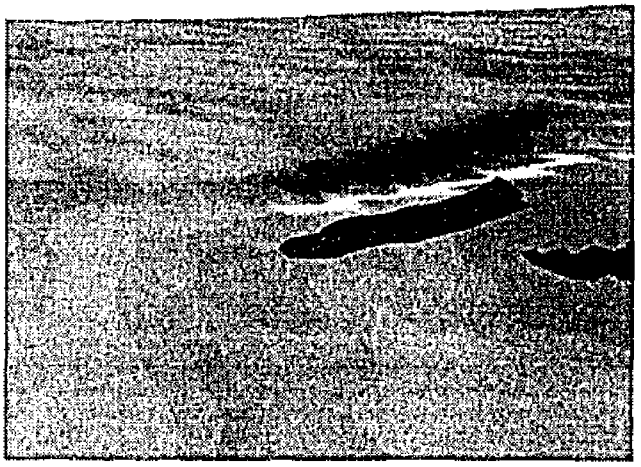

Figure 5.9: Close-up view of a vortex tube with axis parallel to the surface oriented along the direction of the mean flow strain field, with respective free-surface signature amplified for visualization.

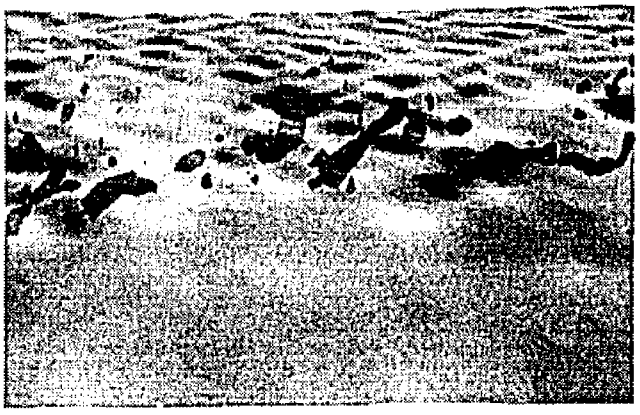

Figure 5.10: Close-up view of a vortex tubes with axis normal to the surface connected to the surface, with respective free-surface signature amplified for visualization.

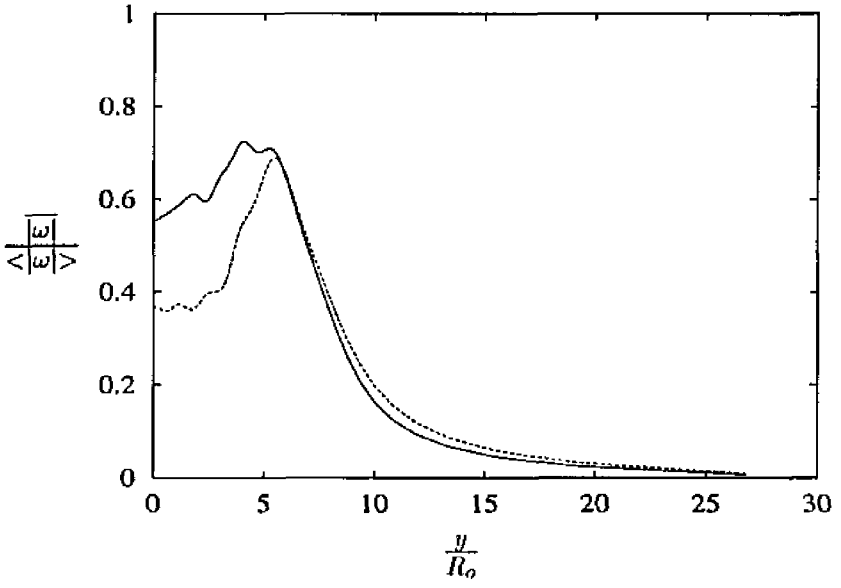

Figure 5.11: Profile of the mean normal vorticity magnitude in the plane z=0, for the shallow jet (H/D =1.0). — numerical result at time $tU_o/R_o = 150$, – – – at time $tU_o/R_o = 200$.

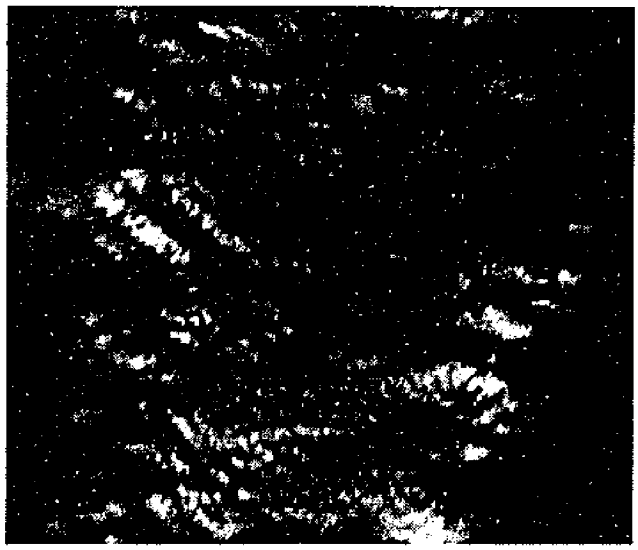

Figure 5.12: General view of the surface deformation, for the shallow jet (H/D =1.0) at $tU_o/R_o = 200$.

Figure 5.13: General view of the surface deformation and underlying vortical structures, for the shallow jet (H/D =1.0) at $tU_o/R_o = 200$.

CHAPTER VI

DYNAMICS OF FREE SURFACE TURBULENCE

In the previous chapters, the effect of the free surface on the structure of turbulence was discussed. In this chapter, the free-surface effects on the dynamics of turbulence will be addressed. Our interest lies, in particular, on the importance of two-dimensionality near the free surface and the modifications to existing models that are needed to account for these two-dimensional effects.

6.1 Energy Transfer in Spectral-Space

We begin by considering the spectral energy transfer, $T(k,t)$, representing the nonlinear transfer of energy to a mode k as a result of interactions between the turbulent fluctuations. The transfer $T(k,t)$ can be computed according to (see Appendix D)

$$T(k,t) = -\sum_{k-\frac{1}{2}<|\mathbf{k}|\leq k+\frac{1}{2}} \text{Real}\{\hat{u}'^{*}_{i}(\mathbf{k},t)\hat{N}'_{i}(\mathbf{k},t)\} \tag{6.1}$$

where $\hat{u}'^{*}_{i}(\mathbf{k},t)$ represents the complex conjugate of the Fourier transform of the velocity fluctuation $u_i(\mathbf{x},t)$, and $\hat{N}'_{i}(\mathbf{k},t)$ is the Fourier transform of the nonlinear term

$$N'_{\alpha}(\mathbf{x},t) = \frac{\partial}{\partial x_\beta}(u'_\alpha u'_\beta) + \frac{1}{\rho}\frac{\partial p''}{\partial x_\alpha} \tag{6.2}$$

with $\frac{1}{\rho}\frac{\partial^2 p''}{\partial x_\alpha \partial x_\alpha} = -\frac{\partial^2}{\partial x_\alpha \partial x_\beta}(u'_\alpha u'_\beta)$. $N'_i(\mathbf{x},t)$ represents the mutual nonlinear interactions between the turbulence fluctuations. The transfer defined in this manner has the same form as in isotropic turbulence and satisfies the same conservation properties, such as $\sum_k T(k,t) = 0$. To compute $T(k,t)$ in the free surface jet the jet data was reflected about the surface, the data was truncated to a box of size $L_x = L_y = L_z = 17.637R_o$ and the data was interpolated to Fourier representation using spectral interpolation.

Figure 6.1 shows the spectrum of energy transfer $T(k)$ in the shallow ($H/D = 1.0$) jet, at tU_o/z_o ranging from 160 to 200. As expected, the transfer is negative at the low wavenumbers and positive at the high wavenumbers, indicating that on average energy is being transferred from the large to the small scales of motion. As mentioned earlier, the transfer spectrum defined by equation (6.1) should satisfy the conservation property, $\sum_k T(k,t) = 0$. We have checked that this is indeed the case for the spectrum shown in figure 6.1.

6.2 Energy Transfer in mixed Spectral-Physical Space

The energy transfer, $T(k)$, as defined by equation 6.1 is appropriate for homogeneous turbulent flows, where there are no boundaries or spatial variation to influence the turbulence. For non-homogeneous flows, such as the free surface jet analyzed here, $T(k)$ is useful, but provides only an average description of the dynamics of the flow. To separate the effects of the surface on the dynamics of turbulence, it is necessary to be able to keep the spatial resolution in the direction normal to the surface in the energy transfer analysis. This can be achieved by defining the transfer

$$T(k_h,z) = -\sum_{k-\frac{1}{2}<|k_h|\leq k+\frac{1}{2}} \text{Real}\{\hat{u}'^*_i(k_x,k_y,z)\hat{N}'_i(k_x,k_y,z)\} \qquad (6.3)$$

where $k_h^2 = k_x^2 + k_y^2$ and $\hat{u'}_i(k_x, k_y, z)$ is the 2D Fourier transform (in x and y directions) of $u'_i(x, y, z)$ and $\hat{N'}_i(k_x, k_y, z)$ is the 2D Fourier transform (in x and y directions) of the nonlinear term, given by equation 6.2. The quantity $T(k_h, z)$ represents the net transfer of energy to the wavenumber k_h in the plane z. This transfer, however, is not solely the result of interactions between the turbulent fluctuation, but can also arise from the advection of energy to wavenumber k_h on plane z from another z plane. Consequently, $T(k_h, z)$ is not conserved in each plane; i.e. $\int T(k_h, z) dk_h \neq 0$. However, the volume average of $T(k_h, z)$ is conserved; namely, $\int \int T(k, z) dz\, dk = 0$. The integral $\int T(k_h, z) dz$ can be viewed as the projection of $T(\vec{k})$ onto a horizontal plane, for those wavenumbers $\vec{k}$ for which $k_x^2 + k_y^2 = k_h^2$.

Figure 6.1 shows a comparison between the volume average of $T(k_h, z)$ in the jet and the volume average of the true three-dimensional transfer $T(k)$. The similarity between the two curves indicates that the dynamics of both quantities is similar.

Figure 6.2 shows the energy transfer $T(k_h, z)$ at various depths from the free surface in the shallow jet ($H/D = 1.0$). The statistics have been average over five times for tU_o/R_0 ranging from 160 to 200. The transfer spectra shown in 6.1 demonstrated that on the average in the jet the dynamics of turbulence follows the rules of three-dimensional turbulence and is dominated by a net forward transfer of energy from the large scales of turbulent motion to the small scales. The same behavior is observed on the detailed transfer for planes not close to the free surface. However, as the free surface is approached (Figure 6.2 a) the turbulence attains a two-dimensional character and its energetics is dominated by a net reverse transfer of energy (backscatter of energy) to the large scales. Translated to an effective eddy viscosity, this means that the effective eddy viscosity may be negative near the free surface. In the intermediate locations (Figure 6.2 b-c), the overall dynamics

of turbulence is determined by a delicate balance between the three-dimensional dynamics of the deep turbulence and the two-dimensional dynamics of turbulence in the immediate vicinity of the free surface.

This transition to 'two-dimensional' turbulence in the immediate vicinity of the free surface has to be accurately captured in any turbulence models used for the prediction of free surface turbulent flows. This makes the modeling of such flows substantially different from the well-studied examples of wall-bounded or free-shear flows.

6.3 Subgrid-Scale Energy Transfer

The quantity $T(k)$ plotted in figure 6.1 represents the net transfer of energy to a scale k as a result of nonlinear interactions with all other scales of turbulent motion. A quantity of more practical interest in the development of subgrid scale models of turbulence is the energy transfer $T_S(k|k_m)$ to a large scale $k \leq k_m$ as a result of nonlinear interactions with scales having a wavenumber higher than a certain cutoff k_m (the subgrid scales). The subgrid-scale energy transfer, $T(k|k_m)$, can be computed as (see Appendix D).

$$T_S(k|k_m) = -\sum_{k-\frac{1}{2}<|\mathbf{k}|\leq k+\frac{1}{2}} \mathrm{Real}\{\hat{u}_i'^{*\mathcal{L}}(\mathbf{k})\hat{N}_i'^{\mathcal{L}|\mathcal{S}}(\mathbf{k})\} \tag{6.4}$$

where $\hat{u}_i'^{\mathcal{L}}$ is the large-scale disturbance velocity (defined by low-pass filtering the velocity field to include only scales with $|\vec{k}| < k_m$) and

$$N'^{\mathcal{L}|\mathcal{S}}_\alpha(\mathbf{x},t) = \frac{\partial}{\partial x_\beta}(u'_\alpha u'_\beta - u'^{\mathcal{L}}_\alpha u'^{\mathcal{L}}_\beta)^{\mathcal{L}} + \frac{1}{\rho}\frac{\partial}{\partial x_\alpha}p''^{\mathcal{L}|\mathcal{S}} \tag{6.5}$$

with

$$\frac{1}{\rho}\frac{\partial^2 p''^{\mathcal{L}|\mathcal{S}}}{\partial x_\alpha \partial x_\alpha} = -\frac{\partial^2}{\partial x_\alpha \partial x_\beta}(u'_\alpha u'_\beta - u'^{\mathcal{L}}_\alpha u'^{\mathcal{L}}_\beta)^{\mathcal{L}} \tag{6.6}$$

represents the nonlinear interactions of the large-scale fluctuating velocity field with the subgrid scales. By analogy to $T(k_h, z)$, one can also define

$$T_S(k_h|k_m, z) = -\sum_{k-\frac{1}{2}<|k_h|\leq k+\frac{1}{2}} \text{Real}\{\hat{u}'^{*\mathcal{L}}_i(k_x, k_y, z)\hat{N}'^{\mathcal{L}|\mathcal{S}}_i(k_x, k_y, z)\} \tag{6.7}$$

which represents the nonlinear interactions of the large-scale fluctuating velocity field with the subgrid scales in mixed spectral-physical space.

Using $T_S(k|k_m)$ one can compute the spectral eddy viscosity $\nu(k|k_m)$ acting on a (large-scale) mode k as a result of nonlinear interactions with all wavenumbers greater than k_m (the subgrid scales). As shown by Kraichnan (1976), $\nu(k|k_m)$ can be defined as

$$\nu(k|k_m) = -\frac{T_S(k|k_m)}{2k^2 E(k)}, \qquad k \leq k_m \tag{6.8}$$

By analogy, in the mixed representation one can define the spectral subgrid-scale eddy viscosity acting on wavenumber k_h at location z as

$$\nu(k_h|k_m, z) = -\frac{T_s(k_h|k_m, z)}{V(k_h|k_m, z))} \tag{6.9}$$

where

$$V(k_h|k_m, z) = -\sum_{k-\frac{1}{2}<|k_h|\leq k+\frac{1}{2}} \text{Real}\{\hat{u}'^{*\mathcal{L}}_i(k_x, k_y, z)\nabla^2\hat{u}'^{\mathcal{L}}_i(k_x, k_y, z)\} \tag{6.10}$$

represents the viscous effect of the large scales. The mean of $\nu(k_h|k_m, z)$ over all z physical locations is then the equivalent of $\nu(k_h|k_m)$,

$$\nu_m(k_h|k_m) = 1/L\int_0^L \nu(k_h|k_m, z)dz \tag{6.11}$$

Figure 6.3 shows the mean spectral eddy viscosity, $\nu_m(k|k_m)$, in the jet computed using equations (6.8) and (6.11), for four values of the cutoff wavenumber; $k_m < \eta >= 0.1$, 0.22 (in the inertial range) and $k_m < \eta >= 0.32$, 0.42 (in the dissipation range). Figure 6.3 also shows the predicted spectral eddy viscosity from Kraichnan's theory. The behavior of spectral eddy viscosity observed in this Figure is similar to that predicted by Kraichnan (1976) using a test-field model of turbulence in the limit of infinitely long inertial range. For all values of k_m, the curves of $\nu(k/k_m)$ plotted in Figure 6.3 have a similar character, consisting of a positive plateau at low wavenumbers and a cusp-like behavior near the cuttoff k_m. This is similar to Kraichman's curve for 3D turbulence. In 2D turbulence, however, Kraichman's theory shows a negative plateau at low wavenumbers. The plateaus in each curve represent the long range interactions between the resolved and the subgrid scales of motion while the cusps represent the interactions between scales near the cutoff. The area under the curve represents the net average effective eddy viscosity in the flow. In 2D turbulence, in the enstrophy transfering range, the negative area at the large scales should be same as the positive area at scales close to the cutoff (Kraichman, 1976). To see if such 2D effects are also present near the free surface in Figure 6.4 we plot $\nu(k/k_m, z)$ for various cutoff wavenumbers k_m and various depths z. It is seen that as the surface is approached, the positive plateau at low wavenumbers is replaced by negative values, similar to 2D turbulence. The area under the curve represents net transfer to the resolved scales. Depending on where the cutoff is, this area can be positive or negative.

The importance of this two-dimentionality depends on where the LES cutoff wavenumber lies with respect to the scales where the injection of energy occurs at the small scales, and on the relative importance of the two dimensionality effect,

which varies with the distance from the surface.

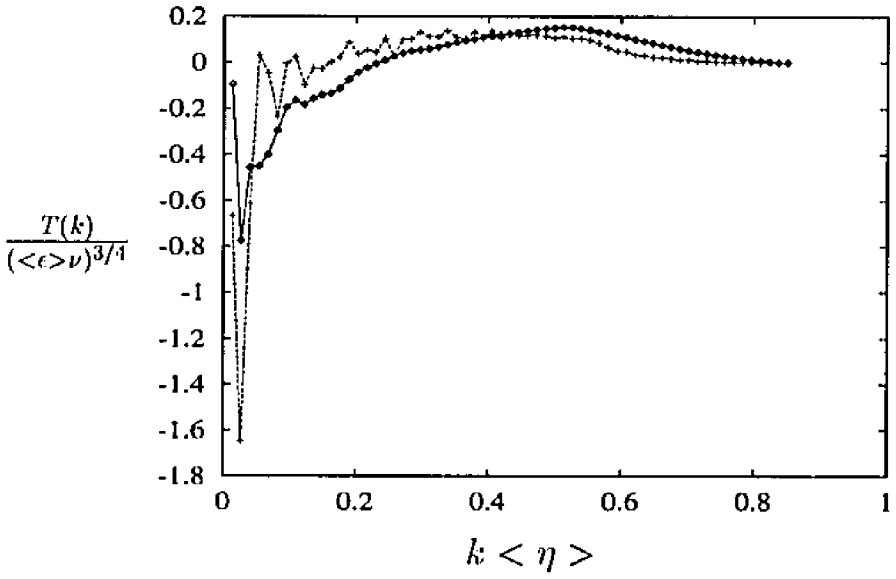

Figure 6.1: The transfer spectra of energy to a wavenumber in the shallow (H/D =1.0) jet at tU_o/R_o = 160 – 200 k; – – –, $T(k)$; ——, mean $T(k_h, z)$.

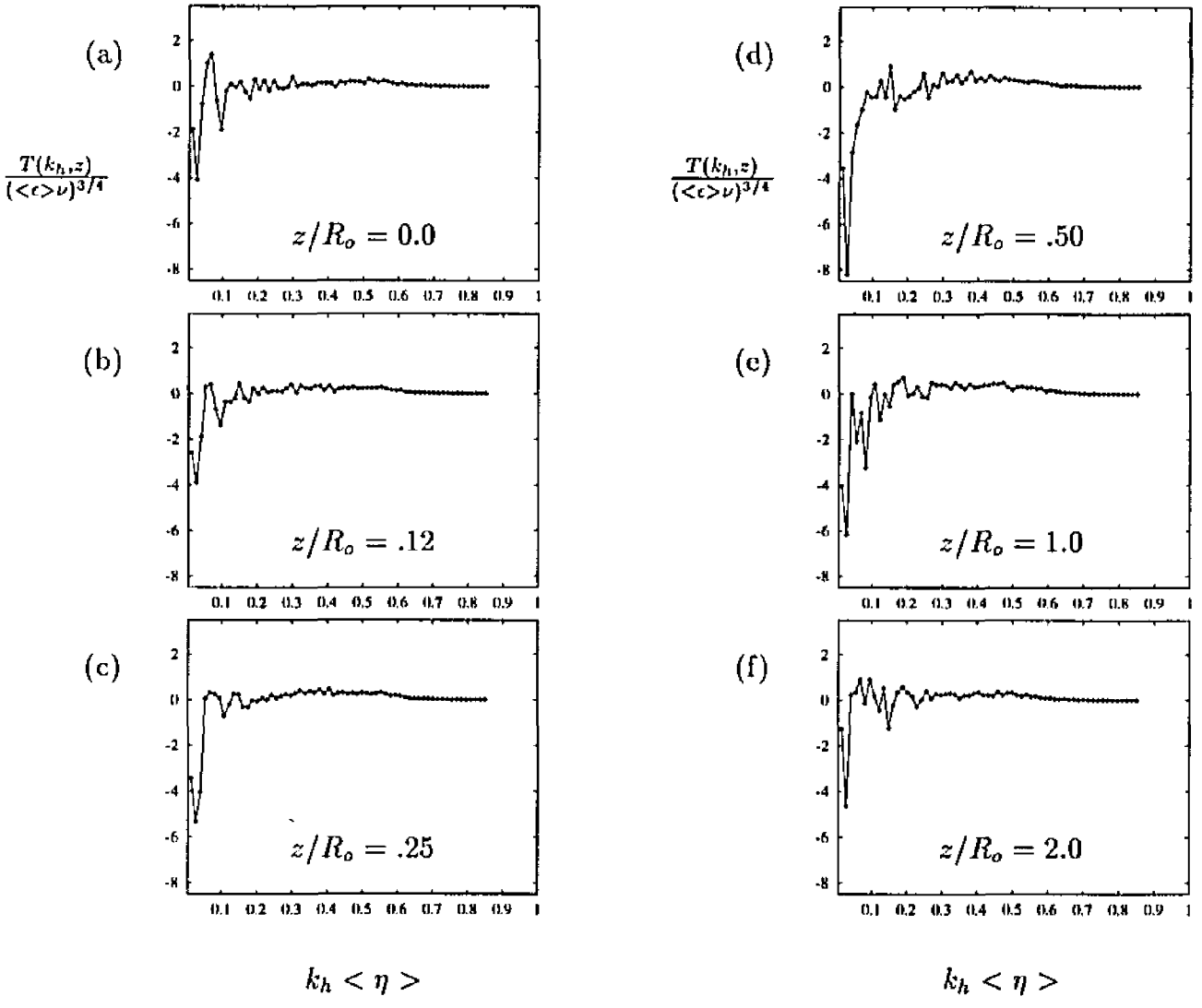

Figure 6.2: Energy transfer spectra, $T(k_h, z)$, in the shallow jet (H/D =1.0) at various depths z/R_o from the free surface

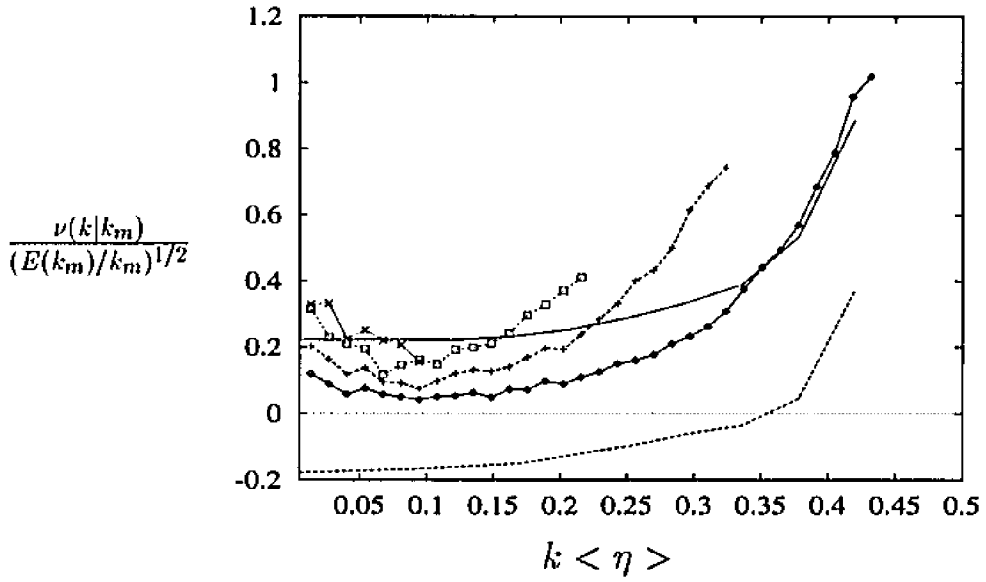

Figure 6.3: Mean eddy viscosity spectra for various cutoff wavenumbers, numerical results at time $tU_o/R_o = 160 - 200$, for the shallow jet (H/D =1.0); $\times$, $k_m < \eta >= 0.1$; $\square$, $k_m < \eta >= 0.22$; $+$, $k_m < \eta >= 0.32$; $\diamond$, $k_m < \eta >= 0.42$; ——, Kraichman (1976) 3D eddy viscosity spectra; — — —, Kraichman (1976) 2D eddy viscosity spectra.

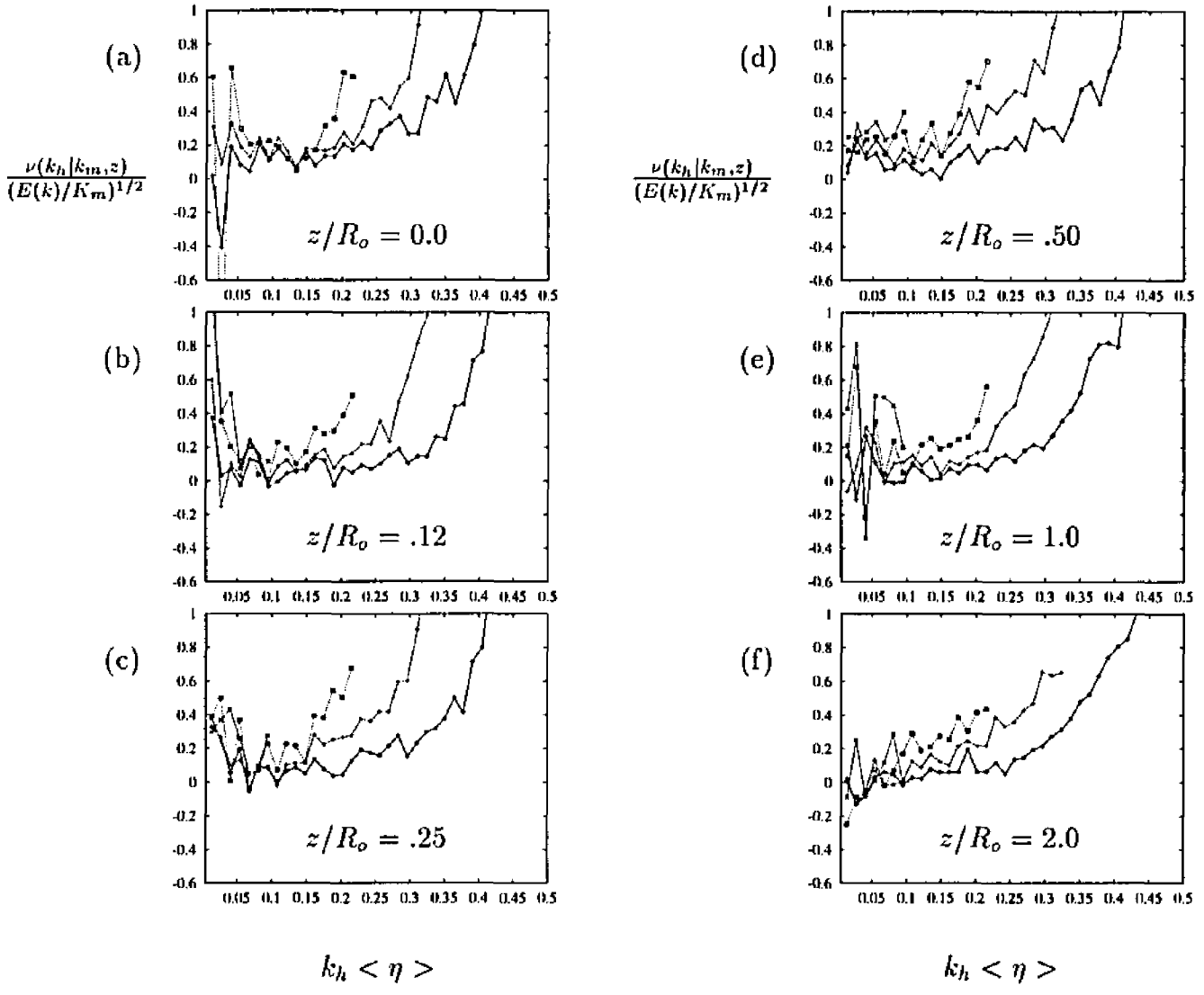

Figure 6.4: Eddy viscosity spectra, $\nu(k_h|k_m, z)$, in the shallow jet (H/D =1.0), at various depths z/R_o, at time $tU_o/R_o = 160 - 200$, $\times$, $k_m < \eta >= 0.1$; $\square$, $k_m < \eta >= 0.22$; $+$, $k_m < \eta >= 0.32$; $\diamond$, $k_m < \eta >= 0.42$.

CHAPTER VII

IMPLICATIONS FOR LES MODELLING OF FREE-SURFACE TURBULENT FLOWS

In this study, Direct Numerical Simulation (DNS) was used to investigate the dynamics of a free surface turbulent jet. DNS involves the explicit computation of all scales of turbulent motion and is an invaluable tool for the study of the detailed dynamics of turbulence for simple geometries and moderate Reynolds. However, it is a well known fact that, in the foreseeable future, Direct Numerical Simulations for realistic flows involving high Reynolds numbers and complex geometries will be outside the realm of computational capabilities. The computation of such realistics flows can only be accomplished if part of the scales of motion are modeled. Large Eddy Simulation (LES) is at present considered one of the most promissing techniques for the simulation of complex engineering flows, where simpler modeling approaches (such as single-point closure) are inadequate. In LES the 3-D, time dependent large scales of the motion are computed explicitly using a filtered Navier-Stokes equation, while the effect of the unresolved (or subgrid) scales is modeled. Obviously the success or failure of LES depends criticaly on the accurancy with which the subgrid interaction have been modeled.

As seen in the previous chapters, the interaction of turbulence with a free surface

leads to a reverse cascade (backscatter) of energy from the subgrid to the large scales of motion in the immediate vicinity of the free surface. For application in LES, it is important that the subgrid model be able to account for these effects.

In this chapter, the performance of various existing subgrid stress models in *a priori* tests of free surface turbulence is compared. The comparisons will include the Smagorinsky (1963) model, the dynamic eddy viscosity model of Germano *et al* (1991), and the Dynamic Two-Component model of Ansari *et al.* (1994).

7.1 Large Eddy Simulation Equations

In LES, the velocity field is decomposed into resolved (or filtered) components, $\overline{u_i}$, and subgrid (or residual) fields, u_i'. The equation governing the large scale components can be obtained by filtering the Navier-Stokes and continuity equations. The resulting equations, for the large scale velocity field $\overline{u}_i(\mathbf{x}, t)$ are given by

$$\frac{\partial \overline{u}_i}{\partial t} + \frac{\partial}{\partial x_i}(\overline{u}_i\,\overline{u}_j) = -\frac{\partial \overline{p}}{\partial x_i} - \frac{\partial \tau_{ij}}{\partial x_j} + \frac{1}{Re}\frac{\partial^2 \overline{u}_i}{\partial x_j \partial x_j} \tag{7.1}$$

$$\frac{\partial \overline{u}_i}{\partial x_i} = 0 \tag{7.2}$$

where the overbar denotes filtering at the LES cutoff (corresponding to scale k_m) for an appropriate filter $\overline{G}$ (one which computes with the derivative operators) defined in physical space as

$$\overline{f}(\mathbf{x}) = \int \overline{G}(\mathbf{x} - \mathbf{x}')f(\mathbf{x}')d\mathbf{x}' \tag{7.3}$$

Some common filters used in practice are the Gaussian filter given by

$$\overline{G}(\mathbf{x} - \mathbf{x}') = (6/\pi\Delta)^{1/2}\exp[6(\mathbf{x} - \mathbf{x}')^2/\Delta^2]$$

the box filter defined as

$$\overline{G}(\mathbf{x} - \mathbf{x}') = \begin{cases} 1/\Delta, & \text{for } |(\mathbf{x} - \mathbf{x}')| < \Delta/2 \\ 0, & \text{otherwise} \end{cases}$$

and the Fourier sharp cutoff filter which is most conveniently defined in Fourier space

$$\overline{G}(k_i) = \begin{cases} 1, & \text{if } k_i \leq k_m \\ 0, & \text{otherwise} \end{cases}$$

where $\overline{G}(k_i)$ is the Fourier coefficient of the filter function, $\overline{G}(\mathbf{x}-\mathbf{x}')$ and $k_m = \pi/\Delta$ is the cutoff wave number, In all of these filters Δ is the filter width in the physical space and k_m is the cutoff wavenumber which is related to Δ by $k_m = \pi/\Delta$.

The term

$$\tau_{ij}(\mathbf{x}, t) = \overline{u_i u_j} - \overline{u}_i \overline{u}_j \tag{7.4}$$

represents the nonlinear interactions of the large-scale flow field with the subgrid scales. This term needs to be modeled, or parameterized, and various works have addressed this issue with various degrees of success.

7.2 Smagorinsky Model

Smagorinsky (1963), based on the assumption of quasi-equilibrium turbulence, developed and applied an eddy viscosity model for the sub-grid stresses of turbulent atmospheric flows. Using dimensional arguments, Smagorinsky related the eddy viscosity, ν_T, to the resolvable-scale rate of strain tensor $\overline{S}_{ij}$

$$\nu_T = (C_s\Delta)^2|\overline{S}| \tag{7.5}$$

where

$$|\overline{S}| = (2\overline{S}_{ij}\overline{S}_{ij})^{1/2}$$

$$\overline{S}_{ij} = \frac{1}{2}\left(\frac{\partial \overline{u}_i}{\partial x_j} + \frac{\partial \overline{u}_i}{\partial x_j}\right)$$

C_S is a constant and Δ is a length scale, usually taken to be the filter width.

Because of its simplicity, this model has been widely used in Large Eddies Simulations, with reasonable success. However, this model has a number of limitations: (i) the model includes an empirical "constant" that needs to be tuned for various flows; (ii) the model can not account for backscatter of energy, and (iii) the model does not have the correct behavior near solid boundaries or in transitional or relaminarizing flows.

7.3 Germano DEM Model

The Dynamic Eddy Viscosity model of Germano *et al* (1991) is, in principle, similar to the Smagorinky model, but it tries to overcome some of its limitations. In particular, the model constant is computed dynamically during the course of the simulation. Similar to the Smagorinsky model, the subgrid-scale stress term

$$\tau_{ij} = \overline{u_i u_j} - \overline{u}_i \overline{u}_j \tag{7.6}$$

is modeled using an eddy viscosity assumption

$$\tau_{ij} - \frac{\delta_{ij}}{3} = -2\nu_T \overline{S}ij = -2C\overline{\Delta}^2 \overline{S}\,\overline{S}_{ij} \tag{7.7}$$

To find $C(x, y, z, t)$ dynamically, a second test filter $\widehat{\overline{G}}$ is applied to the Navier-Stokes equations. The subgrid stresses at this filter,

$$T_{ij} = \widehat{\overline{u_i u_j}} - \widehat{\overline{u}}_i \widehat{\overline{u}}_j \tag{7.8}$$

is modelled in the same way

$$T_{ij} - \frac{\delta_{ij}}{3} T_{kk} = -2C\widehat{\overline{\Delta}}^2 \widehat{\overline{S}}\,\widehat{\overline{S}}_{ij} \tag{7.9}$$

assuming $C(x, y, z, t)$ remains the same as in τ_{ij}.

Noting that

$$L_{ij} = \widehat{\overline{u_i u_j}} - \widehat{\overline{u_i}}\,\widehat{\overline{u_j}} \tag{7.10}$$

is known, the resolved turbulent stress can be related to the subgrid and subtest stresses by

$$L_{ij} = T_{ij} - \widehat{\tau_{ij}} \tag{7.11}$$

to compute C, resulting in

$$C(z,t) = -\frac{1}{2}\frac{L_{kl}\overline{S}_{kl}}{\widehat{\overline{\Delta}}^2|\widehat{\overline{S}}|\widehat{\overline{S}}_{mn}\overline{S}_{mn} - \overline{\Delta}^2\widehat{|\overline{S}|\overline{S}_{mn}}\overline{S}_{mn}} \tag{7.12}$$

In applying this expression to LES of wall-bounded flows, Germano *et al.* found that this expression could result in a negative or an indeterminate C, which would make the solution procedure unstable. To overcome this problem, they suggested that for homogeneous flows the denominator and numerator should be averaged in the homogeneous direction;

$$C(z,t) = -\frac{1}{2}\frac{< L_{kl}\overline{S}_{kl} >}{\widehat{\overline{\Delta}}^2 < |\widehat{\overline{S}}|\widehat{\overline{S}}_{mn}\overline{S}_{mn} > - \overline{\Delta}^2 < \widehat{|\overline{S}|\overline{S}_{mn}}\overline{S}_{mn} >} \tag{7.13}$$

The resulting C is always positive. It was later suggested by Lilly that a more consistent procedure for evaluating C is to compute C according to

$$C(z,t) = \frac{1}{2}\frac{< L_{kl}M_{kl} >}{< M_{ij}M_{ij} >} \tag{7.14}$$

where $M_{ij} = \widehat{\overline{\Delta}}^2 < |\widehat{\overline{S}}|\widehat{\overline{S}}_{mn} > - \overline{\Delta}^2 < \widehat{|\overline{S}|\overline{S}_{mn}} >$

The Germano *et al.* DEM has been shown to provide the appropriate behavior near solid boundaries and in transitional flows. It's main limitation is that it requires the averaging procedure described above, and as such is restricted to simple flows with homogeneous directions and can not account for local backscatter of energy.

7.4 The Two-Component Dynamic Subgrid-Scale Model

A dynamic two-component subgrid-scale model (DTM) was proposed by Ansari *et al.* (1994) to overcome the limitations of DEM. In this model, the effect of inter-

actions between the subgrid and the resolved scales far from the cutoff is modeled separately from the interactions between the subgrid- and the resolved scales close to the cutoff. The detailed derivation of the model has been given by Ansari *et al.* (1994). Here the more important features of the method will be briefly described. To model τ_{ij}, two additional filters $\widetilde{\overline{G}} = \tilde{G}\overline{G}$ and $\widehat{\widetilde{\overline{G}}} = \hat{G}\tilde{G}\overline{G}$ are introduced corresponding to cutoffs k_m/α and k_m/α^2 ($\alpha > 1$), respectively. If k_m, k_m/α and k_m/α^2 all fall within the inertial range, a model for the subgrid-scale stress τ_{ij} is constructed assuming that

$$\tau_{ij}\overline{S}_{ij} \simeq \mathcal{T}_{ij}\widetilde{\overline{S}}_{ij} \tag{7.15}$$

is a valid approximation. This is further approximated to

$$\tau_{ij} \simeq \frac{\mathcal{T}_{ij}\widetilde{\overline{S}}_{lm}\overline{S}_{lm}}{\overline{S}_{pq}\overline{S}_{pq}} \tag{7.16}$$

The subgrid-scale dissipation $\mathcal{T}_{ij}$ is modeled from the dynamics of the resolved scales using the two-component model

$$\mathcal{T}_{ij} - \frac{\delta_{ij}}{3}\mathcal{T}_{kk} = -2C\widetilde{\overline{\Delta}}^2|\widetilde{\overline{S}}|\widetilde{\overline{S}}_{ij} + (\widetilde{\overline{\overline{u}_i\overline{u}_j}} - \widetilde{\overline{\overline{u}}}_i\widetilde{\overline{\overline{u}}}_j) - \frac{\delta_{ij}}{3}(\widetilde{\overline{\overline{u}_k\overline{u}_k}} - \widetilde{\overline{\overline{u}}}_k\widetilde{\overline{\overline{u}}}_k) \tag{7.17}$$

where the first term is a Smagorinky type term to account for forward cascade of energy, and the second term is added to account for local backscatter of energy. With the exception of the coefficient C, all the other variables in equation (7.17) involve only large-scale quantities and are known. The coefficient $C(x, y, z, t)$ is computed dynamically using the procedure suggested by Germano *et al.* (1991), from the subgrid-scale stress T_{ij} (see equation 7.11) at $\widehat{\widetilde{\overline{G}}}$ filter level. Assuming that the two-component subgrid-scale model suggested in equation (7.17) can also be applied (with the same $C(x, y, z, t)$) to model T_{ij}, we obtain

$$T_{ij} - \frac{\delta_{ij}}{3}T_{kk} = -2C\widehat{\widetilde{\overline{\Delta}}}^2|\widehat{\widetilde{\overline{S}}}|\widehat{\widetilde{\overline{S}}}_{ij} + (\widehat{\widetilde{\overline{\overline{u}_i\overline{u}_j}}} - \widehat{\widetilde{\overline{\overline{u}}}}_i\widehat{\widetilde{\overline{\overline{u}}}}_j) - \frac{\delta_{ij}}{3}(\widehat{\widetilde{\overline{\overline{u}_k\overline{u}_k}}} - \widehat{\widetilde{\overline{\overline{u}}}}_k\widehat{\widetilde{\overline{\overline{u}}}}_k) \tag{7.18}$$

A dynamical equation for the computation of C can then be obtained (Germano et al. 1991) by noting that

$$L_{ij} = T_{ij} - \widehat{T_{ij}} = \widehat{\widetilde{\overline{u}}_i \widetilde{\overline{u}}_j} - \widehat{\widetilde{\overline{u}}}_i \widehat{\widetilde{\overline{u}}}_j \tag{7.19}$$

involves only large-scale quantities and is, therefore, known. Substitution of (7.9) and (7.10) into (7.11) gives

$$L_{ij} - \frac{\delta_{ij}}{3} L_{kk} = -2CM_{ij} + B_{ij} - \frac{\delta_{ij}}{3} B_{kk} \tag{7.20}$$

where

$$M_{ij} = \widehat{\widetilde{\Delta}}^2 \widehat{|\widetilde{\overline{S}}|\widetilde{\overline{S}}_{ij}} - \widehat{\widetilde{\Delta}}^2 \widehat{|\widetilde{\overline{S}}|} \widehat{\widetilde{\overline{S}}_{ij}} \tag{7.21}$$

and

$$B_{ij} = (\widehat{\widetilde{\overline{u}}_i \widetilde{\overline{u}}_j} - \widehat{\widetilde{\overline{u}}}_i \widehat{\widetilde{\overline{u}}}_j) - (\widehat{\widetilde{\overline{u}}_i \widetilde{\overline{u}}_j} - \widehat{\widetilde{\overline{u}}}_i \widehat{\widetilde{\overline{u}}}_j) \tag{7.22}$$

where it is assumed that the spatial variation of C is small at the level of the $\hat{G}$ filter so that $\hat{C} \simeq C$. The expression for C can then be obtained using the least-squared approach suggested by Lilly (1992).

$$C = -\frac{(L_{ij} - B_{ij}) M_{ij}}{2 M_{ij} M_{ij}} \tag{7.23}$$

Equations (7.8), (7.9) and (7.15) form a complete set, from which the subgrid-scale stress τ_{ij} can be evaluated. The model coefficients $C(x, y, z, t)$ computed from (7.15) are substituted directly into (7.9) without the need for any spatial averaging. Unlike the dynamic eddy viscosity model (Germano et al. 1991, Moin et al. 1991), in the DTM model this does not lead to numerical instability. This is because the intense backscatter of energy is accounted for separately (by the second and third terms on the RHS of equation 7.9). The role of the eddy viscosity term in the DTM model is primarily to account for the background forward transfer of energy.

The DTM subgrid-scale stress model yields zero subgrid-scale stresses in laminar flow and at solid walls, and has the correct asymptotic behavior in the near-wall region. The only adjustable parameter in this model is the ratio $\alpha = \widetilde{\overline{\Delta}}/\overline{\Delta} = \widehat{\widetilde{\Delta}}/\widetilde{\Delta}$. The *a priori* tests of Ansari *et al.* (1994) suggest that for $1 < \alpha < 2$ the model is very insensitive to the choice of α.

7.5 Evaluation of the Models

To evaluate the suitability of these models for LES of free-surface turbulence, the performance of each of the above models in the free-surface jet was tested against results from DNS in *a priori* tests. In *a priori* tests, the subgrid model is applied to the truncated DNS database of the turbulent free-surface jet and its predictions for the subgrid-scale dissipation are compared to results from DNS. To facilitate the application of the various models, the DNS data was interpolated onto a uniform three-dimensional Fourier grid using spectral interpolation. This allowed the use of a sharp Fourier cutoff filter, with the same filter width in all three directions. The cutoff k_m (corresponding to the LES filter $\overline{G}$) was chosen to be at $k_m < \eta >= 0.08$ or 0.20 and the other cutoffs were chosen with a filter ratio of $\alpha = 1.25$ for DTM, and $\alpha = 2$ for DEM.

Figure 7.1 and 7.2 show the spatial distributions of the subgrid-scale dissipation $\tau_{ij}\overline{S}_{ij}$ at the free surface (plane $z = 0$) in the shallow ($H/D = 1.0$) jet at the two cutoffs $k_m < \eta >= 0.08$ and 0.20, respectively. The subgrid-scale dissipation computed from the full DNS database is compared to the subgrid-scale dissipation predicted by the dynamic two-component model (DTM), the dynamic eddy-viscosity model (DEM) of Germano et al. (1991) and the Smagorinsky (1963) eddy viscosity model with a Smagorinsky constant of 0.1 ($C = .01$). The Germano model was implemented

with a test-filter-width to grid-filter-width ratio of 2, as recommended by Germano et al. (1991) and with the model coefficient computed after a spatial averaging was performed in the horizontal directions (i.e, according to equation 17 of Germano et al. (1991). The average subgrid dissipation computed from the DNS data, and the three models is shown in table 7.1. It can be seen that the dynamic two-component model not only predicts an average subgrid dissipation in better agreement with the DNS data compared to DEM, but also is far more successful in capturing the correct spatial distribution of the subgrid-scale dissipation (Figures 7.1-7.2). In particular, regions of intense forward and reverse transfer of energy are accurately described. In contrast, the structure of the subgrid-scale dissipation predicted by DEM is seen to be essentially identical to that predicted by the Smagorinsky model which has little correlation with the structure of the subgrid-scale dissipation field observed in the DNS database. The DTM ability to predict negative subgrid transfer (backscatter) is very promising and suggests that it should be able to account for the two-dimensionality effects associated with free-surface turbulence.

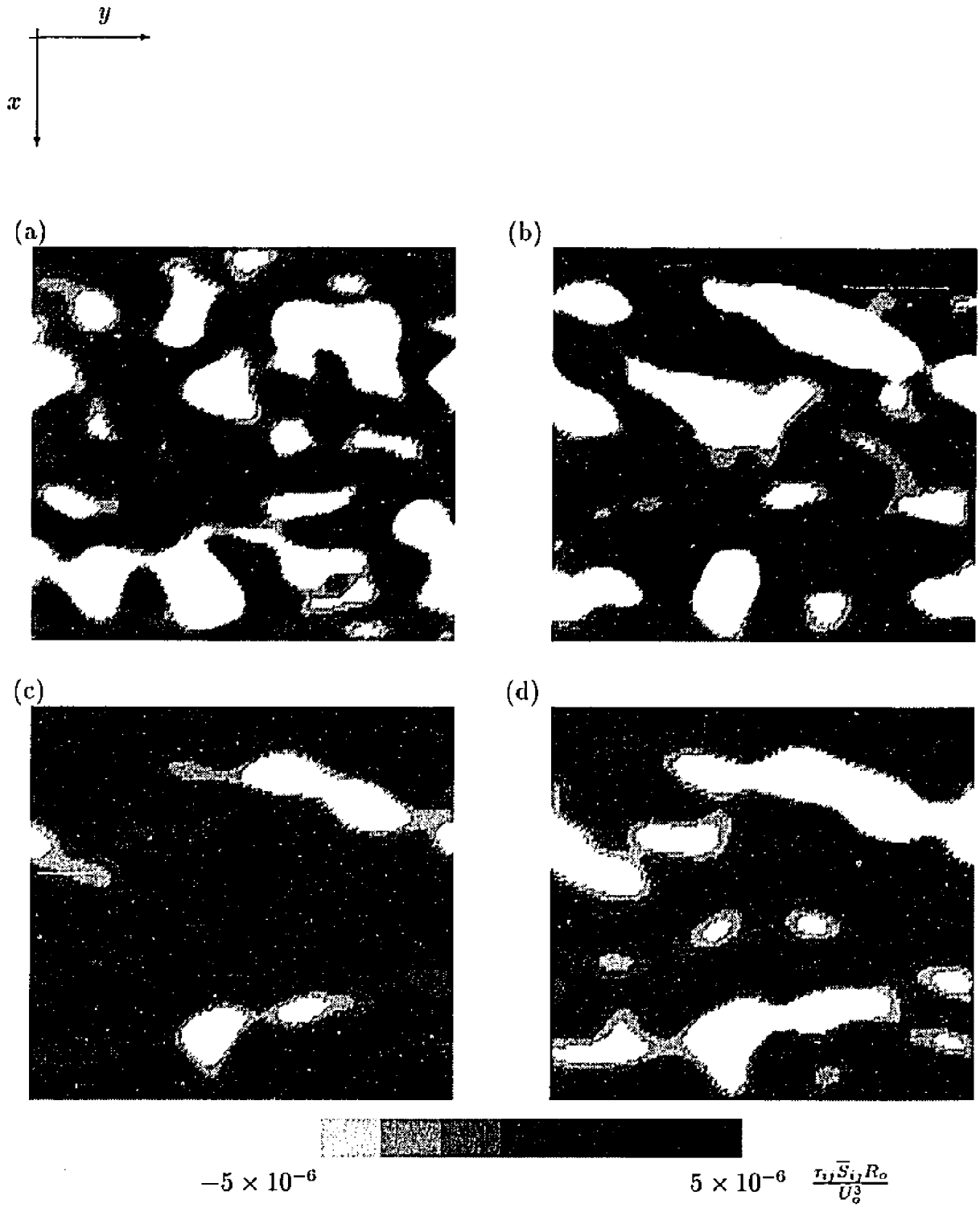

Figure 7.1: Subgrid-scale dissipation $\tau_{ij}\overline{S}_{ij}$ at the free surface ($z = 0$) in the shallow jet H/D =1.0 at $tU_o/R_o = 200$, for $k_m < \eta >= 0.8$; (a) DNS results, (b) DTM, (C) Smagorinsky model, (d) DEM.

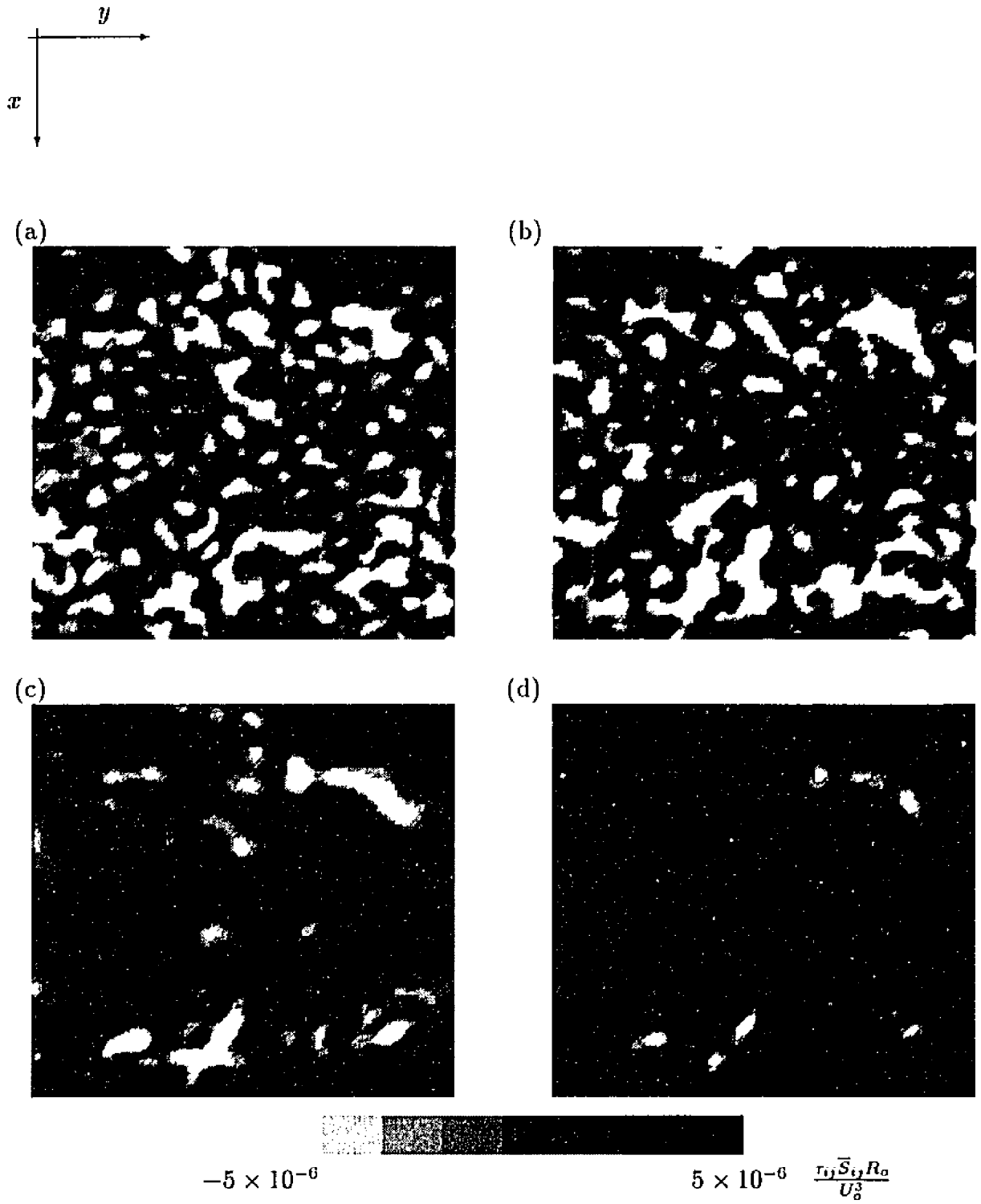

Figure 7.2: Subgrid-scale dissipation $\tau_{ij}\overline{S}_{ij}$ at the free surface ($z = 0$) in the shallow jet H/D =1.0 at $tU_o/R_o = 200$, for $k_m < \eta >= 0.20$; (a) DNS results, (b) DTM, (C) Smagorinsky model, (d) DEM.

	$K_m < \eta >= 0.20$ $\frac{\tau_{ij}\overline{S}_{ij}R_o}{U_o^3} \times 10^6$			$K_m < \eta >= 0.80$ $\frac{\tau_{ij}\overline{S}_{ij}R_o}{U_o^3} \times 10^6$		
	Min	Max	Mean	Min	Max	Mean
DNS	-17.872	89.649	2.787	-39.451	86.037	1.193
Smagorinky (1963)	0.00	13.304	0.994	0.00	23.989	0.874
Lilly (1992)	0.00	31.111	2.325	0.00	7.403	0.308
DTM	-68.358	86.394	2.003	-84.364	182.037	1.284

Table 7.1: Subgrid dissipation for the shallow jet (H/D =1), at tU_o/R_o =200 at the surface.

CHAPTER VIII

SUMMARY AND CONCLUSIONS

The dynamics of free surface turbulence at low Froude numbers has been investigated by direct numerical simulations of a series of temporally growing round turbulent jets issued below and parallel to a clean free surface. The jets had a Reynolds number of 10000 based on initial jet diameter and centerline velocity ($Re_\lambda \approx 100$), a Froude number of 0.1 and were issued at depths of 1.0, 1.5, and 2.0 jet diameters below the surface, respectively. A passive scalar with a Schmidt number of 0.7 was also included in the simulation.

The statistics and structure of the jet was found to be in good agreement with experimental measurements in free-surface jets. As the jet approaches the free-surface, the vertical turbulent fluctuations are damped in a 'surface layer' of magnitude on the order of one lateral Taylor microscale, and the horizontal turbulent fluctuations are amplified.

Two classes of organized vortical structures could be identified within the surface layer of the jet; (i) vortex tubes with axis parallel to the free surface oriented along the direction of the mean flow strain field and, (ii) vortex tubes with axis normal to the free surface connected to the surface. The interaction of these structures with the free surface leads to the establishment of a secondary flow which pumps the flow

upwards towards the free surface at the jet centerplane and outwards towards the edges of the jet on the surface. This phenomenon, known as the surface current, has also been observed in experimental studies. The parallel vortex tubes are subject to three-dimensional dynamics and the usual cascade of energy to the small scales. The reconnected vortex tubes, on the other hand, are not subject to strong vortex stretching near the free surface and form long-lasting coherent structures which grow with time and occasionally merge, leading to a reverse cascade of energy towards the large scales and the establishment of a nearly two-dimensional turbulent state in the immediate vicinity of the free surface.

Examination of the small-scale structure of the flow reveals the presence of coherent small-scale vortical structures in the form of vortex tubes with diameter on the order of 10 Kolmogorov scales and length on the order of an integral scale. These vortex tubes give rise to coherent regions of intense kinetic energy dissipation and intense scalar dissipation at their periphery, which have scales of the same order of magnitude as the scale at which the kinetic energy and scalar dissipation spectra attain a peak.

The presence of the free surface is found to affect the dynamics of turbulence within a 'surface layer' of thickness on the order of one lateral Taylor microscale. Within this layer, the turbulence has a two-dimensional character and is dominated by a net reverse transfer of energy to the large scales. These effects should be incorporated into any turbulence models intended for the prediction of free surface turbulent flows.

The implications of the two-dimensionality of the free-surface turbulent jet flow on the modeling of sub-grid has been analyzed. The performance of various subgrid models has been assessed by *a priori* testing. The dynamic two-component model

based on the dynamics of the resolved scales developed by Ansari *et al.* (1994) for LES of incompressible turbulence which captures the observed dual character of subgrid-scale energy transfer in this database has shown to be a very promising model. Two separate terms are included in this model; one representing the low-intensity background forward transfer of energy due to 'nonlocal' (in wavenumber space) energy exchanges, and the other representing the intense forward and reverse transfers of energy due to 'local' energy exchanges between scales near the LES cutoff. The former is modeled using a Smagorinsky-type eddy viscosity model. The latter is modeled using the dynamics of the velocity field in the neighborhood of the cutoff wavenumber. A dynamic procedure is used for computing the model coefficient dynamically, without the need for any external input. The only input parameter to the model is the ratio of test filter to LES filter, α. The model has been shown to be insensitive to the exact value of α. The model has the correct behavior in laminar and transitional flows and near solid boundaries.

Tests of the model show the model to be superior to existing subgrid models in being able to provide a spatial distribution of subgrid-scale dissipation in good agreement with results from filtered DNS in *a priori* tests.

APPENDICES

APPENDIX A

IMPLICIT SOLVER

A.1 Introduction

In this section we describe the numerical procedure used for the solution of the Poisson and Helmholtz equations, which arise from the discrete time integration of the vorticity and velocity fields (equations 2.15 and 2.16).

A.2 Solution of Second-order Poisson Operators

For the vorticity, for example, we need to solve

$$(\nabla^2 - \frac{2Re}{\Delta t})\omega_z^{n+1} = -(\nabla^2 + \frac{2Re}{\Delta t})\omega_z{}^n + s \tag{A.1}$$

where

$$s = \vec{k} \cdot \frac{3}{2}(\nabla \times (\vec{u} \times \vec{\omega}))^n - \frac{1}{2}(\nabla \times (\vec{u} \times \vec{\omega}))^{n-1}$$

subject to boundary conditions

$$\frac{\partial}{\partial z}\omega_z^{n+1}(z = 0) = 0 \tag{A.2}$$

$$\omega_z^{n+1}(z = \infty) = 0 \tag{A.3}$$

$$\omega_z^{n+1}(y = -\infty) = 0 \tag{A.4}$$

$$\omega_z^{n+1}(y=\infty)=0 \tag{A.5}$$

$$\text{periodic in } x \tag{A.6}$$

which is a Helmholtz-type equation, for each time step, that for simplicity we can re-write as

$$(\nabla^2-\alpha)u=f \tag{A.7}$$

Denoting by U and F the Fourier transforms (in the x direction) of u and f respectively, we may write

$$(\frac{\partial^2}{\partial y^2}+\frac{\partial^2}{\partial z^2}-k_x^2-\alpha)U(k_x,y,z)=F(k_x,y,z) \tag{A.8}$$

The discrete version of this equation can be written symbolically as:

$$(D_y^2+D_z^2-k_x^2-\alpha)U(k_x,y,z)=F(k_x,y,z) \tag{A.9}$$

where the discretized operators correspond to

$$D_y^2=\frac{\partial^2}{\partial y^2} \tag{A.10}$$

$$D_z^2=\frac{\partial^2}{\partial z^2} \tag{A.11}$$

at the interior points, and equations A.2-A.5 at the boundaries. This equation is solved using the collocation/diagonalization method proposed by Haidvogel and Zang (1979), and Haldenwang et al. (1984). In this method, the D_y^2 and D_z^2 operators are first diagonalized

$$D_y^2=E_y\Lambda_y E_y^{-1} \tag{A.12}$$

$$D_z^2=E_z\Lambda_z E_z^{-1} \tag{A.13}$$

where E and Λ are the matrices formed by the eigenvectors and eigenvalues of the one-dimensional D^2 operators.

The discretized Helmholtz equation A.14 then becomes

$$(E_y \Lambda_y E_y^{-1} + E_z \Lambda_z E_z^{-1} - (k^2 + \alpha)I)U = F \tag{A.14}$$

which can be solved for U to give

$$U = E_y E_z \frac{1}{\Lambda_y + \Lambda_z - k^2 - \alpha} E_y^{-1} E_z^{-1} F \tag{A.15}$$

In practice the discretized D^2 operator matrices are diagonalized as a pre-processing step. The solution of each Helmholtz operator during each time step involves the combination of four matrix-vector products and the product of a diagonal matrix with a vector. This requires $O(mnp^2 + mn^2p)$ operations, roughly twice as many as a double Fourier, single Chebyshev code.

A.3 Solution of Fourth-order Operators

The fourth-order equation for the z component of the velocity, w

$$(\nabla^2 - \frac{2Re}{\Delta t})\nabla^2 w^{n+1} = g \tag{A.16}$$

where

$$g = \mathbf{k} \cdot curl^2(\frac{3}{2}(\mathbf{v} \times \omega + \mathbf{f})^n - \frac{1}{2}(\mathbf{v} \times \omega + \mathbf{f})^{n-1}) + (\nabla^2 + \frac{2Re}{\Delta t})(\nabla^2)w^n \tag{A.17}$$

was solved using an analytical Green's function approach (Domaradzki 1990). The fourth-order equation can be split into two second-oder equations,

$$(\nabla^2 - \frac{2Re}{\Delta t})\xi^{n+1} = g \tag{A.18}$$

$$\nabla^2 w^{n+1} = \xi \tag{A.19}$$

These equations need to be solved subject to boundary conditions

$$w(y = \infty) = 0 \tag{A.20}$$

$$w(y=-\infty)=0 \tag{A.21}$$

$$\frac{\partial^2}{\partial y^2}w(y=\infty)=0 \tag{A.22}$$

$$\frac{\partial^2}{\partial y^2}w(y=-\infty)=0 \tag{A.23}$$

$$\frac{\partial}{\partial z}w(z=0)=a(x,y) \tag{A.24}$$

$$\frac{\partial^2}{\partial z^2}w(z=0)=b(x,y) \tag{A.25}$$

$$w(z=\infty)=0 \tag{A.26}$$

$$\frac{\partial^2}{\partial y^2}w(z=\infty)=0 \tag{A.27}$$

$$\text{periodic in } x \tag{A.28}$$

The two equations are couppled through the bondary conditions. They can be uncouppled by using an analytical Green's functions approach. The solution is decomposed into two contributions:

$$w(x,y,z)=w_p(x,y,z)+w^+(x,y,z) \tag{A.29}$$

where w_p is the solution of equation (20), (21), and (22), with homogeneous boundary conditions $\xi_p(y=\pm\infty)=w_p(y=\pm\infty)=\xi_p(z=0,\infty)=w_p(z=0,\infty)=0$, and w^+ is a Green's function which is obtained by solving,

$$(\nabla^2-\frac{2Re}{\Delta t})\nabla^2 w^+=0 \tag{A.30}$$

subject to boundary conditions:

$$w^+(y=\infty)=0 \tag{A.31}$$

$$w^+(y=-\infty)=0 \tag{A.32}$$

$$\frac{\partial^2}{\partial y^2}w^+(y=\infty)=0 \tag{A.33}$$

$$\frac{\partial^2}{\partial y^2} w^+(y = -\infty) = 0 \tag{A.34}$$

$$\frac{\partial}{\partial z} w^+(z = 0) = a(x, y) - \frac{\partial}{\partial z} w_p(z = 0) \tag{A.35}$$

$$\frac{\partial^2}{\partial z^2} w^+(z = 0) = b(x, y) - \frac{\partial^2}{\partial z^2} w_p(z = 0) \tag{A.36}$$

$$w^+(z = \infty) = 0 \tag{A.37}$$

$$\frac{\partial^2}{\partial z^2} w^+(z = \infty) = 0 \tag{A.38}$$

$$\text{periodic in } x \tag{A.39}$$

To find the soluiton to (A.30-A39) we take the Fourier transform of the equations in the x direction and diagonalize the equations in the y direction. Then A.34 becomes

$$(D_z^2 E_y^{-1} + \Lambda_y E_y^{-1} - k_x^2 E_y^{-1} - \frac{2Re}{\Delta t} E_y^{-1})(D_z^2 E_y^{-1} + \Lambda_y E_y^{-1} - k_x^2 E_y^{-1}) W^+ = 0 \tag{A.40}$$

where $W^+(k_x, y, z)$ is the x-Fourier transform of w^+, E_y and Λ_y are the matrices formed by the eigenvectors and eigenvalues of the one-dimensional D_y^2. Defining $\tilde{W}^+$ as $\tilde{W}^+ = E_y^{-1} W^+$ we get

$$(D_z^2 + \Lambda_y - k_x^2 - \frac{2Re}{\Delta t})(D_z^2 + \Lambda_y - k_x^2)\tilde{W}^+ = 0 \tag{A.41}$$

which has the general solution

$$\tilde{W}^+(k_x, \Lambda_y, z) = c_1 e^{-\kappa_1 z} + c_2 e^{-\kappa_2 z} \tag{A.42}$$

where

$$\kappa_1^2 = -\Lambda_y + k_x^2 + \frac{2Re}{\Delta t} \tag{A.43}$$

$$\kappa_2^2 = -\Lambda_y + k_x^2 \tag{A.44}$$

The coefficients c_1 and c_2 are chosen such that the boundary conditions (A.35 and A.36) are satisfied,

$$\frac{\partial}{\partial z}\tilde{W}^{+}(z=0) = -\kappa_1 c_1 - \kappa_2 c_2 = \tilde{A}(k_x, \Lambda_y) - \frac{\partial}{\partial z}\tilde{W}_p(z=0) \tag{A.45}$$

$$\frac{\partial^2}{\partial z^2}\tilde{W}^{+}(z=0) = \kappa_1^2 c_1 + \kappa_2^2 c_2 = \tilde{B}(k_x, \Lambda_y) - \frac{\partial^2}{\partial z^2}\tilde{W}_p(z=0) \tag{A.46}$$

where $A(\tilde{k_x}, y) = E_y^{-1} A(k_x, \Lambda_y)$, $B(\tilde{k_x}, y) = E_y^{-1} B(k_x, \Lambda_y)$ and A and B are x Fourier transform of a and b.

Once c_1 and c_2 are found, the solution is obtained as:

$$W(k_x, y, z) = E_y(\tilde{W}_p + \tilde{W}^{+}) \tag{A.47}$$

APPENDIX B

PARALLEL PSEUDO-SPECTRAL ALGORITHM

B.1 Introduction

In this section we describe the steps required to parallelize the Fourier-Double Chebyshev pseudo-spectral method described on §2. for non-homogeneous turbulence on a medium grained, distributed memory MIMD computer. A similar Double Fourier-Chebyshev code has been described by Mangiavacchi and Akhavan (1993). The pseudo-spectral approach not only leads to improved accuracy but also to work-intensive concurrent native parallelism with minimal communication, allowing to reach MFLOPS ratings surpassing today's vector supercomputers, and high parallel efficiencies.

The governing equations (2.3), (2.4), and (2.5), are solved by expanding the flow variables in Fourier series in the streamwise (x) directions, and mapped Chebyshev polynomials in the spanwise (y), and normal or transverse (z) direction. The second-order Adams-Bashforth scheme is used for the discretization of the nonlinear and pressure terms, and the second-order Crank-Nicholson scheme in the viscous term. The discretized Navier-Stokes equation is given by

$$\frac{\mathbf{v}^{n+1}-\mathbf{v}^{n}}{\Delta t}=\frac{3}{2}(\mathbf{v}\times\omega-\nabla\Pi)^{n}-\frac{1}{2}(\mathbf{v}\times\omega-\nabla\Pi)^{n-1}+\frac{1}{2Re}(\nabla^{2}\mathbf{v}^{n+1}+\nabla^{2}\mathbf{v}^{n}). \quad \text{(B.1)}$$

Equation (2) is split into two steps: one containing the nonlinear terms, and one combining the pressure and viscous terms. To solve the second step equations the analytical Green's function approach is applied. Other time-stepping methods could be implemented similarly.

B.2 The Parallel Code

The parallelization of the code is based on a "domain decomposition" approach in *latu sensu*. We may note that the time-stepping algorithm involves three kinds of operators: (i) the nonlinear terms, (ii) the evaluation of inverse Poisson operators, and (iii) the discrete Fourier transforms. The nonlinear term computation in physical space involves only velocities and vorticities at that same physical location. If the data is distributed among the nodes such that each node contains all the variables for a certain physical region, all computations involved in the nonlinear step can be done in parallel without communications. The inverse Poisson operator in Fourier Space is diagonal in the x direction, the domain can be divided in groups of or yz planes in Fourier space, and the computations can still be performed without communications. The same applies to the computation of the vorticity. Assigning an equal number of planes to each processor either in Fourier space or in physical space guarantees load balance. The transformation in the x direction, from physical space to Fourier space, and back, which requires a Fourier transform is the only operation that requires communication between nodes.

Assume p processors P_n are numbered by $n = 0, 1, \ldots, p-1$. If $\mathbf{v}(1..N_x, 1..N_y, 1..N_z)$ is an array containing real data $\mathbf{v}$ at the respective physical points, when in Fourier

space the same amount of storage will be required to contain the complex array $\hat{\mathbf{v}}(1..N_x/2, 1..N_y, 1..N_z)$. In Fourier space we distribute data among the nodes such that processor P_n will have in its local memory $\hat{\mathbf{v}}(1+n.N_x/2p..(n+1)N_x/2p, 1..N_y, 1..N_z)$. When data is stored in this way, the inversion of the elliptic operators in the y and z directions can be done without communication, and the x direction is uncoupled (the elliptic operator is diagonal). The same applies to the computation of the vorticity. Data in the x (Fourier) direction is now distributed among processors. Therefore, to proceed and perform the 1-D FFTs will require communication. There are two possible options to proceed: (i) to compute the 1-d FFT keeping the data distributed in the x direction across nodes; (ii) to transpose the data before the computation. Since the number of operations in both approaches is essentially the same, the total amount of communication can be minimized using the transposition, and as single node library FFT routine performance is very high, we decided to follow the transpose approach.

After the transposition, each node will contain $\hat{\mathbf{v}}(1..N_x/2, 1+nN_y/p..(n+1)N_y/p, 1..N_z)$ complex modes. When data is stored in this way, 1-D FFTs in the x direction can be performed concurrently, without communication, on the whole data.

To avoid edge contention and have an "in place" algorithm, reducing the amount of scratch memory, we use some properties of the binary hypercube addressing method, such that at each step of the communication algorithm the processors are divided in pairs, and each processor only communicates with its pair. At each step a different set of pairs is defined, using the concept of relative address.

The transposition algorithm can be summarized as follows:

- For i=1, 2, ...,$p-1$ do:

- Each node m collects and sends to $n = XOR(m, i)$ all blocks that have node n as final destination, and replaces them with the blocks that receives from n.

- Unshuffle the resulting data in each node.

This algorithm combined with the routing algorithm used by the iPSC/860 hardware avoids edge contention.

The Poisson operator is diagonal in the Fourier x directions. In the general case of a mapped Chebyshev expansion the solution in the y and z directions requires the inversion of a full matrix. Using Haidvogel-Zang [6] method, at each step requires two matrix-vector multiplies for each direction (y and z) at a cost proportional to $N_Y^(2)N_Z + N_Y N_Z^2$. After decomposition of the domain among the nodes, the Poisson operator will require $O(\frac{N_X N_Y N_Z^2}{p})$ computations per node at each time step, and no communications. The FFT's will require $O(\frac{N_X N_Y N_Z(\log_2 N_X + \log_2 N_Y + \log_2 N_Z)}{p})$ computations and $(p-1)$ bidirectional communications of length $\frac{N_X N_Y N_Z}{p^2}$ when using the described transposition algorithm. Since the latency time is much shorter than the communication time for large problem sizes, the total communication time is essentially $O(\frac{N_X N_Y N_Z}{p})$ Therefore the ratio of communications to computations is $O(\frac{1}{N_Z})$. Longer vectors result in better performance because vectorize better in the i860 processor. This will result in better performance for larger problems.

B.3 The Results

The methods described in the previous section have been implemented on the SDSC 64 node iPSC/860, and later on the SDSC 400 node Paragon. . All computations were performed using double precision (64 bits) arithmetic.

The most computationally intensive tasks are the FFTs, and the matrix-vector multiplies in the elliptic solvers. Vectorized all-Fortran codes for these tasks do not show very high performances. Much better single-node performance was obtained using optimized FFT and BLAS library routines. The matrix-vector multiply was performed using DGEMV BLAS routine. The performance of the elliptic solver increased with the size of the matrix, from 9.6 Mflops for $N_z = 64$ to 18.4 Mflops for $N_z = 256$.

The complex to complex factor-2 FFTs performance also increased with the length, varying from 8.0 Mflops for $N = 64$ to 12.8Mflops for $N = 256$. The average performance over the whole code for problems that fit on the memory of a single processor is not very impressive, because of the reduced length of the vectors involved. For example, in the $32 \times 32 \times 32$ size of problem the average performance is about 4.7 Mflops (table I).

With increasing problem sizes, using a larger number of nodes, the individual node performance can improve, as long as the communication overhead in the parallel code is moderate. Timings performed on tests with different numbers of processors and different resolutions are also shown in table I. A parallel efficiency is defined as $\eta = \frac{T_{computation}}{T_{total}}$ where T_{total} is the total execution time, and $T_{computation}$ is the time spent on the actual computation, which excludes communication, synchronization times, and other overheads due to parallelization of the code. Typically 50% of the execution time is spent on the elliptic solvers (matrix-vector multiply), 20% in the FFTs, 20% is the communication overhead, and 10% is used by the rest of the code. This is in contrast with the number of operations, where up to about 90% of the computations are performed in the elliptic solvers, and emphasizes the high performance of the matrix-vector multiplication library routines.

Problem Size ($N_x \times N_y \times N_z$)	32^3		64^3		128^3	
Number of Nodes	Total Mflops	Mflops per Node	Total Mflops	Mflops per Node	Total Mflops	Mflops per Node
1	4.661	4.661				
2	8.292	4.146				
4	14.88	3.720	24.02	6.004		
8	24.08	3.010	44.83	5.604		
16	31.92	1.995	76.34	4.771		
32			101.7	3.178	226.3	7.071
64					416.0	6.501

Table B.1: Mflops ratings for different problem sizes and cube dimensions.

Efficiencies of about 80%, and sustained rates in excess of 7 Mflops per node can be obtained for problems that scale with the size of the hypercube. The maximum sustained performance was obtained on 64 nodes, with 7.18 Mflops per node, for a total of 460 Mflops and an efficiency of 76%, when running the $128 \times 128 \times 256$ case. Execution time for this case was 37.4 seconds per time step. Due to its storage requirements this size problem cannot be executed "in core" on a CRAY YMP. The $128 \times 128 \times 128$ case on 64 nodes runs in 16.4 seconds per time step, which compares favorably by more than a factor of 2 with timings on a CRAY YMP, which requires 40 seconds per step for a vectorized code that utilizes very fast FFT routines and assembly coded matrix-vector products.

APPENDIX C

VISCOUS HYDRODYNAMIC STABILITY

In this section the methodology used to study the linear evolution of axisymmetric and helical perturbations on a temporally growing circular jet is described. The complete set of linearized viscous equations of stability is solved for the axisymmetric and helical modes using appropriate boundary conditions. The results can then be used as initial conditions to test the 3-D unsteady Navier-Stokes solver.

C.1 The Governing Equations

The basic flow field is a uni-directional jet with a velocity profile having components $U_r, 0, 0$, expressed in cylindrical coordinates x,r,ϕ respectively. On this mean flow field, we superimpose small velocity and pressure perturbations v'_x, v'_r, v'_ϕ and p'. The type of perturbations that are analysed in this study are given by:

$$u_x, u_r, u_\phi = R[\{F(r), iG(r), H(r)\}e^{in\phi+i\alpha(x-ct)}] \tag{C.1}$$

$$\frac{p}{\rho} = R[P(r)e^{in\phi+i\alpha(x-ct)}] \tag{C.2}$$

where α is the wave number and the imaginary part of the complex velocity $c = c_r + ic_i$ determines the stability of the jet to this particular perturbation. If we substitute the total velocity as $v = V + v'$ and $p = P + p'$, and linearize the equations, all

terms related to the mean flow drop out and we get a set of linearised equations for perturbations:

$$\frac{\partial v'}{\partial t} + v'_r \frac{dV}{dr} + U\frac{\partial v'}{\partial x} = -\frac{1}{\rho}\nabla p' + \frac{1}{R}\nabla^2 v' \tag{C.3}$$

Substituting (3) in (1)~(2), we obtain the scalar equations for the four unknowns F, G, H and P:

$$\alpha(U-c)F + U'G = -\alpha P - i\nu\{F'' + \frac{1}{r}F' - (\alpha^2 + \frac{n^2}{r^2})F\} \tag{C.4}$$

$$\alpha(U-c)G = P' - i\nu\{G'' + \frac{1}{r}G' - (\alpha^2 + \frac{n^2+1}{r^2})G - \frac{2n}{r^2}H\} \tag{C.5}$$

$$\alpha(U-c)H = \frac{n}{r}P - i\nu\{H'' + \frac{1}{r}H' - (\alpha^2 + \frac{n^2+1}{r^2})H - \frac{2n}{r^2}G\} \tag{C.6}$$

$$\alpha F + G' + \frac{1}{r}G + \frac{n}{r}H = 0 \tag{C.7}$$

in which a prime denotes differentiation with respect to r. The conditions to be satisfied at the outer boundary are

$$F, G, H, P \longrightarrow 0 \qquad as \qquad r \rightarrow \infty \tag{C.8}$$

At the inner boundary r=0, u_x and p must be independent of ϕ. Thus we have

$$\begin{aligned} F(0) = G(0) &= 0 \qquad n \neq 0 \\ G(0) = H(0) &= 0 \qquad n \neq 1 \\ G(0) &= -H(0) \qquad n = 1 \end{aligned} \tag{C.9}$$

C.2 Solution

To obtain the solution, it is convenient to deal with the governing equations separately for n=0 (axisymmetric perturbation) and $n \neq 0$ (helical perturbation), as done by Kambe(1969).

- $n = 0$

For axisymmetric perturbations ($\frac{\partial}{\partial\theta}$ and v_ϕ=0) H=0. Eliminating F and P from equations (C.4)~(C.7), we obtain the following fourth order equation for G:

$$\triangle_1^\alpha \triangle_1^\alpha G = i\alpha R\{(U-c)\triangle_1^\alpha G + WG\} \tag{C.10}$$

where

$$W = \frac{1}{r}U' - U''$$
$$\triangle_m^\alpha = \frac{d^2}{dr^2} + \frac{1}{r}\frac{d}{dr} - \frac{m^2}{r^2} - \alpha^2 \tag{C.11}$$

and R is the Reynolds number. The boundary conditions to be satisfied by G are

$$G(0) = 0 \qquad G(\infty) = 0 \qquad G'(\infty) = 0 \qquad G''(0) = 0 \tag{C.12}$$

- $n \neq 0$

In this case, it is convenient to introduce new variables S(r) and T(r) defined by

$$S = G - H$$
$$T = G + H \tag{C.13}$$

Eliminating F and P in (C.4)~(C.7), we obtain the system of governing equations for S and T as:

$$D_n \triangle_{1+n}^\alpha T - D_{-n}\triangle_{1-n}^\alpha S = i\alpha R\{(U-c)(D_nT - D_{-n}S) + U'(T-S)\} \tag{C.14}$$

$$E_n \triangle_{1+n}^\alpha T + E_{-n}\triangle_{1-n}^\alpha S = i\alpha R\{(U-c)(E_nT + E_{-n}S) - U'(T+S)\} \tag{C.15}$$

where

$$D_n = \frac{d}{dr} + \frac{1+n}{r} \qquad E_n = D_n + \frac{\alpha^2}{n} r \tag{C.16}$$

The boundary conditions for S and T are

$$S(\infty) = T(\infty) = T'(\infty) = S'(\infty) = 0$$

$$S(0) = T(0) = 0 \qquad \text{for } n \neq 1$$

$$S'(0) = T(0) = 0 \qquad \text{for } n = 1 \tag{C.17}$$

Equations C.10 with boundary conditions C.12, and C.14-C.15 with boundary conditions C.17 are discretized using mapped Chebyshev polynomials. The resulting generalized eigenvalue problem is solved using the subroutine GENEIGC to find the complex eigenvalues c, and EIGREVC is used to find the eigenvectors (G for $n = 0$, and T, S for $n \neq 0$) associated with each eigenvalue.

APPENDIX D

ENERGY TRANSFER IN SPECTRAL-SPACE

The spectral energy transfer, $T(k)$, in the jet representing the nonlinear transfer of energy to a mode k as a result of mutual interactions between the turbulent fluctuations can be computed by considering the Navier-Stokes equation for the fluctuating velocity field u'_α (see Hinze, 1975; chap. 4). In the physical space, u'_α satisfies

$$\frac{\partial u'_\alpha}{\partial t} + u'_3\frac{\partial U}{\partial x_3}\delta_{\alpha 1} + U\frac{\partial u'_\alpha}{\partial x_1} + \frac{\partial}{\partial x_\beta}(u'_\alpha u'_\beta) - \frac{\partial}{\partial x_3}(\overline{u'_\alpha u'_3}) = -\frac{1}{\rho}\frac{\partial p'}{\partial x_\alpha} + \nu\frac{\partial^2 u'_\alpha}{\partial x_\gamma \partial x_\gamma} \quad \text{(D.1)}$$

where $U = U(x_3)$ represents the mean velocity in the jet, and p' satisfies

$$\frac{1}{\rho}\frac{\partial^2 p'}{\partial x_\alpha \partial x_\alpha} = -\frac{\partial^2}{\partial x_\alpha \partial x_\beta}(u'_\alpha u'_\beta) - 2\frac{\partial u'_3}{\partial x_1}\frac{\partial U}{\partial x_3} + \frac{\partial^2}{\partial x_\alpha \partial x_3}(\overline{u'_\alpha u'_3}) \quad \text{(D.2)}$$

In symbolic form, equation 1 can be written as

$$(\frac{\partial}{\partial t} - \nu\nabla^2)u'_\alpha(\mathbf{x}, t) = -N'_\alpha(\mathbf{x}, t) - N'^{\mathcal{M}}_\alpha(\mathbf{x}, t) \quad \text{(D.3)}$$

where,

$$N'_\alpha(\mathbf{x}, t) = \frac{\partial}{\partial x_\beta}(u'_\alpha u'_\beta) + \frac{1}{\rho}\frac{\partial p''}{\partial x_\alpha} \quad \text{(D.4)}$$

with $\frac{1}{\rho}\frac{\partial^2 p''}{\partial x_\alpha \partial x_\alpha} = -\frac{\partial^2}{\partial x_\alpha \partial x_\beta}(u'_\alpha u'_\beta)$ represents the mutual nonlinear interactions between the turbulence fluctuations, and

$$N'^{\mathcal{M}}_\alpha(\mathbf{x}, t) = u'_3\frac{\partial U}{\partial x_3}\delta_{\alpha 1} + U\frac{\partial u'_\alpha}{\partial x_1} + \frac{\partial}{\partial x_3}(\overline{u'_\alpha u'_3}) + \frac{1}{\rho}\frac{\partial p'^{\mathcal{M}}}{\partial x_\alpha} \quad \text{(D.5)}$$

with $\frac{1}{\rho}\frac{\partial^2 p'^{\mathcal{M}}}{\partial x_\alpha \partial x_\alpha} = -2\frac{\partial u_3'}{\partial x_1}\frac{\partial U}{\partial x_3} + \frac{\partial^2}{\partial x_\alpha \partial x_3}(\overline{u_\alpha' u_3'})$ represents the nonlinear interactions of the fluctuating velocity with the the mean flow. The spectral transfer of energy to a wavenumber k can then be obtained from the Fourier transform of (3)

$$(\frac{\partial}{\partial t} + \nu k^2)\hat{u'}_\alpha(\mathbf{k},t) = -\hat{N'}_\alpha(\mathbf{k},t) - \hat{N'}_\alpha^{\mathcal{M}}(\mathbf{k},t) \tag{D.6}$$

by considering the evolution equation for the energy amplitude $\frac{1}{2}|\hat{u'}(\mathbf{k},t)|^2 = \frac{1}{2}\hat{u'}_\alpha(\mathbf{k},t)$ $\hat{u'}_\alpha^*(\mathbf{k},t)$, where hat denotes Fourier transform and asterisk denotes complex conjugate. It follows from (6) that

$$(\frac{\partial}{\partial t} + 2\nu k^2)\frac{|\hat{u'}(\mathbf{k},t)|^2}{2} = T(\mathbf{k},t) + T^{\mathcal{M}}(\mathbf{k},t) \tag{D.7}$$

where

$$T(\mathbf{k},t) = -Real\{\hat{u'}_\alpha^*(\mathbf{k},t)\hat{N'}_\alpha(\mathbf{k},t)\} \tag{D.8}$$

represents the nonlinear transfer of energy to a wavenumber k due to mutual interactions between the turbulent fluctuations and

$$T^{\mathcal{M}}(\mathbf{k},t) = -Real\{\hat{u'}_\alpha^*(\mathbf{k},t)\hat{N'}_\alpha^{\mathcal{M}}(\mathbf{k},t)\} \tag{D.9}$$

represents the production of turbulent energy by the mean shear and the transfer of energy to a wavenumber k as a result of the deformation of the turbulent eddies by the mean shear. The energy equation for a mode k can the be obtained by summing equation 7 for all modes with a wavelength $k - \frac{\Delta k}{2} < |\mathbf{k}| \leq k + \frac{\Delta k}{2}$

$$(\frac{\partial}{\partial t} + 2\nu k^2)E(k,t) = T(k,t) + T^{\mathcal{M}}(k,t) \tag{D.10}$$

where

$$E(k,t) = \sum_{k-\frac{\Delta k}{2}<|\mathbf{k}|\leq k+\frac{\Delta k}{2}} \frac{1}{2}|\hat{\mathbf{u}}'(\mathbf{k})|^2 \tag{D.11}$$

is the three-dimensional energy spectrum, and

$$T(k,t) = -\sum_{k-\frac{\Delta k}{2}<|\mathbf{k}|\leq k+\frac{\Delta k}{2}} Real\{\hat{u'}^{*}_{\alpha}(\mathbf{k},t)\hat{N'}_{\alpha}(\mathbf{k},t)\} \tag{D.12}$$

is the energy transfer spectrum in the jet. Note, in particular, that the transfer defined in this manner has the same form as in isotropic turbulence and satisfies the same conservations properties, such as for example that $\int_0^\infty T(k,t)dk = 0$.

Similarly, the subgrid-scale transfer of energy $T_S(k|k_m)$ to a scale k ($k < k_m$) due to nonlinear interactions with scales having a wavenumber greater than k_m (the subgrid scales) can be obtained by considering the evolution equation for the large-scale fluctuating velocity $u'^{\mathcal{L}}_{\alpha}(\mathbf{x},t)$. It follows from (3) that

$$(\frac{\partial}{\partial t} - \nu\nabla^2)u'^{\mathcal{L}}_{\alpha}(\mathbf{x},t) = -N'^{\mathcal{L}|\mathcal{L}}_{\alpha}(\mathbf{x},t) - N'^{\mathcal{L}|\mathcal{S}}_{\alpha}(\mathbf{x},t) - N'^{\mathcal{ML}}_{\alpha}(\mathbf{x},t) \tag{D.13}$$

where

$$N'^{\mathcal{L}|\mathcal{L}}_{\alpha}(\mathbf{x},t) = \frac{\partial}{\partial x_\beta}(u'^{\mathcal{L}}_{\alpha}u'^{\mathcal{L}}_{\beta})^{\mathcal{L}} + \frac{1}{\rho}\frac{\partial}{\partial x_\alpha}p''^{\mathcal{L}|\mathcal{L}} \tag{D.14}$$

with $\frac{1}{\rho}\frac{\partial^2 p''^{\mathcal{L}|\mathcal{L}}}{\partial x_\alpha \partial x_\alpha} = -\frac{\partial^2}{\partial x_\alpha \partial x_\beta}(u'^{\mathcal{L}}_{\alpha}u'^{\mathcal{L}}_{\beta})^{\mathcal{L}}$ represents the mutual nonlinear interactions between the large-scale velocity fluctuations, and

$$N'^{\mathcal{L}|\mathcal{S}}_{\alpha}(\mathbf{x},t) = \frac{\partial}{\partial x_\beta}(u'_{\alpha}u'_{\beta} - u'^{\mathcal{L}}_{\alpha}u'^{\mathcal{L}}_{\beta})^{\mathcal{L}} + \frac{1}{\rho}\frac{\partial}{\partial x_\alpha}p''^{\mathcal{L}|\mathcal{S}} \tag{D.15}$$

with

$$\frac{1}{\rho}\frac{\partial^2 p''^{\mathcal{L}|\mathcal{S}}}{\partial x_\alpha \partial x_\alpha} = -\frac{\partial^2}{\partial x_\alpha \partial x_\beta}(u'_{\alpha}u'_{\beta} - u'^{\mathcal{L}}_{\alpha}u'^{\mathcal{L}}_{\beta})^{\mathcal{L}} \tag{D.16}$$

represents the nonlinear interactions of the large-scale fluctuating velocity field with the subgrid scales. It follows by analogy with (10) that the large-scale turbulent energy spectrum $E^{\mathcal{L}}(k,t)$ is governed by

$$(\frac{\partial}{\partial t} + 2\nu k^2)E^{\mathcal{L}}(k,t) = T_L(k|k_m) + T_S(k|k_m) + T^{\mathcal{ML}}(k|k_m) \tag{D.17}$$

where

$$T_L(k|k_m) = - \sum_{k-\frac{\Delta k}{2}<|\mathbf{k}|\leq k+\frac{\Delta k}{2}} Real\{\hat{u}'^{*\mathcal{L}}_{\alpha}(\mathbf{k})\hat{N}'^{\mathcal{L}|\mathcal{L}}_{\alpha}(\mathbf{k})\} \tag{D.18}$$

represents the transfer of energy to the mode k as a result of mutual interactions between the large-scale velocity fluctuations, and

$$T_S(k|k_m) = - \sum_{k-\frac{\Delta k}{2}<|\mathbf{k}|\leq k+\frac{\Delta k}{2}} Real\{\hat{u}'^{*\mathcal{L}}_{\alpha}(\mathbf{k})\hat{N}'^{\mathcal{L}|\mathcal{S}}_{\alpha}(\mathbf{k})\} \tag{D.19}$$

represents the transfer of energy to the mode k as a result of interactions with the subgrid-scale velocity fluctuations.

BIBLIOGRAPHY

BIBLIOGRAPHY

[1] ABID, M. AND BRACHET, E. 1993 Numerical characterization of the dynamics of vortex filaments in round jets. *Phys. Fluids A* **5** (11), 2582-2584.

[2] ANSARI, A. 1993 Small-scale dynamics and subgrid interactions in turbulent shear flows. *Ph.D. Thesis, University of Michigan.*

[3] ANSARI, A., MANGIAVACCHI, N., AND AHKAVAN, R. 1994 Subgrid scale energy transfer in turbulent shear flows. *Phy. Fluids (In press)*

[4] ANTHONY, D.G. 1990 The influence of a free surface on the development of turbulence in a submerged jet. *Ph.D. Thesis, University of Michigan.*

[5] ANTHONY, D. G., HIRSA, A., AND WILLMARTH, W. W. 1991 On the interaction of a submerged turbulent jet with a clean or contaminated free surface. *Phy. of Fluids A* **3**, 245-247.

[6] ANTHONY, D. G. AND WILLMARTH, W. W. 1992 Turbulence measurements in a round jet beneath a free surface. *Journal of Fluid Mech.* **243**, 699-720.

[7] BARDINA, J. 1983 Improved turbulence models based on large eddy simulation of homogeneous, incompressible turbulent flows. *Ph.D. Thesis, Dept. Mech. Eng., Stanford University.*

[8] BERNAL, L. P. AND MADNIA, C. K. 1988 Interaction of a turbulent round jet with the free surface. *Proc 17th Symp. on Naval Hydrodynamics,* 79-87.

[9] BERNAL, L. P., HIRSA, A., KWON, J. T., AND WILLMARTH, W. W. 1989 On the interaction of vortex rings and pairs with a free surface for varying amounts of surface active agent. *Phy. Fluids A* **1**, 2001-2004.

[10] BERNAL, L. P. AND KWON, J. T. 1989 Vortex rings dynamics at a free surface. *Phy. Fluids A* **1**, 449-451.

[11] BRANCHER, P., CHOMAZ, J. M., AND HUERRE, P. 1994 Direct numerical simulations of round jets: Vortex induction and side jets. *Phys. Fluids* **6** (5).

[12] BRUMLEY, B.H. AND JIRKA, G.H. 1987 Near-surface turbulence in a grid-stirred Tank. *Journal of Fluid Mech.* **183**, 235-263.

[13] CANUTO, C., HUSSAINI, M.Y. , QUARTERONI, A., AND ZANG T.A. 1987 Spectral methods in fluid mechanics. *Springer-Verlag.*

[14] DOMARADZKI, A. J. 1990 An Analytic Green's Functions Method in Pseudo-Spectral Navier-Stokes Solvers for Boundary Layer and Channel Flows. *Journal of Computational Phys.* **88**, 232-242.

[15] DOMARADZKI, A. J. 1992 Nonlocal triad interactions and the dissipation range of isotropic turbulence. *Phys. Fluids A* **4**, 2037-2045.

[16] DOMMERMOUTH, D. G. 1993 The laminar interactions of a pair of vortex tubes with a free surface. *Journal of Fluid Mech.* **246**, 91-115.

[17] EVANS, J. T. 1955 Pneumatic and similar breakwaters. *Proc. Royal Soc. London A* **231**, 457-466.

[18] FABRIKANT, A. L. AND RAEVSKY, M. A. 1994 The influence of drift turbulence on surface gravity wave propagation. *Journal of Fluid Mech.* **262**, 141-156.

[19] GERMANO, M., PIOMELLI, U., MOIN, P., AND CABOT, W. H. 1991 A dynamic subgrid-scale eddy viscosity model. *Phys. Fluids A* **3**, 1760-1765.

[20] GHARIB, M., WEIGAND, A., AND NOVIKOV, E. 1992 Interaction of small scale turbulence with the free surface. *Bulletin of American Physical* **37**, 1763.

[21] GUTMARK, E. AND WYGNANSKI, I. 1976 The planar turbulent jet. *Journal of Fluid Mech.* **73**, 465-495.

[22] HAIDVOGEL, D. B. AND ZANG, T. 1979 The accurate solution of the poisson equation by expansion in chebyshev polynomials. *Journal of Computational Phys.* **30**, 167-180.

[23] HALDENWANG, P., LABROSSE, G., ABBOUDI, S., AND DEVILLE, M. 1984 Chebyshev 3-D spectral and 2-pseudospectral solvers for the Helmholtz equation. *Journal of Computational Phys.* **55**, 115-128.

[24] HINZE, J. 1975 Turbulence, McGraw-Hill.

[25] HIRSA, A. AND WILLMARTH, W. W. 1994 Measurements of vortex pair interaction with a clean or contaminated free surface. *Journal of Fluid Mech.* **259**, 25-45.

[26] HUNT, J. C. R. 1984 Turbulence structure in thermal convection and shear free boundary layers. *Journal of Fluid Mech.* **138**, 161-184.

[27] HUNT, J. C. R. 1984 Turbulence structure and turbulence diffusion near gas-liquid interfaces. *ed. W. Brutsaert & G. H. Jirka, Gas Transfer at Water Surfaces*, 67-82.

[28] HUNT, J. C. R. AND GRAHAM, J. M. R. 1978 Free-stream turbulence near plane boundaries. *Journal of Fluid Mech.* **84** (2), 209-235.

[29] KAMBE, T. 1969 The stability of an axisymmetric jet with parabolic profile. *Journal of the Physical Society of Japan* **26** (2), 566-575.

[30] JIMENEZ, J., WRAY, A. A., SAFFMAN, P. G., AND ROGALLO, R. S. 1992 The structure of intense vorticity in homogeneous isotropic turbulence. *CTR, Proc. Sum. Prog.*, 21-45.

[31] KRAICHNAN, R. H. 1976 Eddy viscosity in two and three dimensions. *Journal of Atmos. Sci.* **33**, 1521-1536.

[32] KOMORI, S., UEDA, H., OGINO, F., AND MIZUSHINA, T. 1982 Turbulence structure and transport mechanism at the surface in an open channel flow. *Intl. J. Heat Mass Transfer* **25**, 513-521.

[33] LAUNDER, B. E. AND RODI, W. 1981 The turbulent wall jet *Prog. Aerospace Sci.* **19**, 81-128.

[34] LAUNDER, B. E. AND RODI, W. 1983 The turbulent wall jet - Measurements and modeling *Annual Review of Fluid Mech.* **15**.

[35] LESIEUR, M. 1983 Introduction a la turbulence bidimensionnelle. *Journal de Mécanique Theo. et Appl.*, 5-20.

[36] LESSEN, M. AND SINGH, P. J. 1973 The stability of axisymmetric free shear layers. *Journal of Fluid Mech.* **60** (4), 433-457.

[37] LIEPMANN, D. 1990 The near-field dynamics and entrainment field of submerged and near-surface jets. *Ph.D. Thesis, University of California, San Diego.*

[38] LIEPMANN, D. AND GHARIB, M. 1992 The role of streamwise vorticity in the near-field entrainment of round jets. *Journal of Fluid Mech.* **245**, 643-662.

[39] LILLY, D. K. 1992 A proposed modification of the Germano subgrid scale closure method. *Phys. of Fluids A* **4**, 663.

[40] LONGUET-HIGGINS, M. S. AND STEWART, R. W. 1961 The changes in amplitude of short gravity waves on steady non-uniform currents. *Journal of Fluid Mech.* **10**, 529-549.

[41] LYDEN, J. D., HAMMOND, R. R., LYZENGA, D. R., AND SHUCHMAN, R. A. 1988 Synthetic Aperture Radar imaging of surface ship wakes. *Journal of Geophysical Research* **93** (C10), 12293-12303.

[42] MADNIA, C. K. AND BERNAL, L. P. 1989 Interaction of a turbulent round jet with the free surface. *Tech. Report University of Michigan, Aerospace dept.* **89-05.**

[43] MADNIA, C. K. AND BERNAL, L. P. 1994 Interaction of a turbulent round jet with the free surface. *Journal of Fluid Mech.* **261**, 305-332.

[44] MANGIAVACCHI, N., AND AKHAVAN, R. 1993 Direct numerical simulations of turbulent shear flows on distributed memory architectures. *Proc. 6th SIAM Conf. on Parallel Procedures in Sci. Comp.* **1**, 61-64.

[45] MILGRAM, J. H., PELTZER, R. D., AND GRIFFIN, O. M. 1993 Suppression of short sea waves in ship wakes: Measurements and observations. *Journal of Geophysical Research* **98** (C4), 7103-7114.

[46] MOIN, P., SQUIRES, K., CABOT, W., AND LEE, S. 1991 A dynamic subgrid-scale model for compressible turbulence and scalar transport. *Phys. of Fluids A* **3** (11), 2746-2757.

[47] MONIN, A. S. AND YAGLOM, A. M. 1981 Statistical Fluid Mechanics II. *MIT Press - Cambridge, Massachusetts.*

[48] MUMFORD, J. C. 1982 The structure of the large eddies in fully developed turbulent shear flows (Part 1. The plane jet). *Journal of Fluid Mech.* **118**, 241-268.

[49] MUNK, W. H., SCULLY-POWER, P., AND ZACHARIASEN, F. 1987 Ship wakes from Space, The Bakerian Lecture, 1986. *Proc. Royal Soc. London A* **412**, 231-254.

[50] ORSZAG, S.A. AND PATERA, A.T. 1983 Secondary Instability of Wall-Bounded Shear Flows. *Journal of Fluid Mech.* **128**, 347-385.

[51] PAO, Y. H. 1965 Structure of turbulent velocity and scalar fields at large wavenumbers. *Phys. of Fluids* **8**, 1063.

[52] RASHIDI, M., HETSRONI, G., AND BANERJEE, S. 1992 Wave-turbulence interactions in free-surface channel flows. *Phy. Fluids A*, **4**, (12), 2727-2738.

[53] RAJARATNAM, N. AND HUMPHRIES, J. A. 1984 Turbulent non-buoyant surface jets. *Journal of Hydraulic Res.* **22** (2), 103-115.

[54] RAJARATNAM, N. AND SUBRAMANYAN, S. 1985 Plane turbulent buoyant surface jets. *Journal of Hydraulic Res.* **23** (2), 131-146.

[55] ROGALLO, R. S. 1981 Numerical experiments in homogeneous turbulence. *NASA Tech. Mem.* **81315** (2), 51-54.

[56] ROOD, E. P. 1994 Interpreting vortex interactions with a free surface. *Journal of Fluids Eng.* **116**, 91-94.

[57] RUETSCH, G. R. AND MAXEY, M. R. 1991 Small-scale features of vorticity and passive scalar fields in homogeneous isotropic turbulence. *Phys. of Fluids A* **3**, 1587-1597.

[58] SARPKAYA, T. AND SUTHON, P. 1991 Interaction of a vortex couple with a free surface. *Experiments in Fluids* **11**, 205-217.

[59] SCHEFER, R. W., KERSTEIN A. R., NAMAZIAN, M., AND KELLY, J. 1994 Role of large-scale structure in a nonreacting turbulent CH4 jet. *Phys. of Fluids* **6**, 652-661 .

[60] SHE, Z. S., JACKSON, E., AND ORSZAG, S. A. 1990 Intermittent vortex structures in homogeneous isotropic turbulence. *Nature* **344**, 226-228.

[61] SMAGORINSKY, J. 1963 General circulation experiments with the primitive equations. *Mon. Weath. Rev.* **91**, 99-164.

[62] SWEAN, T. F., RAMBERG, S. E., PLESNIAK, M. W., AND STEWART, M. B. 1989 Turbulent surface jet in channel of limited depth. *Journal of Hydraulic Eng.* **115**, 1587-1606.

[63] SWEAN, T. F., RAMBERG, S. E., MINER, E.W. 1991 Anisotropy in a Turbulent Jet Near a Free Surface. *Journal of Fluids Eng.* **113**, 430-438.

[64] SONG, M., KACHMAN, N., KWON, J. T., BERNAL, L. P., AND TRYGGVASON, G. 1990 Vortex ring interaction with a free surface. *Proc 18th Symp. on Naval Hydrodynamics* , .

[65] TAYLOR, G. I. 1955 The action of surface current used as a breakwater. *Proc. Royal Soc. London A* **231**, 466-478.

[66] TAYLOR, G. I. 1962 Standing waves on a contracting or expanding current. *Journal of Fluid Mech.* **13**, 182-192.

[67] TENNEKES, H. AND LUMLEY, J. L. 1972 A first course in turbulence. *MIT Press - Cambridge, Massachusetts.*

[68] THOMAS, F. O., AND GOLDSCHMIDT, V. W. 1986 Structural characteristics of a developing turbulent planar jet. *Journal of Fluid Mech.* **163**, 227-256.

[69] TRYGGVASON, G., UNVERDI, S. O., SONG, M., AND ABDOLLAHI-ALIBEIK, J. 1991 Interaction of Vortices with a free surface and density interfaces. *Vortex dynamics and vortex methods. Lectures in Applied Math.* **28**, 679-699.

[70] VERZICCO, R, AND ORLANDI, P. 1994 Direct simulations of the transitional regime of a circular jet. *Phy. Fluids*, **6** (2), 751-759.

[71] VINCENT, A. AND MENEGUZZI, M. 1991 The spatial structure and statistical properties of homogeneous turbulence. *Journal of Fluid Mech.* **225**, 1-20.

[72] WALKER, D.T., CHEN, C.Y., AND WILLMARTH, W.W 1994 Turbulent structure in free-surface jet flows. *Submitted to Journal of Fluid Mech..*

[73] WILLERT, C. E. AND GHARIB, M. 1994 The interaction of modulated vortices pairs with free surfaces. *Free-Surface Turbulance - ASME* **181**, 25-36.

[74] WYGNANSKI, I. AND FIEDLER, H. 1969 Some Measurements in the Self-Preserving Jet. *Journal of Fluid Mech.* **38**, 577-612.

[75] YAMAMOTO, K. AND HOSOKAWA, I. 1988 A decaying isotropic turbulence pursued by the spectral methods. *Journal of Phys. Soc. Japan* **57**, 1532-1535.

[76] YODA, M., HESSELINK, L., AND MUNGAL, M. G. 1992 The evolution and nature of large-scale structures in the turbulent jet. *Phys. of Fluids A* **4** (4), 803-811 .

[77] YULE, A. J. 1978 Large-scale structure in the mixing layer of a round jet. *Journal of Fluid Mech.* **89**, 413-432.

[78] ZANG, Y., STREET, R. L., AND KOSEFF, J. R. 1993 A dynamic mixed subgrid-scale model and its application to turbulent recirculating flows. *Phys. of Fluids A* **5** (12), 3186-3196.